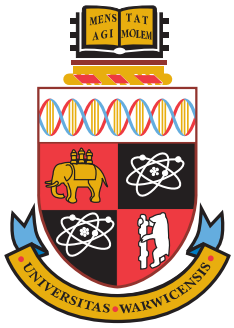

Direct Numerical Simulation of Turbulent Flow over a Backward-Facing Step

by

Michal Andrzej Kopera

Thesis

Submitted to the University of Warwick

for the degree of

Doctor of Philosophy

School of Engineering

March 2011

Contents

List of Figures

List of Tables

Acknowledgements

I would like to express my deep appreciation to my supervisor, Professor Robert Kerr, for allowing me to work on this project. His advice and support helped me to deepen the understanding of the fluid dynamics and computational methods.

I am grateful to Professor Dwight Barkley for fruitful discussions and helping me to get on track with simulations. I owe my gratitude to Dr. Hugh Blackburn for valuable advice on Semtex. I would like to thank Chris Cantwell for programming support and David Moxey for the implementation of the flowrate correction algorithm.

I acknowledge the financial support of EPSRC in frame of the EP/C007921/1 grant. I am thankful to the UK Turbulence Consortium, in particular Dr. Gary Coleman, for allowing me to access HECToR resources in frame of EPSRC grant EP/G069581/1. I am grateful to students and staff in the Centre for Scientific Computing for providing fun and stimulating research environment. I owe my gratitude to Ahmed Al Makky for helping me out on the last hurdle.

I would like do thank my parents and in-laws for warm thoughts and support in difficult times. I am grateful to Mateusz Jachimczyk for lending me his laptop.

Finally, and most importantly, I wish to immeasurably thank my wife Ewelina and son Antoś for their smile, support and motivation that helped me to get through many ups and downs. To them I dedicate this thesis.

Declaration

I herewith declare that this thesis contains my own research performed under the supervision of Professor Rober Kerr, without assistance of third parties, unless stated otherwise. No part of this thesis was previously published or submitted for a degree at any other university.

Abstract

A three-dimensional, turbulent flow in a channel with a sudden expansion was studied by direct numerical simulation of the incompressible Navier-Stokes equations. The objective of this study was to provide statistical data of backward-facing step flow for turbulence modelling. Additionally, analysis of the statistical and dynamical properties of the flow is performed.

The Reynolds number of the main simulation was $Re_h = 9000$, based on the step height and mean inlet velocity, with the expansion ratio $ER = 2.0$. The discretisation is performed using the spectral/hp element method with stiffly-stable velocity correction scheme for time integration. The inlet boundary condition is a fully turbulent velocity and pressure field regenerated from a plane downstream of the inlet. A constant flowrate was ensured by applying Stokes flow correction in the inlet regeneration area.

Time and spanwise averaged results revealed, apart from the primary recirculation bubble, secondary and tertiary corner eddies. Streamlines show an additional small eddy at the downstream tip of the secondary corner eddy, with the same circulation direction as the secondary vortex. The analysis of the 3D, time-only average shows the wavy spanwise structure of both primary and secondary recirculation bubble, that results in spanwise variations of the mean reattachment location. The visualisation of spanwise averaged pressure fluctuations and streamwise velocity showed that the interaction of vortices with the recirculation bubble is responsible for the flapping of the reattachment position. The characteristic frequency $St = 0.078$ was found.

The analysis of small-scale energy transfer was performed to reveal large backscatter regions in strong Reynolds stress areas in the mixing layer. High correlation of small-scale transfer with non-linear interaction of large-scale velocity and small-scale vorticity was found.

The data of the flow fields was archived. It contains the averages for velocities, pressure and Reynolds stress tensor, as well as 3D instantaneous pressure and velocity history.

List of Symbols

Abbreviations

BC	boundary condition
BFS	backward-facing step
DNS	direct numerical simulation
FEM	finite element method
FFT	fast Fourier transform
GLL	Gauss-Lobatto-Legendre points
LES	large-eddy simulation
PDE	partial differential equation
PIV	particle image velocimetry
PSD	power spectral density
SEM	spectral/hp element method

Roman symbols

$\mathbf{A}$	assembly matrix
$\mathbf{B}$	basis matrix
C_{pq}	correlation coefficient

C_f	coefficient of friction
C_P	coefficient of pressure
$\mathbf{D}$	derivation matrix
d_{ij}	element of the derivation matrix
$D(x)$	viscous dissipation
$E(x)$	kinetic energy
ER	channel expansion ratio
$\mathbf{F}_s$	sponge zone forcing
h	step height
$h_p(\xi)$	Lagrange polynomial through Gauss-Lobatto-Legendre points
$\mathbf{I}$	identity matrix
$\mathbf{I}_N^M$	filtering operator
J_e	explicit integration order
J_i	implicit integration order
$L(u)$	linear diffusion term of the Navier-Stokes equation
$\mathbf{L}$	filter matrix
L_i	streamwise dimension of the inlet channel
L_r	length of the inlet regeneration section
L_x	streamwise dimension of the outlet channel
L_y	vertical dimension of the outlet channel
L_z	spanwise dimension of the domain
$\mathbf{M}$	global mass matrix
$\mathbf{M}^e$	elemental mass matrix

$\mathbf{M}_b$	boundary-boundary interaction mass matrix
$\mathbf{M}_{bi}$	boundary-interior interaction mass matrix
$\mathbf{M}_i$	interior mass matrix
$\mathbf{n}$	normal vector
$N(u)$	non-linear convective term of the Navier-Stokes equation
N_{dof}	number of degrees of freedom
N_{el}	number of elements
N_P	number of nodal points
$\mathcal{N}_P$	nodal expansion basis
N_z	number of mesh points in spanwise direction
$O(x)$	enstrophy
p	static pressure
P	number of interpolating polynomials, unless stated otherwise
$\mathcal{P}_n(\overline{\Omega})$	space of polynomials of order n on a standard element
$\mathcal{P}_P^{(\alpha,\beta)}$	Jacobi polynomial of order P
Q	mass flow rate
$\overline{Q}$	prescribed flowrate
∇Q	irrotational part of the linear term L
R	residual of the approximation
Re	Reynolds number
Re_0	Reynolds number based on step height h and free stream velocity U_0 (in cases without the top wall)

Re_h	Reynolds number based on step height h and mean inlet velocity U_b
St	Strouhal number
S_{ij}	rate-of-strain tensor
t	time
T_{ave}	averaging time
T_{BI}	simulation burn-in time
T_{BT}	recirculation bubble turnover time
T_{FT}	flow-through time
$T(x)$	energy-transfer term
$\mathbf{u} = [u, v, w]^T$	velocity vector
U, V, W	averaged velocity components
u', v', w'	velocity fluctuations
U_0	free-stream velocity or maximum inlet velocity
U_b	mean inlet velocity
$u^\delta(x)$	approximation of $u(x)$
$\hat{u}_j$	expansion coefficient
$\hat{\mathbf{u}}, \hat{\hat{\mathbf{u}}}$	velocity sub-step vectors, unless stated otherwise
$\mathbf{U}_s$	prescribed velocity profile in the sponge zone
$\mathbf{u}_g$	Green function; a solution to Stokes problem
$v_j(x)$	test function
w_i	Gaussian quadrature weights
$\mathbf{x} = [x, y, z]^T$	position vector
X_r	reattachment length

Greek symbols

$\alpha(t)$	flowrate adjustment parameter
α_i	stiffly-stable scheme coefficients
α_s	sponge zone amplification parameter
β_i	explicit integration coefficients
δ_{pq}	Kronecker delta
$\Delta = \nabla \cdot \nabla$	Laplace operator, unless stated otherwise
Δx,Δy	element mesh size in spanwise and vertical dimension respectively
$\nabla = \left[\frac{\partial}{\partial x}, \frac{\partial}{\partial y}, \frac{\partial}{\partial z}\right]^T$	vector differential operator
γ_0	stiffly-stable scheme coefficient
γ_i	implicit integration coefficients
$\epsilon(\xi)$	approximation error
$\phi_j(x)$	local basis function
$\Phi(x)$	global basis function
ν	kinematic viscosity
ρ	density
ξ	coordinate in standard element
χ_e	coordinate mapping from a standard element to an arbitrary element
Ω	computational domain
Ω_e	element of the domain
$\partial\Omega_b$	bottom wall
$\partial\Omega_i$	inlet plane

$\partial\Omega_o$	outlet plane
$\partial\Omega_r$	regeneration plane
$\partial\Omega_t$	top wall
$\overline{\Omega}$	standard element
ω	vorticity
$\omega\mathbf{S}\omega$	enstrophy production

Superscripts and subscripts

a^*	non-dimensionalisation
a^+	in wall units
$\tilde{a}$	filtering operation
$\overline{a}$	average
$a^{\mathcal{S}}$	small-scale quantity
$a^{\mathcal{L}}$	large-scale quantity

Chapter 1

Introduction

1.1 Motivation

The flow over a backward-facing step (BFS) is a prototype for separating, recirculating and reattaching flow. Such phenomena occur both in nature and in numerous engineering applications, for example in flows around buildings, inside combustors, industrial ducts or in cooling of electronic devices. In all those cases the presence of separation, recirculation and reattachment drastically changes the transport of momentum and heat within the flow, which can have significant consequences. For an aeroplane separation results in a loss of the lift force and increased drag. Recirculation inside an expanding duct influences the recovery of the flow downstream from the expansion. In combustors, the presence of a shear layer between the main flow and the recirculation bubble can increase the mixing of fuel and oxidiser. In electronic systems the recirculation zone greatly changes the cooling properties of the flow. All of those examples share one common scenario, where an adverse pressure gradient (usually due to a sudden change of

geometry) causes the boundary layer to separate from the surface and form a mixing layer, which eventually reattaches to the surface again. The backward-facing step is a very good sample of such a scenario, as it demonstrates all those phenomena with a very simple geometry, which can be easily set-up experimentally, as well as modelled computationally.

On the other hand, the geometry of the BFS is the next most complicated paradigm for the direct numerical simulation (DNS), after the flows exhibiting periodicity in the streamwise direction - like the channel or pipe flow. To the Author's knowledge, there has been only one publication regarding three-dimensional DNS of turbulent flow over a BFS by Le *et al.* (1997). One of the motivations of this research is to demonstrate the applicability of the high-order spectral/hp element method (SEM) to relatively high Reynolds number flows in the BFS geometry and to increase the Reynolds number as high into the turbulent regime as possible, keeping in mind limited computational resources.

Another motivation is to provide the turbulence modelling community with a set of statistics and instantaneous flow field data, that can be used for better understanding and modelling of the separation, recirculation and reattachment of the turbulent flow. The analysis of collected results should provide useful insight into the structure and dynamics of the flow.

1.2 Survey of Previous Work

1.2.1 Experimental Investigations

BFS flow has received significant attention from experimental investigators. A good early review can be found in Abbot & Kline (1962). They examined the turbulent flow in a channel with a sudden expansion on either one or both walls. They have identified three regions of a separated turbulent flow: a three dimensional zone just after the step face, where one or more vortices with vertical axis of rotation were present (axis of rotation parallel to y axis using the notation of figure 2.1); two dimensional zone downstream of the first zone demonstrating a classical stall pattern where the flow near the wall moves upstream and the flow adjacent to the through-flow moves downstream with little spanwise fluctuation of velocity; and finally the third zone - time dependent reattachment region, whose size is changing periodically in time. The dimensionality of the flow in the main flow region was judged based on the mean velocity profiles in the vertical and spanwise directions, however the investigations in the recirculation region were based solely on observations of a dye injected into the flow.

Bradshaw & Wong (1972) provided an extensive overview of experiments on recirculating flows in different configurations performed up to 1970, like a square obstacle, a fence or a BFS, as well as some of their own measurements of the BFS case, with special attention on regeneration of the shear layer. The authors provide mean velocity and turbulence intensity profiles along the vertical direction as well as the skin friction coefficient along the streamwise direction after the reattachment. The study shows that the behaviour of the relaxing boundary

layer is strongly dependent on the fraction of mass flow that is deflected upstream at the reattachment and supplies the recirculation. They also note the bifurcation that occurs in a symmetrically expanded channel (with the symmetry plane in the middle of the channel, perpendicular to vertical direction) - the reattachment length differs significantly on both walls, as was noted by Abbot & Kline (1962), but the configuration changes spontaneously. The side that initially had the longer recirculation zone now is at the deficit as compared to the opposite side of the expanded channel. This finding demonstrates the importance of the time dependence of the reattachment position. The conclusions of the paper are that the reattaching shear layer does not resemble any other previously known behaviour like plane mixing layer or any other thin shear layer. Also, the investigation of the regeneration of the boundary layer shows that it is a very slow process and the law of the wall cannot be applied within the distance of at least 52 step heights from the step edge.

Etheridge & Kemp (1978) report measurements of velocity, turbulence intensities and Reynolds shear stress around the reattachment of the boundary layer. The authors present evidence that the reattaching shear layer splits and deflects about 1/6th of the mass flow upstream to the recirculation zone. They report large values of Reynolds stresses in the reattachment region, which decreases rapidly downstream. The authors did not notice, however, a time periodicity in the reattachment length, which is in contrary to the two previous papers. It should be noted that, in general, the large differences in the results of those early experiments can be attributed to different techniques used (hot film, laser anemometer, Pitot tube).

In order to investigate the asymmetry between reattachment positions at opposite walls in the BFS flow with symmetric (double) expansion and look at periodic time oscillations of the recirculation length Durst *et al.* (1974) and Cherdron *et al.* (1978) used laser-Doppler anemometry to examine the laminar flow through a channel with double expansion. The authors demonstrate that symmetric mean velocity profiles can exist in a two-dimensional BFS geometry for a limited range of Reynolds numbers. For transitional and turbulent flow regime, small disturbances, which are generated near the step edge by the unsteady recirculating flow, are amplified in the mixing layer. Cherdron *et al.* (1978) report that the peak of the spectrum of oscillations and magnitude of the predominant frequency depends on the Reynolds number. They also support the locking-on condition postulated by Martin (1974), which states that "only the uneven number of oscillation cycles will feed back the correct in-phase disturbance to the lip of the step from which separation occurs" what will allow for the self sustainability of the disturbances. The unsteady mixing layer causes the recirculating flow to be unsteady as well, which feeds-back the disturbance to the near-edge region of the mixing layer and generates disturbances - that closes the self-sustainable cycle. The authors report that the shorter reattachment length is always approximately equal to one cycle length corresponding to the predominant frequency, while the longer reattachment is usually of the order of three cycle lengths. The conclusion of the paper is that the amplification of the disturbances in the shear layer reaches a maximum for the Strouhal number equal 0.11 (based on maximum velocity).

The work of Chandrsuda & Bradshaw (1981) is a direct continuation of the experiments of Bradshaw & Wong (1972). Using a hot-wire probe the authors

measured second and third-order mean products of velocity fluctuations and provided turbulent energy and shear stress budgets. They note that the mixing layer turbulent properties change rapidly in the reattachment zone, and suggest that in order to represent this any non-direct computational method that deals with reattachment should have sophisticated models for triple products of velocity fluctuations.

Kim *et al.* (1980) performed an extensive investigation of pressure distribution, turbulence intensities and shear stress in both recirculation and reattachment regions. Although the measurement technique incorporated high uncertainties, especially in the recirculation zone, the authors confirmed the findings of other researchers, namely an increased turbulence intensity and shear stress near the reattachment, followed by a rapid decrease downstream. Also, the slow regeneration of the boundary layer and streamwise pressure distribution is documented up to 16 step heights after the step edge.

Durst & Tropea (1981) examined the influence of the expansion ratio (ER) - that is the ratio of the height of the outlet channel to the inlet channel - on the reattachment position X_r. Their study showed that X_r grows with ER, but the relation is nonlinear with the steepest growth in the range $1 < ER < 1.3$. This study also found a strong dependence of the reattachment position on Reynolds number up to $Re = 6000$, based on the hydraulic diameter of the inlet channel and mean inlet velocity. Further investigations by Armaly *et al.* (1983) confirmed and expanded the range of Reynolds numbers to an early turbulent regime. Using laser-Doppler anemometer they measured the reattachment length as a function of Reynolds number in a range $70 < Re < 8000$. They reported that

the reattachment length grows with Reynolds number in the laminar regime, then drops in the transitional regime ($1200 < Re < 6600$) and remains fairly constant in the turbulent regime, with a value of $X_r \approx 8$ for the expansion ratio $ER = 1.94$. Another important finding was the presence of the secondary recirculation bubble at the wall opposite to the step. The size of that bubble initially increased, then decreased with Re, to vanish when the flow became fully turbulent.

Adams & Johnston (1988) investigated the effect of the upstream boundary layer thickness and shape on the flow structure and reattachment position in a wide range of Reynolds numbers ($800 < Re < 40000$). The authors reported measurements of the wall static pressure, reattachment length and wall shear stress. The reattachment length increased by 30% when the upstream boundary layer underwent transition from laminar to turbulent. Also the friction coefficient was sensitive to boundary layer thickness change.

Jovic & Driver (1995) employed the Laser-Oil Flow Interferometry technique to measure the skin-friction for different Reynolds number flows. The results show that the skin-friction magnitude decreases as the Reynolds number increases both in the recirculation zone and downstream of reattachment. The minimum of skin-friction coefficient scales like $C_{f,min} \sim Re^{-1/2}$ which suggests that the recirculating flow is dominated by viscosity and resembles laminar flow for the examined Reynolds numbers range $5000 < Re < 37200$. This finding is in agreement with previous experiments by Castro & Haque (1987).

Kasagi & Matsunaga (1995) performed 3D Particle Tracking Velocimetry measurements of all three components of velocity. They performed a detailed analysis of turbulence statistics for a region spanning from -2 step heights upstream to

12 step heights downstream of the step. The main motivation was to validate recent DNS simulation by Le *et al.* (1993). The agreement of mean and fluctuating velocities, the Reynolds shear stress, and the turbulent kinetic energy budget proved to be very good, despite the difference in inflow conditions.

Spazzini *et al.* (2001) focused on low-frequency motions in turbulent flow over a BFS. They measured the time history of skin friction in the recirculation and reattachment regions and performed flow visualisation in order to investigate the flapping of the separated flow. The authors reported a difference in the behaviour of the flow upstream and downstream of the secondary recirculation bubble separation point. The secondary recirculation bubble has a low-frequency cycle with frequency corresponding to the flapping of the primary separated region. They point out that this relationship may suggest that those two cases are different aspects of the same motion.

Yoshioka *et al.* (2001) applied a time-periodic perturbation at the step edge in order to examine the possibilities of controlling the separation. It turns out that by applying perturbations at optimum frequency, $St = 0.19$, the reattachment length was reduced by 30%. At the same time the Reynolds shear stress increased in the shear layer. The authors argue that the increased Reynolds stress enhances the momentum transfer in the shear layer, which leads to a shorter reattachment length.

Hall *et al.* (2003) investigated the secondary corner vortex that appears very close to the step edge. The authors suggest a new structure that occurs in the vicinity of the secondary bubble. The PIV results show that a portion of the reversed flow in the primary bubble divides and flows perpendicularly to the cross-

sectional plane in which measurements were taken. The authors also concluded that the secondary vortex is highly three-dimensional and varies strongly in time. No evidence of a tertiary corner vortex was found.

1.2.2 First Numerical Experiments

Early investigations showed that computational methods up to 1980 were unable to deal with the recirculation and reattachment problem. The main issue were very limited computational resources and lack of turbulence models that could reproduce reattaching flow reliably. Thus the first attempts to solve the flow over a BFS were confined to two-dimensional cases. Armaly *et al.* (1983), apart from an extensive experimental study, performed the computations of a laminar flow over a BFS using the finite volume discretisation of the Navier-Stokes equations. Results compared to experimental data showed that the reattachment length was under-predicted for Reynolds numbers greater than 400, which was attributed to the three-dimensionality of the flow observed in experiments. The simulation managed to predict the secondary recirculation region at the wall opposite to the step.

Friedrich & Arnal (1990) provided the first high Re simulation ($Re_0 = 1.65 \times 10^5$, based on the step height and centreline inlet velocity) of BFS using LES on a uniform mesh. They reported $X_r = 7.0$ for high Re as opposed to $X_r \approx 8.5$ for Durst and Tropea experiments. The authors argued that this difference might be due to less than fully developed flow in the experiment inlet. Friedrich & Arnal (1990) reported that the mixing layer is oscillating in the horizontal direction - this phenomenon was called *flapping* of the shear layer. The time-averaged

reattachment line did not reveal any oscillations in the spanwise direction. They also reported instantaneous contours of $u = 0$, which corresponds to the instantaneous reattachment location, suggesting after Bradshaw & Wong (1972) that its movement is a consequence of amalgamation of turbulent structures.

Kaikstis *et al.* (1991) applied a high order mixed spectral/spectral element method to a transitional flow over a BFS. They focused on early transition to turbulence and three dimensionality in a nominally two-dimensional geometry. Up to 1991, all direct simulations of BFS were performed for two-dimensional geometry and consistently under-predicted X_r above $Re = 600$. The authors concluded, after Armaly *et al.* (1983), that it is because of the three-dimensionality of the flow. They identified characteristic frequencies of the flow depending on Re, however the spectra for higher Re are wide-band.

Silveira Neto *et al.* (1993) performed 2D and 3D computations of BFS with prescribed inlet velocity profile with superimposed noise using both direct and large-eddy simulations. They focused upon the coherent structures occurring in BFS flow. Their investigation revealed that there is a pairing of main Kelvin-Helmholtz vortices in the mixing layer, with secondary hairpin vortices in between. The authors reported that the Strouhal number for largest vortices in their 3D simulation was 0.08 (compared to the Eaton and Johnston 1980 value of 0.07).

1.2.3 Direct Numerical Simulations

Direct numerical simulations of the flow over the backward-facing step have focused mainly on the laminar and transitional regime. The only exception was the

study by Le *et al.* (1997), where the authors presented results of computation of a turbulent flow in an open channel with sudden expansion domain for $Re = 5100$, based on free stream velocity and step height, with expansion ratio $ER = 1.2$. Statistics were in excellent agreement with concurrent experimental study by Jovic & Driver (1994). The study of the dynamical behaviour of the reattachment length showed the characteristic frequency of oscillations to be $St = 0.06$. The authors reported a mean reattachment length of $X_r = 6.28$ with the instantaneous reattachment location varying in the spanwise direction. A very high negative skin friction coefficient was discovered in the recirculation area, which was attributed to a relatively low Reynolds number. Also, the velocity profiles at long distances downstream were not fully developed, which confirmed slow regeneration of the velocity profile after reattachment.

The work of Le *et al.* (1997) became a reference for all turbulence models and set a standard in separated turbulent flow simulations. The present study aims to extend the DNS database of turbulent backward-facing flows to higher Reynolds numbers.

1.3 Outline of the Thesis

This thesis draws on the results reviewed in the previous section and is organised as follows.

Chapter 2 presents the numerical methods used to perform the simulations. The domain configuration and mesh generation is discussed and the boundary conditions are specified. The main ideas behind the spectral element method are presented for one-dimensional problem and subsequently extended to two-

dimensional formulation used in this work. The time advancement scheme, along with a stiffly-stable formulation, is discussed and the method for flowrate control is presented. The chapter is concluded with the introduction of filtering methods used for the small-scale energy transfer analysis.

Chapter 3 provides the review of papers, where the validation of the code was documented, and summarises the preliminary simulations performed in order to specify parameters of the main simulation. Also, the examination of inlet and outlet boundary conditions is presented using the results of the turbulent channel flow simulation.

Chapter 4 presents the results of the main simulation with $Re_h = 9000$. Firstly, the verification of results is performed by comparing the reattachment length and coefficient of friction with previous experimental and computational results. Subsequently the averaged fields of pressure, velocity and Reynolds stresses are analysed and conclusions regarding the structure of the flow are made. This investigation is complemented by the examination of instantaneous results and time-sequences of wall shear stresses, which provides interesting insight into the behaviour of the reattachment position. The chapter is concluded with the analysis of the small-scale energy transfer.

Chapter 5 provides a summary and conclusion of the thesis, along with proposed future extension of the work done.

Chapter 2

Numerical Methods

This chapter defines the problem addressed in the thesis and discusses the methods applied to solve it and analyse the results. Firstly, the governing equations, domain and boundary conditions are specified. A special kind of inlet boundary condition, called the *copy boundary condition*, is discussed in detail. The design of the element mesh is presented, followed by the introduction of the spectral/hp element method. The method, initially formulated for a one-dimensional case in order to clearly demonstrate the main ideas, is subsequently extended to two-dimensions. The numerical code Semtex (Blackburn & Sherwin, 2004), which is used throughout this project, employs hybrid spectral - spectral element method, where periodic dimension is discretized using Fourier pseudo-spectral aproach, and resulting set of 2D problems is discretized using spectral/hp element method. Therefore the two-dimensional formulation of the spectral element method is considered.

The time advancement scheme is discussed, and the stiffly-stable formulation, that improves the stability of computations, is introduced. Also, the method of

flowrate control is presented, as maintaining constant mass flow was one of the main issues in the simulations. Finally, the filtering methods applicable to the spectral element discretisation are introduced.

2.1 Governing Equations

The flow over a backward-facing step is governed by the Navier-Stokes equation for incompressible flow:

$$\frac{\partial \mathbf{u}}{\partial t} + (\mathbf{u} \cdot \nabla)\mathbf{u} = -\frac{1}{\rho}\nabla p + \nu \Delta \mathbf{u} \tag{2.1}$$

with the continuity equation given by:

$$\nabla \cdot \mathbf{u} = 0 \tag{2.2}$$

where $\mathbf{u} = [u, v, w]^T$ is the velocity vector, p is static pressure, ν is kinematic viscosity and ρ is density. Without the loss of generality one can assume $\rho = 1$. All variables are non-dimensionalized by the mean inlet velocity U_b and step height h:

$$t^* = \frac{tU_b}{h}, \qquad x^* = \frac{x}{h}, \qquad \mathbf{u}^* = \frac{\mathbf{u}}{U_b}, \qquad p^* = \frac{p}{\rho U_b^2} \tag{2.3}$$

The non-dimensional equations take the form:

$$\nabla \cdot \mathbf{u}^* = 0 \tag{2.4}$$

$$\frac{\partial \mathbf{u}^*}{\partial t^*} + (\mathbf{u}^* \cdot \nabla)\mathbf{u}^* = -\nabla p^* + \frac{1}{Re_h}\Delta \mathbf{u}^* \tag{2.5}$$

where $Re_h = \dfrac{U_b h}{\nu}$ is the Reynolds number. For the sake of simplicity, the superscript * will be dropped for the remainder of this dissertation.

2.2 Geometry and Mesh

2.2.1 Domain definition and boundary conditions

The simulated case consists of a flow inside a channel with a one-sided sudden expansion. Figure 2.1 presents the overview of the geometry along with a schematic of the inlet and outlet boundary conditions. The coordinate frame is defined by (x, y, z) axis, where x indicates the streamwise, y the vertical and z the spanwise directions. The origin of the coordinate frame is located at the bottom of the step at the rear end of the span of the domain.

The outlet channel has dimensions $L_x = 29h$ and $L_y = 2h$. The inlet channel is $L_i = 12h$ long and its height is equal $L_y - h = h$ which gives the expansion ratio $ER = \dfrac{L_y}{L_y - h} = 2$. The computational domain Ω is defined as:

$$\Omega : (x, y, z) \in [-12h, 0] \times [h, 2h] \times [0, 2\pi h] \quad \cup \quad [0, 29h] \times [0, 2h] \times [0, 2\pi h]. \tag{2.6}$$

Walls confining the channel are modelled as no-slip walls with Dirichlet type boundary condition $\mathbf{u} = 0$. The wall at $y = 2h$ (further referred to as the top wall) is defined as:

$$\partial\Omega_t : (x, y, z) \in [-12h, 29h] \times \{2h\} \times [0, L_z]. \tag{2.7}$$

The step wall (also referred to as the bottom wall) is defined as:

$$\begin{aligned} \partial\Omega_b : (x, y, z) \quad &\in \quad [-12h, 0] \times \{h\} \times [0, L_z] \\ &\cup \quad \{0\} \times (0, h) \times [0, L_z] \\ &\cup \quad [0, 29h] \times \{0\} \times [0, L_z]. \end{aligned} \tag{2.8}$$

The channel is periodic in the spanwise direction with a periodic length of $L_z = 2\pi h$. The periodic length was chosen based on results by Le (1995) ($L_z = 4.0h$), Schafer *et al.* (2009) ($L_z = \pi h$) and Kaikstis *et al.* (1991) ($L_z = 2\pi h$). Le (1995) reports that a periodic length of $L_z = 4.0h$ was adequate to tail off the two-point correlations for u, v and w near the wall, however the correlations at separation $L_z/2$ computed at a location away from the wall in the free shear layer remained at approximately 10% level. One reason for that was the presence of spanwise rollers in the free shear layer. In the present study the periodic dimension is over 50% longer in order to make sure that all spanwise structures are well represented.

A special kind of boundary condition is prescribed at the inlet to the domain. It is a variation of the method for generation of turbulent inflows proposed by Lund *et al.* (1998). The method assumed extracting the plane of velocity data from an auxiliary simulation of wall bounded flow. In the present study the velocity and pressure is regenerated from a plane downstream of the inlet and prescribed as Dirichlet boundary condition at the inlet plane. This is schematically presented in figure 2.1 (a). The length of the regeneration section is $L_r = 8h$. This type of boundary condition will be referred to as the *copy* boundary condition. The validation of this technique is presented in Section 4.2.1. Details of the

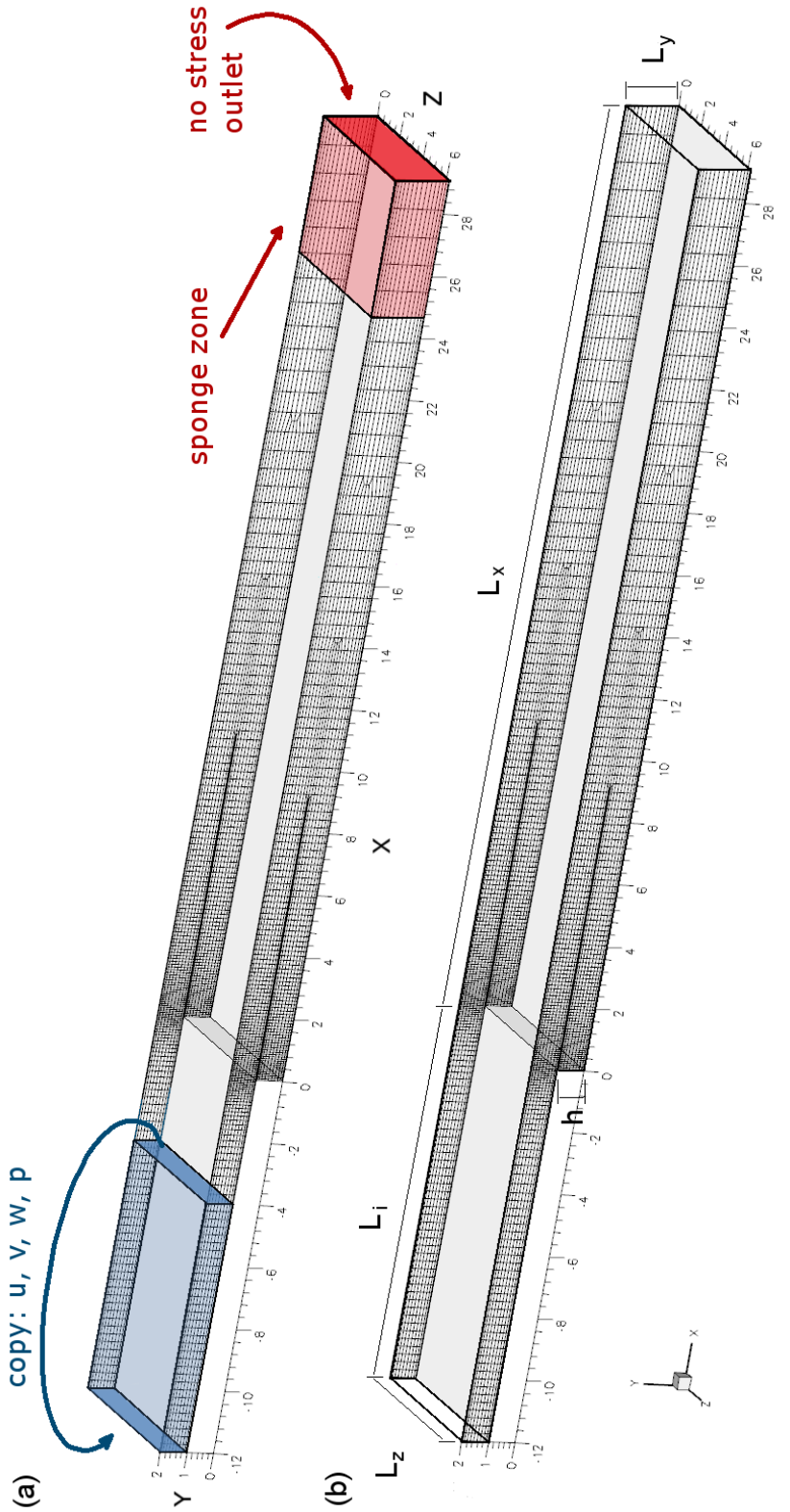

Figure 2.1: Geometry overview - (a) schematics of inlet and outlet boundary conditions, (b) dimensions of the domain

implementation to Semtex can be found in Cantwell (2009).

$$\begin{aligned} \mathbf{u}\mid_{\partial\Omega_i} = \mathbf{u}\mid_{\partial\Omega_r} \quad \partial\Omega_i &: (x,y,z) \in \{-12h\} \times [h,2h] \times [0,2\pi h] \\ \partial\Omega_r &: (x,y,z) \in \{-12h + L_r\} \times [h,2h] \times [0,2\pi h]. \end{aligned} \tag{2.9}$$

The outlet boundary condition prescribed at $\partial\Omega_o$ is the Neumann condition:

$$\nabla\mathbf{u}\cdot\mathbf{n}\mid_{\partial\Omega_o} = 0 \quad \partial\Omega_o : (x,y,z) \in \{29h\} \times [0,2h] \times [0,2\pi h], \tag{2.10}$$

where $\mathbf{n}$ is a unit vector perpendicular to $\partial\Omega_o$.

In case the Neumann condition would not advect the flow structures out of the domain properly, an additional sponge zone was implemented in the area $2h$ upstream of the outflow in order to dampen excessive oscillations. The sponge zone was implemented by adding a forcing term to equation (2.5):

$$\mathbf{F_s} = -\alpha_s(\mathbf{u} - \mathbf{U_s}), \tag{2.11}$$

where $\mathbf{U_s}$ is a prescribed velocity profile, i.e. the mean turbulent channel flow profile obtained and rescaled from the inlet channel, and α_s is a parameter regulating the forcing amplitude. The aim of the sponge zone was to force the turbulent flow towards the prescribed profile. In the course of preliminary simulations it turned out that the length of the outflow channel was sufficient for the flow to regenerate enough to be advected by the Neumann condition (2.10) without additional forcing, therefore in the main simulation $\alpha_s = 0$.

The implementation of the sponge zone forcing to Semtex was provided by

Dr. Jörg Stiller from TU Dresden.

2.2.2 Mesh

The problem defined in sections 2.1 and 2.2.1 is discretised in the spanwise direction using Fourier pseudo-spectral method. A set of 2D problems resulting from Fourier transform can then be discretised in using the two-dimensional spectral/hp element method (SEM). The 2D SEM consists of the expansion of the solution in the polynomial base on quadrilateral elements (triangular elements, or elements with curved edges are also possible) which pave the entire computational domain. Details of the methods are discussed in Sections 2.3 and 2.4. In the present case the element mesh is constructed for the $x - y$ plane and a uniform mesh is applied in the spanwise direction which enables the application of Fast Fourier Transform (FFT). The outline of the element mesh is shown in figure 2.1 and the close-up of the area near the step is presented in figure 2.2.

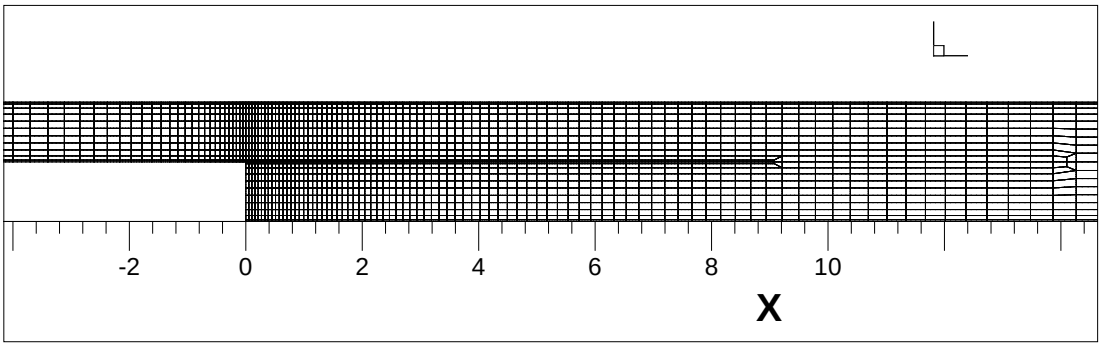

Figure 2.2: Spectral element mesh - close-up on the area near to the step.

The element mesh is block-structured with non-structured elements near $(x, y) = (9h, h)$, $(x, y) = (14h, h)$ and $(x, y) = (19h, h)$. The non-structured elements were introduced in order to coarsen the vertical resolution in the middle part of the

channel and maintain at the same time the conformity of the grid, which is a requirement for the software used for the simulation.

The mesh in the inlet channel consists of 11 elements in the vertical direction. Each element consists of 11 nodal points in each direction, which gives a total of 121 nodal points in the vertical direction. Only 111 of them are unique, because nodal points at elemental boundaries coincide and the C^0 continuity is enforced across the boundary. The distribution of element vertexes, which define the elements, mimic the Chebyshev distribution, following a good practise guidelines for SEM DNS of channels contained in Karniadakis & Sherwin (2005, p.475). The size of the element closest to the wall is approximately 16 wall units, based on the friction velocity measured at $x = -8h$ in the inlet channel. With 11 nodal points inside an element, the first point away from the wall is located at $\Delta y^+ = 0.528$.

The inflow vertical distribution of element vertexes continues in the upper part of the outflow channel. The lower part of the outflow channel is paved similarly, which ensures high resolution in the mixing layer and good resolution of the boundary layers at the walls. Downstream of $x = 9h$ the vertical distribution is gradually coarsened in the middle part to avoid an unnecessary concentration of elements downstream of the mixing layer.

In the streamwise direction the mesh is uniform in the periodic (regeneration) part of the inlet channel, with the element size $\Delta x = 0.25h$ which corresponds to $\Delta x^+ \approx 136$ for an element, and Δx^+ between 4.5 and 20.1 for nodal points within each element. It is gradually refined from $x = -4h$ to $x = 0$, and it slowly coarsens downstream of the step. The smallest streamwise element size near the step has $\Delta x^+ \approx 27$, which corresponds to the smallest distance between the nodes

of $\Delta x^+ \approx 1.78$. A single $x - y$ slice of the domain consists of 2845 2D elements and 344245 nodal points.

The number of collocation points in the spanwise direction $N_z = 128$, which corresponds to 64 Fourier modes, is doubled as compared to Le (1995), which results in higher resolution as the spanwise domain size is only increased by over 50%. This is to avoid problems with resolving small-scale structures at $y^+ < 10$, as reported by Le (1995). The spanwise resolution analyses are presented in Section 4.2.3.

2.3 Fourier Spectral Method

Since the spanwise direction in the BFS domain is periodic, it is possible to apply a spectral method in that direction. In Fourier spectral methods the global solution $u(z)$ is approximated by a finite number of Fourier expansion modes

$$u(z) = \sum_{k=0}^{N-1} \hat{u}_k e^{ikz}, \tag{2.12}$$

where $\hat{u}_k$ are the coefficients of Fourier expansion and $i = \sqrt{-1}$. The coefficients are found using the Fast Fourier Transform (FFT)

$$\hat{u}_k = \frac{1}{N_z} \sum_{j=0}^{N_z-1} u(z_j) e^{-2\pi ijk/N_z}, \qquad k = 0, \ldots, N_z - 1. \tag{2.13}$$

However, only $N_z/2$ coefficients will be unique, the rest being complex conjugates. Therefore after the spanwise Fourier transform the original three dimensional

problem (2.5) turns into a set of two dimensional problems:

$$\hat{\nabla}_k \cdot \hat{\mathbf{u}}_k = 0, \tag{2.14}$$

$$\frac{\partial \hat{\mathbf{u}}_k}{\partial t} + \widehat{\mathbb{N}(\mathbf{u})}_k = -\hat{\nabla}_k \hat{p}_k + \frac{1}{Re_h}\hat{\Delta}_k \hat{\mathbf{u}}_k, \qquad k = 0, \ldots, N_z/2 \tag{2.15}$$

where $\hat{\mathbf{u}}_k$ is a vector of Fourier velocity coefficient $[\hat{u}_k, \hat{v}_k, \hat{w}_k]^T$, $\hat{\nabla}_k = [\frac{\partial}{\partial x}, \frac{\partial}{\partial y}, ik]^T$ and $\hat{\Delta}_k = \hat{\nabla}_k \cdot \hat{\nabla}_k$.

The term $\widehat{\mathbb{N}(\mathbf{u})}_k$ is the representation of the non-linear term in the Fourier space. We could evaluate it in Fourier space by a convolution of Fourier coefficients. For example, the term $u\frac{\partial u}{\partial z}$ would give

$$\begin{aligned} \widehat{u\frac{\partial u}{\partial z}} &= \sum_{l=0}^{N_z/2-1} \hat{u}_l e^{ikz} \frac{\partial}{\partial z} \sum_{k=0}^{N_z/2-1} \hat{u}_k e^{ikz} \\ &= \sum_{l=0}^{N_z/2-1} \hat{u}_l e^{ikz} \sum_{k=0}^{N_z/2-1} ik\hat{u}_k e^{ikz}, \end{aligned} \tag{2.16}$$

which requires the evaluation of $N_z^2/4$ products $\hat{u}_l\hat{u}_k$. Instead of this costly operation, the non-linear term is evaluated in real space and only then transformed to Fourier space. This procedure is called a pseudo-spectral method. Three-dimensional problems in Semtex are solved using this approach. The 3D problem is transformed to a set of $N_z/2$ 2D complex problems. Each 2D problem is discretised using spectral/hp element method and can be allocated to a different processing core. The communication between cores happens when the non-linear term needs to be evaluated in real space, and therefore the data needs to be transformed to real space and back to Fourier space.

2.4 Spectral Element Method in 1D

This section discusses the spectral/hp element method used to solve the set of 2D problems stated in Section 2.3. For the purpose of demonstration the one-dimensional case will be initially considered. Section 2.5 will discuss the extension of the ideas presented here to two-dimensions.

The SEM combines the geometrical flexibility of the finite element method (FEM) with high-order accuracy and exponential convergence of the global spectral method. Similarly like in FEM, the domain is divided into a set of elements. The contribution of spectral methods is that the solution is expanded into a polynomial base within each element, which results in exponential convergence. This creates an opportunity for independent refinement of the element mesh locally (h-refinement) and increasing of the interpolating polynomial order globally (p-refinement).

In order to be able to implement the method efficiently, one needs to specify the relation between an arbitrary element and a standard element, where the expansion basis is defined. Eventually, the methods for derivation and integration within a standard element will be presented.

2.4.1 Galerkin method

The spectral element method utilises the weak Galerkin formulation of a partial differential equation (PDE). The idea behind the Galerkin method is to expand the solution in a function space and construct a functional (the weak form of the equation), by zeroing which will minimize the errors of the approximation of the solution. This section provides the definition of this errors, called the residual,

along with a framework of the Galerkin method.

The approximation to a continuous function $u(x)$ in a domain $\overline{\Omega}$ can be expressed in terms of a finite number of expansion basis functions $\phi_j(x)$

$$u(x) \approx u^{\delta}(x) = \sum_{j=0}^{N} \hat{u}_j \phi_j(x), \qquad x \in \overline{\Omega}. \tag{2.17}$$

Let $\mathbb{F}$ be a differential operator in $\overline{\Omega}$.

$$\mathbb{F}(u(x)) = 0. \tag{2.18}$$

The *residual* of the approximation u^{δ} is defined as

$$R(x) = \mathbb{F}(u^{\delta}(x)). \tag{2.19}$$

$R(x) \to 0$ as $u^{\delta}(x) \to u(x)$. Therefore by minimising R one obtains the best possible approximation for $u(x)$. This constraint can be expressed as

$$(v_j(x), R) = 0, \ j = 0, \cdots, N, \tag{2.20}$$

where $v_j(x)$ are test functions and $(\cdot, \cdot)$ denotes Legendre inner product over $\overline{\Omega}$

$$(f, g) = \int_{\overline{\Omega}} f(x) g(x) dx. \tag{2.21}$$

The Galerkin formulation of problem (2.18) is constructed by selecting expansion

functions as test functions: $v_j(x) = \phi_j(x)$, which yields

$$(\phi_j(x), \mathbb{F}(u^\delta(x))) = \int_{\overline{\Omega}} \phi_j(x) \mathbb{F}\left(\sum_{j=0}^{N} \hat{u}_j \phi_j(x)\right) dx = 0. \tag{2.22}$$

Therefore solving equation (2.18) is equivalent to minimising the functional (2.22).

2.4.2 Elemental decomposition and the standard element

As mentioned in Section 2.2.2, the spectral element method decomposes the domain Ω into a set of non-overlapping elements Ω_e:

$$\Omega = \bigcup_e \Omega_e, \tag{2.23}$$

where for $\widetilde{\Omega}_e = \Omega_e / \partial\Omega_e$

$$\widetilde{\Omega}_e \cap \widetilde{\Omega}_f = \emptyset \qquad \forall e \neq f. \tag{2.24}$$

This partitioning is defined by a set of points $x_e \in \Omega$ such that:

$$\Omega_e = \{x | x_e \leq x \leq x_{e+1}\}. \tag{2.25}$$

The set $\{x_e\}$ forms an element mesh that can be locally adjusted. This sort of mesh extension is called *h-type extension* and is characteristic for finite element methods.

Each element Ω_e can be of arbitrary length (or in higher dimensions of arbitrary shape). Therefore in order to simplify operations performed on such

elements, the *standard element* is introduced:

$$\overline{\Omega}_e(\xi) = \{\xi | -1 \leq \xi \leq 1\}. \tag{2.26}$$

The data from an arbitrary element is mapped onto the standard element, where all the operations (differentiation and integration) are performed, and mapped back to an arbitrary element. Such an approach leads to a more efficient numerical scheme than if the operations were performed on arbitrary elements. In order to be able to make such a projection, a coordinate change is needed. For an arbitrary element $\Omega_e \in [x_e, x_{e+1}]$ the projection is a linear mapping $\chi_e : \overline{\Omega}_e \to \Omega_e$

$$x = \chi_e(\xi) = \frac{1-\xi}{2} x_e + \frac{1-\xi}{2} x_{e+1}, \tag{2.27}$$

and the inverse mapping $\chi_e^{-1} : \Omega_e \to \overline{\Omega}_e$ is

$$\xi = \chi_e^{-1}(x) = 2\frac{x - x_e}{x_{e+1} - x_e} - 1. \tag{2.28}$$

2.4.3 Local and global expansion basis

Let $\mathcal{P}_n(\overline{\Omega})$ be a space of polynomials of order n or less on the standard element $\overline{\Omega}$. Any continuous function $u(\xi)$ is approximated on a standard element in terms of a set of P polynomials $\phi_p \in \mathcal{P}_{P-1}$ where $p = 0, 1, ..., P-1$.

$$u(\xi) \approx u^{\delta}(\xi) = \sum_{p=0}^{P-1} \hat{u}_p \phi_p(\xi) \tag{2.29}$$

where $\hat{u}_p$ are expansion coefficients corresponding to polynomials ϕ_p. Such polynomials are called the *local basis functions*.

In order to obtain basis functions for an arbitrary element, one can use the mapping χ_e:

$$\phi_p^e(x) = \phi(\chi_e^{-1}(x)). \tag{2.30}$$

Local basis functions for arbitrary elements are used to construct the *global basis functions*:

$$\Phi_{k=k(p,e)}(x) = \begin{cases} \phi_p^e(x) & \text{if } x \in \Omega_e \\ 0 & \text{otherwise} \end{cases}. \tag{2.31}$$

Function $u(x)$ defined on the global domain Ω can be approximated using the global expansion basis:

$$u(x) \approx u^\delta(x) = \sum_{k=0}^{N_{dof}-1} \hat{u}_k \Phi_k(x) = \sum_{e=1}^{N_{el}} \sum_{p=0}^{P-1} \hat{u}_p^e \phi_p(\chi_e^{-1}(x)). \tag{2.32}$$

Because $N_{dof} \neq N_{el} \cdot P$, additional constraints need to be applied for local expansion coefficients $\hat{u}_p^e$. Those constraints represent the fact that global modes are continuous throughout the domain and will depend on the choice of the expansion basis.

It follows from equation (2.31) and (2.32) that if $\hat{\mathbf{u}}_g = [\hat{u}_0, \cdots, \hat{u}_{N_{dof}-1}]^T$ is a

vector of all global coefficients, and

$$\hat{\mathbf{u}}_l = \begin{bmatrix} \hat{\mathbf{u}}^1 \\ \hat{\mathbf{u}}^2 \\ \vdots \\ \hat{\mathbf{u}}^{N_{el}} \end{bmatrix}$$

is a vector of all local coefficients, where $\hat{\mathbf{u}}^e = [\hat{u}^e_0, \hat{u}^e_1, \cdots, \hat{u}^e_{P-1}]^T$ is a vector of local coefficients for element e, then one can express the relation of local and global coefficients in matrix form:

$$\hat{\mathbf{u}}_l = \mathbf{A}\hat{\mathbf{u}}_g. \tag{2.33}$$

The matrix $\mathbf{A}$ is called the *assembly matrix* and is usually very sparse. It allows for a quick transformation of data in the global basis into the local bases. One can also consider a reverse operation of reassembling global expansion from local coefficients. It is called the *global assembly* or *global stiffness summation* and is done using a transpose of the assembly matrix $\mathbf{A}^T$ (see Karniadakis & Sherwin, 2005, p. 41).

The choice of expansion basis is crucial for an efficient numerical method. Two categories of polynomial basis are considered: *hierarchical* (modal) and *non-hierarchical* (nodal). The hierarchical expansion basis is a basis where a set of expansion polynomials of order $P-1$ is contained within an expansion set of order P. An example of such a basis is $\phi_p = x^p$, where $\{1, x, x^2\} \subset \{1, x, x^2, x^3\}$.

The nodal expansion basis is formed on a series of $N_P = P + 1$ nodal points.

This set of points constitutes a local element mesh. The points are chosen so that for any given point ξ_q in standard element $\overline{\Omega}$ only one polynomial $\phi_p(\xi)$ in the expansion basis has the value equal 1 while all others vanish:

$$\mathcal{N}_P = \{\phi_p(\xi) \in \mathcal{P}_P(\overline{\Omega}) | \phi_p(\xi_q) = \delta_{pq},\ p, q = 0, 1, .., N_P - 1\}. \tag{2.34}$$

A typical choice of nodal expansion polynomials are Lagrange polynomials through a set of nodal points ξ_q:

$$\phi_p(\xi) = h_p(\xi) = \frac{\prod_{q=0, q\neq p}^{N_P-1}(\xi - \xi_q)}{\prod_{q=0, q\neq p}^{N_P-1}(\xi_p - \xi_q)} = \frac{g(\xi)}{g'(\xi)(\xi - \xi_p)}, \tag{2.35}$$

where $g(\xi)$ is a polynomial of order P with zeros at N_P nodal points ξ_q. An example of the Lagrange expansion basis for $N_P = 6$ is shown in figure 2.3. Lagrange expansion basis consists of N_P polynomials of order $N_P - 1$, therefore

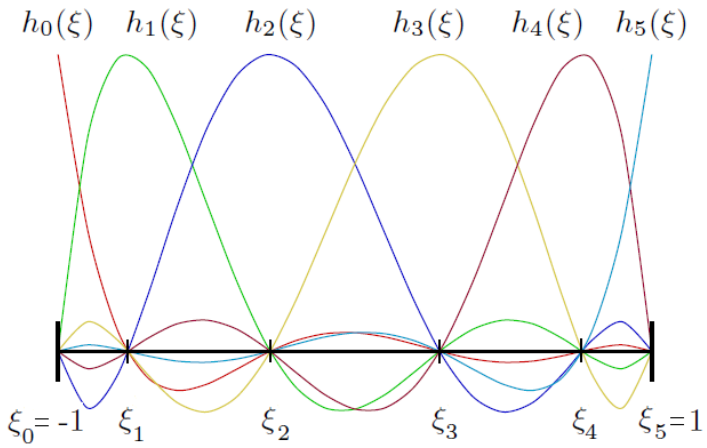

Figure 2.3: Expansion basis of Lagrange polynomials on $\overline{\Omega}$ - $N_P = 6$ Lagrange polynomials of order $P = 5$ defined through Legendre points and $\xi = \pm 1$ (source: Cantwell, 2009).

it is not a hierarchical expansion. It is fully defined by the choice of nodes. Although the choice of points is arbitrary, i.e. one could choose equally spaced nodes, a suitable set of nodal points can lead to an optimised implementation. The appropriate choice of n nodes for polynomials of order $2n-1$ or less can yield an exact integration result, which is a basis of the Gaussian quadrature rule. In Semtex the set of nodes consists of Gauss-Lobatto-Legendre points, that is the end points of the standard element and the zeros of Legendre polynomials on the standard element. Legendre polynomials are a subset of Jacobi polynomials with $\alpha = \beta = 0$ (see Karniadakis & Sherwin, 2005, Appendix A for details on Jacobi polynomials). Therefore the nodal expansion basis $h_p(\xi)$ through points ξ_p (which are zeros of Jacobi polynomial $\mathcal{P}_P^{(0,0)}$) used throughout this work can be written as

$$h_p(\xi) = \begin{cases} 1 & \text{if } \xi = \xi_p \\ \frac{(\xi^2-1)\left[\mathcal{P}_P^{(0,0)(\xi)}\right]'}{P(P-1)\mathcal{P}_{P-1}^{(0,0)}(\xi_p)(\xi-\xi_p)} & \text{otherwise} \end{cases}. \tag{2.36}$$

2.4.4 Numerical integration within the standard element

The previous subsections presented the methods for the approximation of a solution in terms of a polynomial expansion basis. To complete the Galerkin formulation (2.22) one needs a method for evaluating integrals of the form:

$$(1, u(\xi)) = \int_{\overline{\Omega}} u(\xi) d\xi. \tag{2.37}$$

The Gaussian quadrature provides a very accurate approximation to the integral (2.37)

$$\int_{-1}^{1} u(\xi)d\xi \approx \sum_{q=0}^{Q-1} w_q u(\xi_q), \tag{2.38}$$

where w_q are called weights of the quadrature and ξ_q are Q distinct points in $\overline{\Omega}$. Using expansion basis (2.36) one can represent the integrand as

$$u(\xi) = \sum_{q=0}^{Q-1} u(\xi_q) h_q(\xi) + \epsilon(\xi), \tag{2.39}$$

where $\epsilon(\xi)$ is an approximation error. Substituting (2.39) into (2.38) yields

$$\int_{-1}^{1} u(\xi)d\xi = \sum_{q=0}^{Q-1} w_q u(\xi_q) + R(u), \tag{2.40}$$

where

$$w_q = \int_{-1}^{1} h_q(\xi)d\xi, \tag{2.41}$$

$$R(u) = \int_{-1}^{1} \epsilon(\xi)d\xi. \tag{2.42}$$

For the Lagrange polynomial expansion basis based on Gauss-Lobatto-Legendre points the integration is exact ($R(u) = 0$) if $u(\xi) \in \mathcal{P}_{2Q-3}([-1, 1])$. Also, the weights w_q depend only on the expansion basis, therefore they can be precomputed for a standard element. In order to evaluate the integral on an arbitrary

element $e = [x_e, x_{e+1}]$ one needs to use mapping χ_e^{-1} (2.28)

$$\begin{aligned}
\int_a^b u(x)dx &= \int_{x_e}^{x_{e+1}} \sum_q \hat{u}_q h_q^e(x)dx \\
&= \sum_q \hat{u}_q \int_{x_e}^{x_{e+1}} h_q^e(x)dx \\
&= \sum_q \hat{u}_q \int_{-1}^{1} h_q(\chi_e^{-1}(x))\frac{dx}{d\xi}d\xi \\
&= \sum_q \hat{u}_q \int_{-1}^{1} h_q(\chi_e^{-1}(x))\frac{dx}{d\xi}d\xi \\
&= \frac{x_{e+1} - x_e}{2} \sum_q \hat{u}_q w_q. \qquad (2.43)
\end{aligned}$$

A constant $\frac{x_{e+1} - x_e}{2}$ is precomputed for all elements and w_q is defined by equation (2.41).

2.4.5 Numerical derivation

The derivative of $u^\delta(\xi)$, given the expansion basis (2.36), is evaluated as

$$\frac{du^\delta(\xi)}{d\xi} = \frac{d}{d\xi}\sum_q \hat{u}_q h_q(\xi) = \sum_q \hat{u}_q \frac{dh_q(\xi)}{d\xi}. \qquad (2.44)$$

Therefore the evaluation of $\frac{du^\delta(\xi)}{d\xi}$ is dependent on the derivative of expansion polynomials. As we are usually interested in the value of derivatives at nodal points ξ_p, the appropriate $\frac{dh_q(\xi)}{d\xi}\big|_{\xi=\xi_p}$ can be precomputed and expressed as a derivation matrix $\mathbf{D}$ with elements

$$d_{pq} = \frac{dh_q(\xi)}{d\xi}\Big|_{\xi=\xi_p}. \qquad (2.45)$$

The derivative (2.44) can then be evaluated as

$$\frac{du^\delta}{d\xi}\Big|_{\xi=\xi_p} = \sum_{q=0}^{Q-1} d_{pq} u(\xi_q), \tag{2.46}$$

or

$$\begin{bmatrix} \frac{du^\delta}{d\xi}\big|_{\xi=\xi_0} \\ \vdots \\ \frac{du^\delta}{d\xi}\big|_{\xi=\xi_q} \\ \vdots \\ \frac{du^\delta}{d\xi}\big|_{\xi=\xi_{Q-1}} \end{bmatrix} = \mathbf{D} \begin{bmatrix} u(\xi_0) \\ \vdots \\ u(\xi_q) \\ \vdots \\ u(\xi_{Q-1}) \end{bmatrix}. \tag{2.47}$$

In a similar fashion as in (2.43) one can also evaluate the derivative for any point $x = x_0$ in Ω:

$$\frac{u^\delta(x)}{dx}\Big|_{x=x_0} = \frac{x_{e+1} - x_e}{2} \sum_p \hat{u}_p \frac{dh_p(\xi)}{d\xi}\Big|_{\xi=\chi_e^{-1}(x_0)}. \tag{2.48}$$

2.4.6 Transformations between physical and spectral space

Having defined the expansion basis and basic operations on a standard element, one needs to specify the transformation between functions in real and spectral space. Let us consider the projection of a smooth function $u(\xi)$ on a standard element $\overline{\Omega}$ onto a polynomial expansion $u^\delta(\xi)$. In terms of Galerkin formulation (2.22) this can be expressed as

$$\begin{aligned} (\phi_q(\xi), u^\delta(\xi)) &= (\phi_q(\xi), u(\xi)), \qquad && q = 0, \ldots, N_P - 1, \\ \left(\phi_q(\xi), \sum_p \hat{u}_p \phi_p(\xi)\right) &= (\phi_q(\xi), u(\xi)), \qquad && p, q = 0, \ldots, N_P - 1, \end{aligned} \tag{2.49}$$

which is equivalent to solving the matrix equation

$$\mathbf{M}^e \hat{\mathbf{u}} = \mathbf{f}, \tag{2.50}$$

where

$$\mathbf{M}^e_{pq} = (\phi_p, \phi_q), \qquad \hat{\mathbf{u}} = [\hat{u}_0, \ldots, \hat{u}_{N_P-1}]^T, \qquad \mathbf{f_p} = (\phi_p, u). \tag{2.51}$$

The matrix $\mathbf{M}^e$ is known as the *elemental mass matrix*. In order to project function u on the basis ϕ, the mass matrix needs to be inverted

$$\hat{\mathbf{u}} = (\mathbf{M}^e)^{-1}\mathbf{f}, \tag{2.52}$$

therefore the structure and conditioning of $\mathbf{M}^e$ is very important. Two issues are important here - the cost of constructing a well structured matrix $\mathbf{M}^e$ (which may require numerical integration) and the cost of inverting $\mathbf{M}^e$. In the scope of this work we are interested in the GLL expansion (2.36), and the mass matrix $\mathbf{M}^e = (h_p, h_q)$ is full and has no explicit form. However, if we evaluate its elements using Gaussian quadrature (2.40) we obtain

$$\mathbf{M}^e_{pq} = (h_p, h_q) \approx \sum_{i=0}^{N_P-1} w_i h_p(\xi_i) h_q(\xi_i) = \sum_{i=0}^{N_P-1} w_i \delta_{pi} \delta_{qi} = w_p \delta_{pq} \tag{2.53}$$

using the property of (2.35) where $h_p(\xi_q) = \delta_{pq}$. The approximation of $\mathbf{M}^e$ is diagonal and the error of this approximation is consistent with the approximation error of the expansion. It can be shown that the diagonal elements of the reduced mass matrix are the sums of values in corresponding rows of a mass matrix

evaluated using exact integration (see Karniadakis & Sherwin, 2005, p. 57). This procedure is known as *lumping* of the mass matrix and is commonly used in the finite element method.

Equation (2.52) defines the forward transformation of $u(x)$ to the spectral space. Backward transformation is given by the definition of the approximation (2.29) and can be expressed in discrete form as

$$\mathbf{u} \approx \mathbf{u}^\delta = \mathbf{B}\hat{\mathbf{u}}, \tag{2.54}$$

where $\mathbf{u} = [u(\xi_0), \ldots, u(\xi_{N_P-1}]^T$, $\mathbf{u}^\delta = [u^\delta(\xi_0), \ldots, u^\delta(\xi_{N_P-1}]^T$ and $\mathbf{B}_{pq} = \phi_q(\xi_p)$ is called the *basis matrix*. In case of the GLL Lagrange expansion, the basis matrix becomes

$$\mathbf{B}_{pq} = h_q(\xi_p) = \delta_{pq}, \tag{2.55}$$

so $\mathbf{B}$ is an identity matrix and $u^\delta(\xi_p) = \hat{u}_p$. The values of coefficients of expansion are actually the values of the approximation at nodal points. This does not mean, however, that the coefficients represent exact nodal values of the approximated function $u(x)$.

2.5 Spectral Element Method in 2D

The one-dimensional formulation of the SEM can be easily extended to the two-dimensional case, which is used in Semtex. There are only a few of issues, regarding construction of the basis and numbering of points, which are going to be addressed in this section.

2.5.1 Expansion basis for quadrilateral elements

In the general case, SEM can utilise both triangular and quadrilateral elements. Providing that an appropriate mapping is derived, the element's edges can even be curved. For the purpose of this work only straight edge, quadrilateral, conforming elements are considered.

The standard 2D element is defined as

$$\overline{\Omega} = \{\xi_1, \xi_2 | -1 \leq \xi_1, \xi_2 \leq 1\}, \tag{2.56}$$

where ξ_1, ξ_2 are the local coordinates.

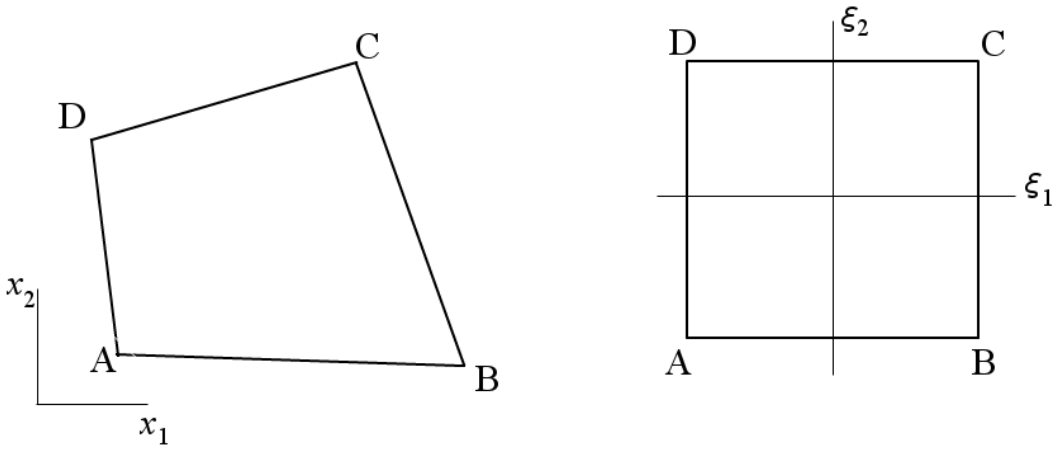

Figure 2.4: 2D coordinate transformation - mapping of a general element $ABCD$ (left) to a standard element $\overline{\Omega}$ (right).

The coordinate transformation from a standard element to a general quadrilateral element Ω_e defined by vortexes $ABCD$ (see figure 2.4) can be expressed

as a mapping $\chi_e(\xi_1, \xi_2) : \overline{\Omega} \to \Omega_e$

$$x_i = \chi_e(\xi_1, \xi_2) = x_i^A \frac{1-\xi_1}{2}\frac{1-\xi_2}{2} + x_i^B \frac{1+\xi_1}{2}\frac{1-\xi_2}{2} + x_i^C \frac{1+\xi_1}{2}\frac{1+\xi_2}{2} + x_i^D \frac{1-\xi_1}{2}\frac{1+\xi_2}{2}. \tag{2.57}$$

It is worth noting that a quadrilateral element $ABCD$ is permissible when all its internal corners have angles less than 180°. Elements with angles close to 180° are strongly advised against in order to minimise approximation errors.

The expansion basis $\phi_{pq}(\xi_1, \xi_2)$ is obtained by a tensor product extension of one-dimensional expansion functions

$$\phi_{pq}(\xi_1, \xi_2) = \phi_p(\xi_1)\phi_q(\xi_2), \qquad 0 \le p \le P_1, \quad 0 \le q \le P_2. \tag{2.58}$$

In general, the polynomial order in each direction does not have to be constant, however for the purposes of this work $P_1 = P_2 = N_P - 1$.

The expansion basis (2.58) maintains the Kronecker delta property of a one-dimensional basis (2.34)

$$\phi_{pq}(\xi_{1i}, \xi_{2j}) = \phi_p(\xi_{1i})\phi_q(\xi_{2j}) = \delta_{pi}\delta_{qj}, \tag{2.59}$$

so each expansion function has a nonzero value only at one nodal point in the standard element. The numbering of points (and therefore basis functions) within an element is discussed in Section 2.5.4

2.5.2 Numerical integration on quadrilateral elements

The integral of $u(\xi_1, \xi_2)$ over the standard element $\overline{\Omega}$ can be expressed in terms of two one-dimensional integrals

$$\int_{\overline{\Omega}} u(\xi_1, \xi_2) d\xi_1 d\xi_2 = \int_{-1}^{1} \left\{ \int_{-1}^{1} u(\xi_1, \xi_2)|_{\xi_2} d\xi_1 \right\} d\xi_2. \tag{2.60}$$

Both integrals can be evaluated using Gauss-Lobatto quadrature defined in (2.40)

$$\begin{aligned} \int_{-1}^{1} u(\xi_1, \xi_2)\big|_{\xi_2} d\xi_1 = f(\xi_{1i}) &\approx \sum_{j=0}^{Q_2-1} w_j u(\xi_{1i}, \xi_{2j}), \\ \int_{\overline{\Omega}} u(\xi_1, \xi_2) d\xi_1 d\xi_2 &\approx \sum_{i=0}^{Q_1-1} w_i f(\xi_{1i}) \end{aligned} \tag{2.61}$$

where w_i, w_j are quadrature weights in ξ_1, ξ_2 direction respectively, and Q_1, Q_2 are number of quadrature points. Throughout this thesis $Q_1 = Q_2 = N_P$ was used.

2.5.3 Numerical differentiation on quadrilateral elements

The two-dimensional expansion of function $u(\xi_1, \xi_2)$ using a tensor product of Lagrange basis (2.36) takes the form

$$u(\xi_1, \xi_2) \approx u^{\delta}(\xi_1, \xi_2) = \sum_{p=0}^{P_1} \sum_{q=0}^{P_2} \hat{u}_{pq} h_p(\xi_1) h_q(\xi_2). \tag{2.62}$$

The partial derivatives are

$$\frac{\partial u^\delta}{\partial \xi_1}(\xi_1, \xi_2) = \sum_{p=0}^{P_1} \sum_{q=0}^{P_2} \hat{u}_{pq} \frac{dh_p(\xi_1)}{d\xi_1} h_q(\xi_2), \tag{2.63}$$

$$\frac{\partial u^\delta}{\partial \xi_2}(\xi_1, \xi_2) = \sum_{p=0}^{P_1} \sum_{q=0}^{P_2} \hat{u}_{pq} h_p(\xi_1) \frac{dh_q(\xi_2)}{d\xi_2}. \tag{2.64}$$

We usually want to evaluate the derivative on nodal points, therefore using the Kronecker delta property $h_p(\xi_q) = \delta_{pq}$, (2.63) can be simplified to

$$\frac{\partial u^\delta}{\partial \xi_1}(\xi_{1i}, \xi_{2j}) = \sum_{p=0}^{P_1} \hat{u}_{pj} \frac{dh_p(\xi_1)}{d\xi_1}\Big|_{\xi_{1i}}, \tag{2.65}$$

$$\frac{\partial u^\delta}{\partial \xi_2}(\xi_{1i}, \xi_{2j}) = \sum_{q=0}^{P_2} \hat{u}_{iq} \frac{dh_q(\xi_2)}{d\xi_2}\Big|_{\xi_{2j}}. \tag{2.66}$$

This can be expressed in matrix form as:

$$\frac{\partial \mathbf{u}}{\partial \xi_1} = \mathbf{D}_{\xi_1} \mathbf{u}, \tag{2.67}$$

$$\frac{\partial \mathbf{u}}{\partial \xi_2} = \mathbf{D}_{\xi_2} \mathbf{u}, \tag{2.68}$$

where $\mathbf{u}$ is a vector of values of u^δ at nodal points (and therefore also coeffcients $\hat{u}_{pq}$) and

$$\mathbf{D}_{\xi_i}[k][l] = \frac{dh_k(\xi_i)}{d\xi_i}\Big|_{\xi_{il}} \tag{2.69}$$

is a derivation matrix that holds the derivatives of expansion basis functions at nodal points. The problem that arises here is the numbering of nodal points and polynomials within the element that would enable construction of the vector u^δ and matrices $\mathbf{D}_{\xi_i}$.

2.5.4 Numbering of nodal points

In order to manage the solution efficiently it is necessary to define a node numbering method within a standard element, what would allow us to write a two-index coefficient $\hat{u}_{pq}$ in vector form. If element e is defined by four corner nodes $e_0, \ldots, e_3$ and the orientation of the element is such that the primary coordinate direction ξ_1 is defined by $e_0 \to e_1$ and the secondary coordinate direction ξ_2 is defined by $e_0 \to e_3$, then the nodal points are numbered in the following order:

- corner nodes $e_0, \ldots, e_3$
- nodes on edge $e_i e_{i+1}$ for $i = 0, 1, 2$
- interior nodes in the row major order: $m = (P_1 - 1) * q + p$ where p changes along ξ_1 and q changes along ξ_2, P_1 is a number of points in the primary direction.

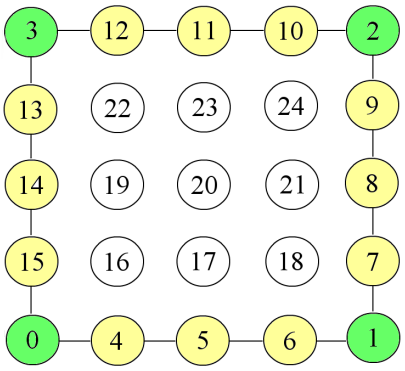

Figure 2.5: Numbering of nodes on a standard quadrilateral element - corner(green), boundary (yellow) and interior nodes (white).

Points in the assembly of elements are numbered in similar fashion. There are five categories of nodes in the assembly:

- boundary corner nodes - element corner nodes that lie at the boundary of the assembly
- boundary edge nodes - element edge nodes that lie at the boundary of the assembly
- interior corner nodes - element corner nodes that lie in the interior of the assembly
- interior edge nodes - element edge nodes that lie in the interior of the assembly
- element-interior nodes

The points are numbered in the order in which the categories were listed above. The schematic numbering for an assembly of 9 elements is shown in figure 2.6.

It is worth noticing that the mesh that is provided to Semtex does not have to follow that ordering. Elements and element corners can be numbered in an arbitrary fashion. The nodes are re-numbered in the pre-processing stage of the computation.

Basis polynomials are numbered in the same way as nodal points, as owing to the Kronecker delta property of Lagrange polynomials each basis function corresponds to one node where it has a non-zero value.

This choice of numbering is beneficial as it separates the boundary nodes. The mass matrix, which represents interactions between expansion modes, has

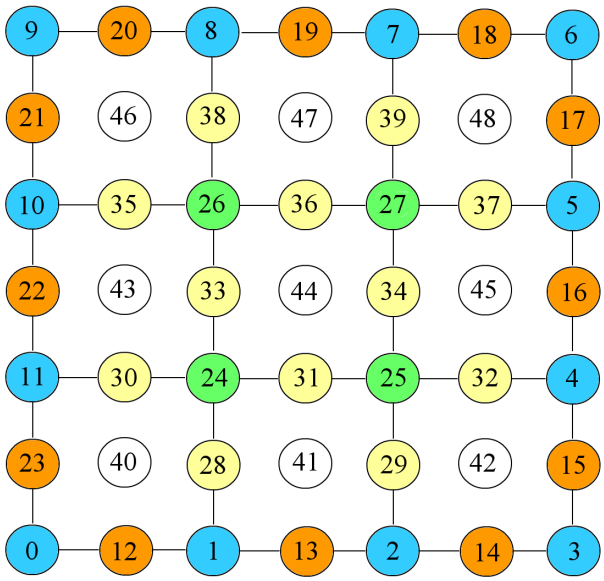

Figure 2.6: Numbering of nodes in an assembly of elements - boundary corner (blue), boundary edge (orange), interior corner (green), interior edge (yellow) and interior nodes (white).

the following structure

$$\mathbf{M} = \mathbf{A}^T \underline{\mathbf{M}^e} \mathbf{A} = \begin{bmatrix} \mathbf{M}_b & \mathbf{M}_{bi} \\ \mathbf{M}_{bi}^T & \mathbf{M}_i \end{bmatrix}, \tag{2.70}$$

where $\underline{\mathbf{M}^e}$ is a block diagonal matrix constructed from elemental mass matrices, $\mathbf{A}$ is an assembly matrix that maps local expansion coefficients to global expansion coefficients (defined in (2.33) for the one-dimensional case), $\mathbf{M}_b$ is a mass sub-matrix that represents boundary-boundary interactions, $\mathbf{M}_{bi}$ is a mass sub-matrix that represents the boundary-interior interactions and $\mathbf{M}_i$ represents only interior modes contribution. The interior matrix maintains its block-diagonal structure.

This kind of decomposition paves the way for a technique called the *static condensation* of the mass matrix. A system of the form

$$\mathbf{M}\mathbf{u} = \mathbf{f}, \tag{2.71}$$

where $\mathbf{u}$ is an unknown vector, typically a global vector of expansion coefficients $\hat{\mathbf{u}}$, can be decomposed into

$$\begin{bmatrix} \mathbf{M}_b & \mathbf{M}_{bi} \\ \mathbf{M}_{bi}^T & \mathbf{M}_i \end{bmatrix} \begin{bmatrix} \mathbf{u}_b \\ \mathbf{u}_i \end{bmatrix} = \begin{bmatrix} \mathbf{f}_b \\ \mathbf{f}_i \end{bmatrix}, \tag{2.72}$$

where $\mathbf{u}_b, \mathbf{u}_i$ and $\mathbf{f}_b, \mathbf{f}_i$ are boundary and interior components of $\mathbf{u}$ and $\mathbf{f}$ respectively. If we pre-multiply this system by a matrix

$$\begin{bmatrix} \mathbf{I} & -\mathbf{M}_{bi}\mathbf{M}_i^{-1} \\ 0 & \mathbf{I} \end{bmatrix}, \tag{2.73}$$

the system decomposes into two steps. The first step is given by

$$(\mathbf{M}_b - \mathbf{M}_{bi}\mathbf{M}_i^{-1}\mathbf{M}_{bi}^T)\mathbf{u}_b = \mathbf{f}_b - \mathbf{M}_{bi}\mathbf{M}_i^{-1}\mathbf{f}_i, \tag{2.74}$$

from where $\mathbf{u}_b$ can be obtained by inversion of the *Schur complement* $\mathbf{M}_b - \mathbf{M}_{bi}\mathbf{M}_i^{-1}\mathbf{M}_{bi}^T$. The second step evaluates $\mathbf{u}_i$ by substituting $\mathbf{u}_b$ into

$$\mathbf{u}_i = \mathbf{M}_i^{-1}\mathbf{f}_i - \mathbf{M}_i^{-1}\mathbf{M}_{bi}^T\mathbf{u}_b. \tag{2.75}$$

$\mathbf{M}_i$ is block-diagonal and can therefore be easily inverted. In the second step, all the operations can be performed on a local elemental level, which means that only the evaluation of boundary conditions requires global assembly.

2.6 Time Advancement Scheme

The numerical code used in this work uses the stiffly-stable multi-step velocity-correction method of Karniadakis *et al.* (1991). The basic idea of this method is to split the time-step into a series of sub-steps, during which contributions from different terms of the Navier-Stokes equation (2.5) are evaluated. Integration of (2.5) yields

$$\mathbf{u}^{n+1} - \mathbf{u}^n = -\int_{t_n}^{t_{n+1}} \nabla p dt + \frac{1}{Re_h} \int_{t_n}^{t_{n+1}} \Delta \mathbf{u} dt - \int_{t_n}^{t_{n+1}} (\mathbf{u} \cdot \nabla)\mathbf{u} dt. \tag{2.76}$$

A multi-step method is formulated around the three terms of the right-hand side above.

In the first step, the integral of the non-linear advection term is evaluated. Throughout this work, and by default in Semtex, this term is represented in the skew-symmetric form

$$\mathbb{N}(\mathbf{u}) = -\frac{1}{2} \left(\mathbf{u} \cdot \nabla \mathbf{u} + \nabla (\mathbf{u} \cdot \mathbf{u}) \right). \tag{2.77}$$

In order to reduce the computational cost, $\mathbb{N}(\mathbf{u})$ is evaluated explicitly using the

Adams-Bashforth scheme of order J_e

$$\int_{t_n}^{t_{n+1}} \mathbb{N}(\mathbf{u})dt = \Delta t \sum_{i=0}^{J_e-1} \beta_i \mathbb{N}(\mathbf{u}^{n-i}), \tag{2.78}$$

where β_i are parameters defined for given J_e (see Gear, 1973).

The linear diffusion term $\mathbb{L}(\mathbf{u}) = \dfrac{1}{Re_h}\Delta\mathbf{u}$ is evaluated implicitly

$$\int_{t_n}^{t_{n+1}} \mathbb{L}(\mathbf{u})dt = \Delta t \sum_{q=0}^{J_i-1} \gamma_q \mathbb{L}(\mathbf{u}^{n+1-q}), \tag{2.79}$$

where J_i is the order of the implicit scheme.

The pressure term is evaluated as

$$\int_{t_n}^{t_{n+1}} -\nabla p dt = -\Delta t \bar{p}^{n+1}, \tag{2.80}$$

where $\bar{p}^{n+1}$ is the pressure field calculated such that the velocity field satisfies the incompressibility condition $\nabla \cdot \hat{\hat{\mathbf{u}}} = 0$.

All three evaluations written in a semi-discrete formulation will give a full multi-step scheme

$$\begin{aligned}
\hat{\mathbf{u}} - \mathbf{u}^n &= -\Delta t \sum_{i=0}^{J_e-1} \beta_i \mathbb{N}(\mathbf{u}^{n-i}) \\
\hat{\hat{\mathbf{u}}} - \hat{\mathbf{u}} &= -\Delta t \bar{p}^{n+1} \\
\mathbf{u}^{n+1} - \hat{\hat{\mathbf{u}}} &= \Delta t \sum_{q=0}^{J_i-1} \gamma_q \mathbb{L}(\mathbf{u}^{n+1-q})
\end{aligned} \tag{2.81}$$

with the condition $\nabla \cdot \hat{\hat{\mathbf{u}}} = 0$. All three steps above demand appropriate boundary

conditions (BC) dependent on the BC's of the original problem (see Karniadakis *et al.*, 1991).

2.6.1 Stiffly-stable scheme

In order to improve the stability of the method, a stiffly-stable scheme is introduced. The stiffly-stable scheme is based on backward differentiation schemes that approximate the time derivative by

$$\frac{\partial \mathbf{u}}{\partial t} \approx \frac{\gamma_0 \mathbf{u}^{n+1} - \sum_{i=0}^{J-1} \alpha_i \mathbf{u}^{n-i}}{\Delta t}, \tag{2.82}$$

where $\gamma_0 = \sum_{i=0}^{J-1} \alpha_i$ is required for consistency. This can be rewritten as

$$\frac{\gamma_0 \mathbf{u}^{n+1} - \sum_{i=0}^{J-1} \alpha_i \mathbf{u}^{n-i}}{\Delta t} = \frac{\sum_{i=0}^{J-1} \alpha_i (\mathbf{u}^{n+1} - \mathbf{u}^{n-i})}{\Delta t}. \tag{2.83}$$

A problem given by

$$\frac{\partial \mathbf{u}}{\partial t} = \mathbf{f} \tag{2.84}$$

can be integrated over (t^{n-i}, t^{n+1}) to yield

$$\begin{aligned} \int_{t^{n-i}}^{t^{n+1}} \frac{\partial \mathbf{u}}{\partial t} dt &= \int_{t^{n-i}}^{t^{n+1}} \mathbf{f} dt, \\ \mathbf{u}^{n+1} - \mathbf{u}^{n-i} &= \int_{t^{n-i}}^{t^{n+1}} \mathbf{f} dt. \end{aligned} \tag{2.85}$$

Substituting this to (2.83) and splitting $\mathbf{f}$ into pressure, advection and diffusion parts gives

$$\frac{\gamma_0 \mathbf{u}^{n+1} - \sum_{q=0}^{J_i-1} \alpha_q \mathbf{u}^{n-q}}{\Delta t} = -\nabla \bar{p}^{n+1} + \sum_{q=0}^{J_e-1} \beta_q \mathbb{N}(\mathbf{u}^{n-q}) + \mathbb{L}(\mathbf{u}^{n+1}), \tag{2.86}$$

where γ_0 and α_q are coefficients of a stiffly-stable scheme of order J_i and β_q are not the same as in (2.78). Karniadakis *et al.* (1991) gives the values for all coefficients of schemes up to third-order. Formulation (2.86) can be written as a three-step method

$$\frac{\hat{\mathbf{u}} - \sum_{q=0}^{J_i-1} \alpha_q \mathbf{u}^{n-q}}{\Delta t} = \sum_{q=0}^{J_e-1} \beta_q \mathbb{N}(\mathbf{u}^{n-q}), \tag{2.87}$$

$$\frac{\hat{\hat{\mathbf{u}}} - \hat{\mathbf{u}}}{\Delta t} = -\nabla \bar{p}^{n+1}, \tag{2.88}$$

$$\frac{\gamma_0 \mathbf{u}^{n+1} - \hat{\hat{\mathbf{u}}}}{\Delta t} = \mathbb{L}(\mathbf{u}^{n+1}). \tag{2.89}$$

Time-stepping algorithm of this form is implemented in Semtex for first, second and third-order integration. Throughout this work the default second-order scheme was used.

2.6.2 High-order pressure boundary condition

One issue that was omitted in previous considerations was the boundary condition for the pressure substep (2.88). It is required that the velocity field $\hat{\hat{\mathbf{u}}}$ is incompressible and satisfies the Dirichlet boundary condition $\hat{\hat{\mathbf{u}}} \cdot \mathbf{n} = \hat{\hat{\mathbf{u}}}^0 \cdot \mathbf{n}$. By

taking the divergence of (2.88) we get

$$\frac{1}{\Delta t}\nabla \cdot \hat{\mathbf{u}} = \Delta \bar{p}^{n+1} \qquad \text{in } \Omega, \tag{2.90}$$

with the boundary condition

$$\frac{\partial \bar{p}^{n+1}}{\partial \mathbf{n}} = -\frac{\mathbf{u}^0 \cdot \mathbf{n} - \hat{\mathbf{u}} \cdot \mathbf{n}}{\Delta t} \qquad \text{on } \partial\Omega. \tag{2.91}$$

Although this formulation of boundary condition is very efficient, it may lead to erroneous results (Marcus, 1984). The correct BC derived from (2.81) is

$$\frac{\partial \bar{p}^{n+1}}{\partial \mathbf{n}} = \mathbf{n} \cdot \left[\sum_{i=0}^{J_e-1} \beta_i \mathbb{N}(\mathbf{u}^{n-i}) + \sum_{q=0}^{J_i-1} \gamma_q \mathbb{L}(\mathbf{u}^{n+1-q}) \right] \qquad \text{on } \partial\Omega. \tag{2.92}$$

This formulation, however, involves terms dependent on $\mathbf{u}^{n+1}$ and leads to a coupled system. The obvious choice is to replace the implicit evaluation of $\mathbb{L}$ on the boundary with an explicit one:

$$\frac{\partial \bar{p}^{n+1}}{\partial \mathbf{n}} = \mathbf{n} \cdot \left[\sum_{i=0}^{J_e-1} \beta_i \mathbb{N}(\mathbf{u}^{n-i}) + \sum_{q=0}^{J_e-1} \beta_q \mathbb{L}(\mathbf{u}^{n-q}) \right] \qquad \text{on } \partial\Omega. \tag{2.93}$$

Orszag *et al.* (1986) showed, that this formulation leads to instabilities, but a stable scheme can be obtained by splitting the linear term into a solenoidal part, solved explicitly, and an irrotational part $\nabla(\nabla \cdot \mathbf{u})$, treated implicitly:

$$\frac{\partial \bar{p}^{n+1}}{\partial \mathbf{n}} = \mathbf{n} \cdot \left[\sum_{i=0}^{J_e-1} \beta_i \mathbb{N}(\mathbf{u}^{n-i}) + \sum_{q=0}^{J_i-1} \gamma_q \nabla(\nabla \cdot \mathbf{u}^{n+1-q}) + \sum_{q=0}^{J_e-1} \beta_q(-\nabla \times (\nabla \times \mathbf{u}^{n-q})) \right]. \tag{2.94}$$

This decouples the system as $\nabla(\nabla \cdot \mathbf{u}) = 0$ due to the incompressibility condition.

2.6.3 Flowrate control

Maintaining a constant mass flow throughout the simulation is an important problem to address. In a case where the Dirichlet condition can be prescribed at the inflow, flowrate will be fixed by this condition. When periodicity in the streamwise direction is demanded, the flow would lose the momentum of its initial state, due to the viscosity, and the flowrate would drop. This problem can be solved by prescribing an underlying pressure gradient as a forcing $\mathbf{f}$ of the flow:

$$\frac{\partial \mathbf{u}}{\partial t} + (\mathbf{u} \cdot \nabla)\mathbf{u} = -\nabla p + \nu \Delta \mathbf{u} + \mathbf{f}. \tag{2.95}$$

In such a situation the flowrate will be constant or oscillate around the level imposed by $\mathbf{f}$. In geometries like BFS choosing $\mathbf{f}$ to match the desired flowrate $\overline{Q}$ for a turbulent flow is difficult. Therefore a different approach is preferred, where instead of applying additional forcing, Q is set on a fixed level by superposition of a Green's function $\mathbf{u}_g$ with the solution $\mathbf{u}$:

$$\mathbf{u} \leftarrow \mathbf{u} + \alpha(t)\mathbf{u}_g, \tag{2.96}$$

where $\alpha(t)$ is a parameter evaluated every timestep and the left-hand-side $\mathbf{u}$ is the corrected solution with the desired flowrate $\overline{Q}$. The arrow indicates that the original right-hand-side solution $\mathbf{u}$ is being corrected by superposition with $\mathbf{u}_g$. The adjustment of $\mathbf{u}$ is performed at the end of each time-step.

The Green's function $\mathbf{u}_g$ is a solution of the Stokes equation:

$$\frac{\partial \mathbf{u}_g}{\partial t} = -\nabla p + \nu \Delta \mathbf{u}_g \tag{2.97}$$

with the same boundary conditions as the original problem. As this is a linear equation, the superposition $\mathbf{u}+\mathbf{u}_g$ is still the solution of the original Navier-Stokes equation (2.1). The Stokes solution $\mathbf{u}_g$ is precomputed at the beginning of the simulation, and the only thing left to be adjusted dynamically is $\alpha(t)$:

$$\alpha(t) = \frac{\overline{Q} - Q(\mathbf{u})}{Q(\mathbf{u}_g)}, \tag{2.98}$$

where $\overline{Q}$ is the prescribed flowrate, $Q(\mathbf{u})$ is the current unmodified flowrate and $Q(\mathbf{u}_g)$ is the flowrate of the Stokes solution. Flowrates can be evaluated at any selected cross-flow plane in the domain. The problem, however, arises in geometries where the Stokes solution is singular. This happens in the vicinity of the corner in the BFS flow. In such cases the correction is only applied to the periodic inflow part of the flow (see the blue region in figure 2.1 a) upstream of the step edge. This ensures the prescribed flowrate in the entire domain.

A concern was raised that this technique introduces a discontinuity at the end of the periodic inflow zone. However, no problems were observed during simulations. The reason for that might be the fact that the boundary of the periodic region coincided with element boundaries. Since the C^0 continuity between elements is enforced, Semtex corrected for this discontinuity automatically.

2.7 Flow Field Filtering

The analysis of the small-scale energy transfer presented in Section 4.5 requires a spatial filtering technique to separate scales of the flow. Two possible techniques for the spectral element method are provided by Levin *et al.* (1997) and Blackburn & Schmidt (2003). The type of the technique used depends on the polynomial expansion base.

In the case of a hierarchical expansion, a low-pass Boyd-Vandeven spectral filter is feasible. In one space dimension the forward and inverse transformation between real and spectral space is defined by

$$\hat{\mathbf{u}} = \mathbf{B}^{-1}\mathbf{u}, \qquad \mathbf{u} = \mathbf{B}\hat{\mathbf{u}}, \tag{2.99}$$

where $\mathbf{B}_{pq} = \phi_p(\xi_q)$ is a basis matrix. The spectral filter can be applied in the space of coefficients $\hat{\mathbf{u}}$

$$\tilde{\mathbf{u}} = \mathbf{B}\tilde{\hat{\mathbf{u}}} = \mathbf{B}\mathbf{L}\hat{\mathbf{u}} = \mathbf{B}\mathbf{L}\mathbf{B}^{-1}\mathbf{u} = \mathbf{F}\mathbf{u}, \tag{2.100}$$

where $\mathbf{L} = \mathrm{diag}(l_0, \ldots, l_N)$ is a diagonal matrix of filter coefficients l_i. The coefficients can be arbitrarily chosen. One example is a cut-off filter where $f_i = 0$ for $i \geq i_{cut-off}$. Another example is the Boyd-Vandeven filter, where the coefficients change smoothly in spectral space (Levin *et al.*, 1997). Figure 2.7 presents schematically the Boyd-Vandeven filtering procedure.

If the expansion basis is nodal, like the GLL Lagrange expansion used in this

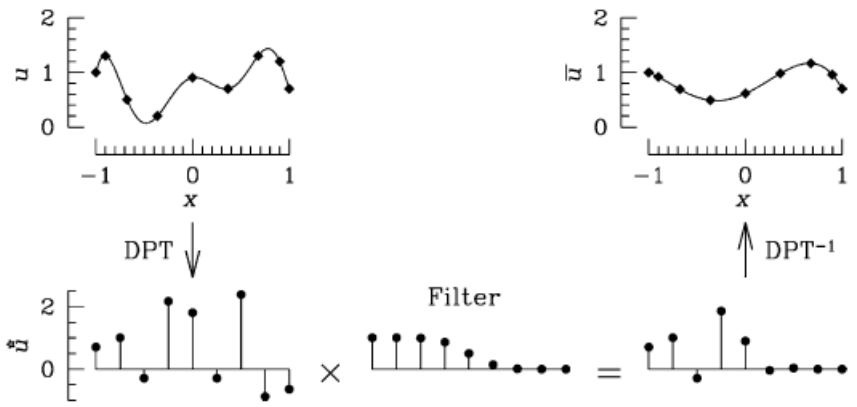

Figure 2.7: Boyd-Vandeven filtering procedure - low-pass filter for hierarchical (modal) polynomial basis. DPT stands for Discrete Polynomial Transform (source: Blackburn & Schmidt, 2003).

work, the filtering can be performed by projecting the solution on a lower order set of basis functions of the same family, and then back to the original basis. If I_N^M is an operator that interpolates the polynomial of order N (with $N_P = N+1$ nodes) to a set of $M_P = M+1$ nodal points, then

$$\tilde{\mathbf{u}} = \mathbf{I}_M^N \mathbf{I}_N^M \mathbf{u} = \mathbf{F}\mathbf{u}. \tag{2.101}$$

This process is shown schematically in figure 2.8

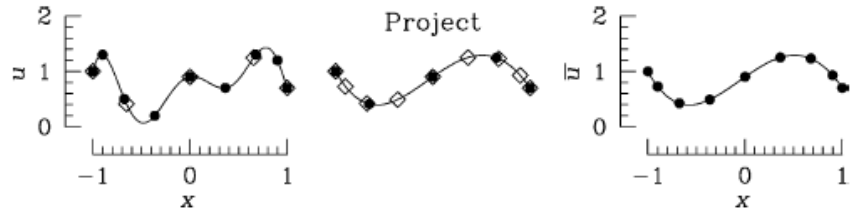

Figure 2.8: Nodal filtering procedure - low-pass filter for non-hierarchical (nodal) polynomial basis (source: Blackburn & Schmidt, 2003).

The operators $\mathbf{I}_N^M$ can be derived using Lagrange interpolants through GLL points:

$$I_{N\,jk}^{M} = \frac{\prod_{p=0}^{N}(x_j - x_p)}{\prod_{\substack{q=0 \\ q\neq k}}^{N}(x_j - x_q)}, \quad j = 0, \ldots, M, \quad k = 0, \ldots, N. \tag{2.102}$$

Typically $M_P = (N_P + 1)/2$ where / represents integer division. It is worth noting that this filtering technique preserves C^0 continuity of the solution across the elements, as the end values of the solution at the element are preserved.

Both of the above techniques are easily extended to the two-dimensional case. Blackburn & Schmidt (2003) provide the implementation of the described filtering methods to Dynamic Smagorinsky model used for LES of turbulent channel flow.

Chapter 3

Code Validation and Preliminary Simulations

The first part of this chapter treats previous applications of the spectral element method, Semtex in particular, to different turbulent flow problems. The goal is to demonstrate the capability of the code to deal with the turbulent backward-facing flow case.

In the second part of the chapter a number of preliminary simulations are described. The goal was to come up with a valid initial condition and find appropriate parameters for the main simulation. Firstly, the turbulent channel flow case was run to generate a turbulent flow which will serve as an inflow for the later 3D BFS simulation. Once that was achieved, a two-dimensional simulation of the flow over BFS with prescribed parabolic profile at the inflow was performed as a first attempt for the simulation in a BFS geometry. Finally the two initial cases were combined and a series of fully 3D, turbulent inflow simulations were run using a different order of interpolation polynomials (p-refinement) to perform

a convergence study and establish minimal resolution requirements.

3.1 Code Validation

The numerical code, called Semtex, used in this study was developed by Hugh Blackburn from Monash University, Australia. A detailed description of the details of the code was published in Blackburn & Sherwin (2004). The method was extensively validated for turbulent flow simulations. The best summary is the chapter 9.3 of the book by Karniadakis & Sherwin (2005), where the authors discuss different aspects of application of SEM to DNS simulations using the turbulent channel flow as an example. Analysis of the influence of the grid refinement upon the solution is performed and some rule-of-thumb recommendations for mesh generation are constructed. The authors compare the DNS results with previous simulations by Moser *et al.* (1999). They also discuss the problem of simulation stabilisation at high Reynolds numbers.

Apart from the plain channel flow, some more complex geometries have been solved owing to geometrical flexibility of SEM. An example is the study by Chu & Karniadakis (1993), who performed DNS of turbulent flow in a channel with streamwise riblets mounted on one of the surfaces. The accuracy of the computations is established by comparing flow quantities corresponding to the smooth wall with previous DNS results of Kim *et al.* (1987). On the riblet mounted wall the comparison is made with experimental results by Walsh (1980).

The Semtex's lineage can be traced back to the spectral element method code Prism by Henderson & Karniadakis (1995). The noteworthy difference is that Semtex has capabilities of dealing with both Cartesian and cylindrical coordi-

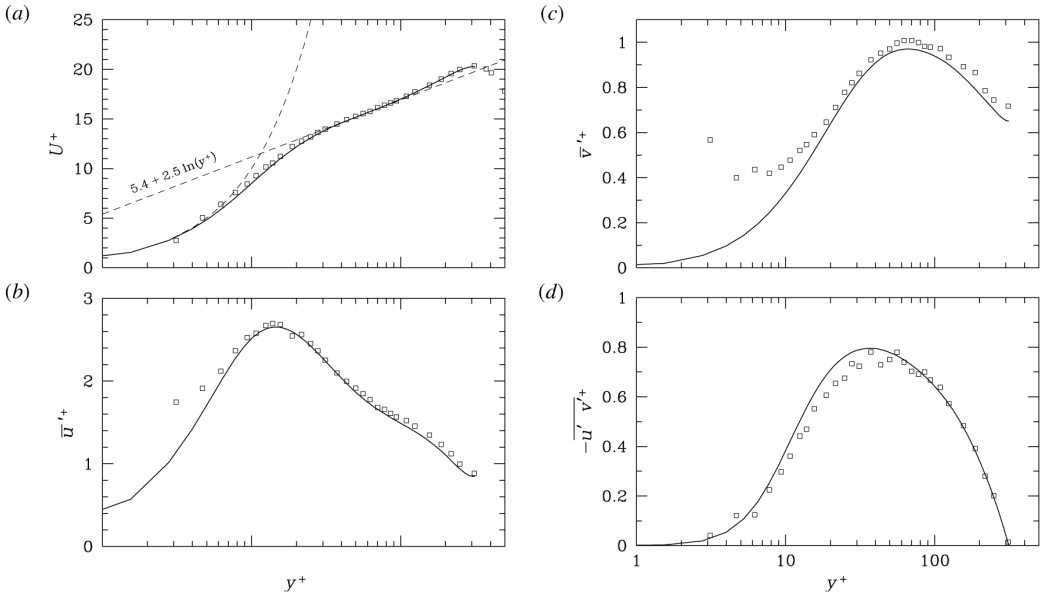

Figure 3.1: Turbulent pipe flow simulation of Blackburn *et al.* (2007) - comparison of flow profile data for the smooth-walled pipe at $Re = 10 \times 10^3$ (solid lines) with LDA-based values of den Toonder & Nieuwstadt (1997) (squares). (a) mean flow, with dashed lines for linear sublayer and fitted log law; (b) rms axial velocity fluctuation; (c) rms radial velocity fluctuation; (d) Reynolds shear stress (source Blackburn *et al.*, 2007)

nates. Due to this feature, Semtex has been used on many occasions for simulations of pipe or stenotic flows (see Sherwin & Blackburn, 2005 or Blackburn & Sherwin, 2007). The DNS of a turbulent flow in a pipe was conducted by Chin *et al.* (2010) providing an extensive study of the influence of the pipe length on turbulence statistics. The investigation by Blackburn *et al.* (2007) focuses on a laminar and turbulent flow inside a wavy-walled pipe. The authors validate the code by performing a DNS simulation of a smooth-walled pipe and directly comparing results with a corresponding experiment by den Toonder & Nieuwstadt (1997) (see figure 3.1). The agreement is excellent except in the near wall region, where inaccuracies of the experimental estimates of fluctuating axial and radial velocities are evident. Recent study by Cantwell *et al.* (2010) addresses the transient growth in a flow through a sudden pipe expansion, which is somewhat similar to the backward facing step case.

Semtex was also used for simulations of turbulent flows in the Cartesian coordinates. Blackburn & Schmidt (2003) studied the feasibility of the spectral element method for LES. The authors compared different filtering techniques with the experimental data of Hussain & Reynolds (1975), Wei & Willmarth (1989) and numerical simulations of Moser *et al.* (1999). The results for the no-model case (i.e. under-resolved DNS, figure 3.2) provide a good match to the DNS data for the mean and wall-normal fluctuating velocities in the viscous sublayer and into the start of the buffer layer, although u^+_{rms} is high, indicating that the near-wall region is, as expected, slightly under-resolved. However the predicted mean velocity in the outer region ($y^+ > 35$) is signicantly low, of order 5% at the centre plane. The application of the dynamic sub-grid scale models (DSM-P, DSM-L,

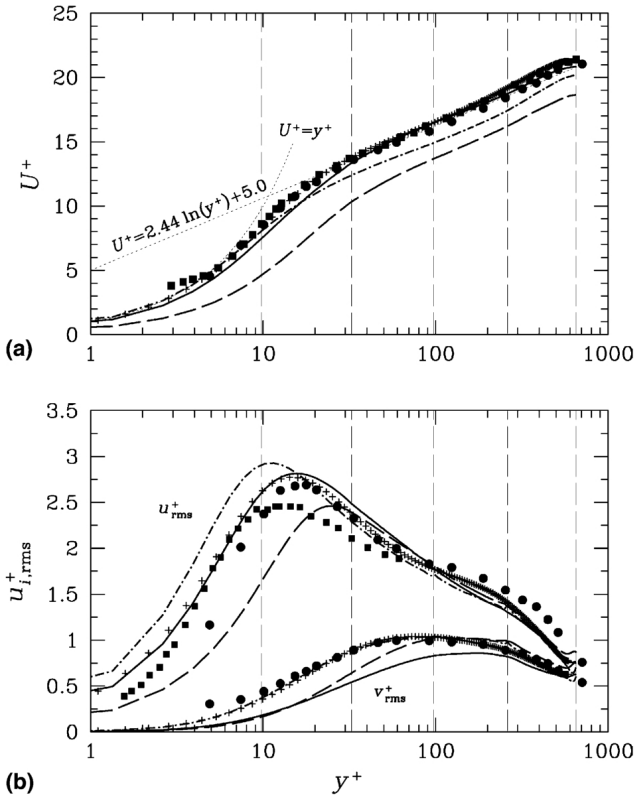

Figure 3.2: Turbulent channel flow simulation of Blackburn & Schmidt (2003) - channel flow comparison data for $Re_\tau = 650$, (a) mean and (b) rms (u^+, streamwise; v^+, wall-normal) velocity profiles: ■, •, experimental measurements (Hussain & Reynolds, 1975, Wei & Willmarth, 1989); +, DNS data (Moser *et al.*, 1999). Non-dynamic spectral element simulations: dot-dashed line - no SGS model; dashed line - Smagorinsky model, $c_S = 0.12$, without wall damping; solid line - Smagorinsky model, $c_S = 0.12$, van Driest wall damping, $A^+ = 26$. Vertical dashed lines indicate element boundaries (source: Blackburn & Schmidt, 2003)

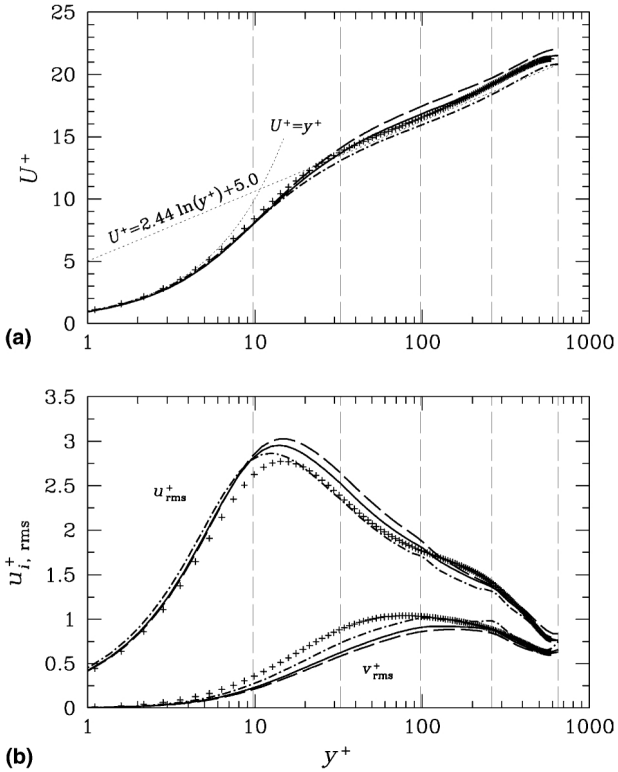

Figure 3.3: Dynamic sub-grid scale models in turbulent channel flow simulation of Blackburn & Schmidt (2003) - channel flow dynamic model simulation results for $Re_\tau = 650$ showing the influence of filtering technique: (a) mean and (b) rms (u^+, streamwise; v^+, wall-normal) velocity profiles. + - DNS data; dot-dashed line - DSM-P filtering; solid line - DSM-L filtering; dashed line - DSM-M filtering (source: Blackburn & Schmidt, 2003)

DSM-M) with filters designed for the spectral element method yielded significant improvements (figure 3.3).

This review shows that the code has been used for a wide range of DNS of turbulent flows in different geometries, starting from plane pipe and channel flows, to expanding and stenotic pipes. Given the extensive validation of the method in general, and the Semtex code in particular, by other authors, we decided that it is not necessary to validate it any further. The publications in well established journals provide sufficient level of trust in the capabilities of this code.

3.2 Preliminary Simulations

The goal of the preliminary simulations was to develop the initial condition that could be used in the main simulation, as well as to determine what set of parameters can be used given the computational resources available. The first attempted simulation was a channel flow, which was run in order to establish a turbulent flow, which would later serve as an input to 3D BFS simulation. The next step was to run 2D, and then full three dimensional backward facing step simulation using the data from channel flow as an inflow. Apart from getting the initial condition for the main simulation, those preliminary runs allowed for checking the behaviour of the inlet and outlet boundary conditions.

3.2.1 Turbulent channel flow simulation

A simulation of turbulent flow in a spanwise and streamwise periodic channel was run to establish turbulent flow, but not until obtaining fully converged statistics.

The criterium for a turbulent flow was the linearity of the Reynolds stress component $\overline{u'v'}$ (see figure 3.4). The dimensions of the channel were $L_x = 8$ in the streamwise, $L_y = 1$ in the vertical and $L_z = 2\pi$ in the spanwise directions. Previous investigations of Blackburn & Schmidt (2003) have shown that these domain extents are sufficient to overcome most contamination effects resulting from periodic correlations. The spanwise and vertical dimensions of the channel were chosen to fit in the inflow section of the domain discussed in Section 2.2.1. The streamwise dimension, which had to match the regeneration length L_i of the main simulation, is a compromise between the possible periodic correlation of velocity fields and the computational cost. The periodic correlations problem and its influence on the BFS flow dynamics is discussed further in Chapter 4.

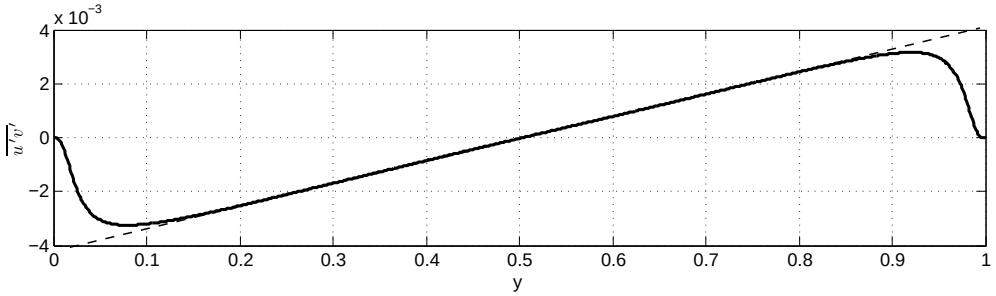

Figure 3.4: Spanwise and streamwise averaged Reynolds stress component - $\overline{u'v'}$ is linear in the main flow section of the channel.

The Reynolds number based on the channel half-height and mean velocity was $Re = 3000$ with a friction velocity based Reynolds number $Re_\tau \approx 195$. This was chosen to match later BFS simulation with $Re_h = 6000$. Turbulence was triggered by adding Gaussian noise to the initial condition, which was a parabolic velocity profile.

Having established turbulent flow in a channel, streamwise periodic boundary

conditions were changed to the copy BC for the inflow with the regeneration plane at 8 channel heights from the inlet plane. The domain was extended to 12 channel heights. The outflow plane had the Neumann no-stress condition prescribed. This set-up allowed for testing the inflow and outflow boundary condition.

Figure 3.5 presents the instantaneous profile of u, v and w velocities at the centre of the channel. Interesting behaviour of w can be noted in the periodic regeneration region ($-12 < x < -4$). The origin of small-scale oscillations is unknown. They vanish soon after leaving the periodic section.

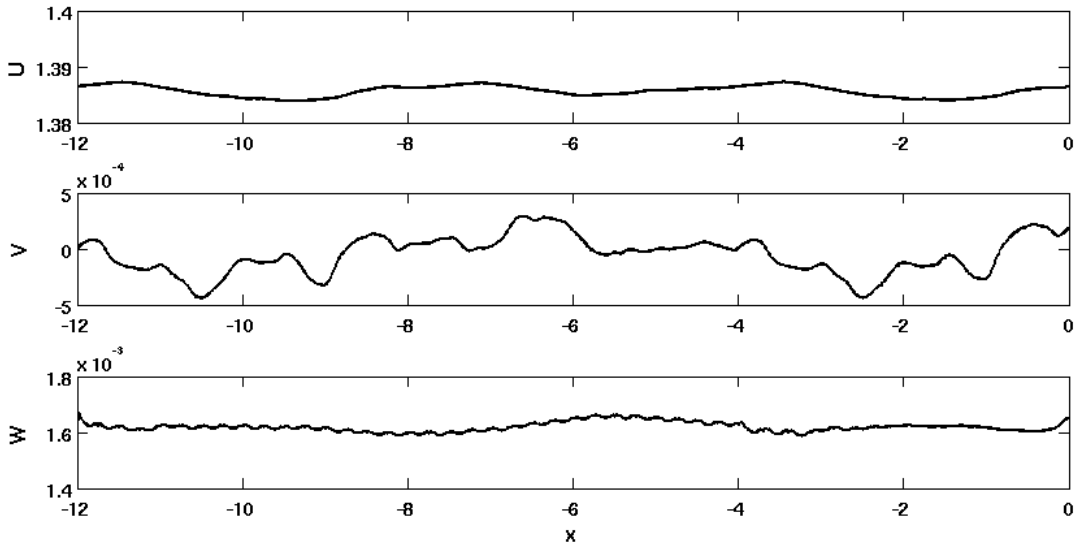

Figure 3.5: Infow-outflow turbulent channel flow simulation - instantaneous values of u, v, w.

Figure 3.6 shows the instantaneous skin friction coefficient along the channel. It is clear that the effect of the no-stress boundary condition is very local and is confined to 0.5 channel heights from the outlet plane.

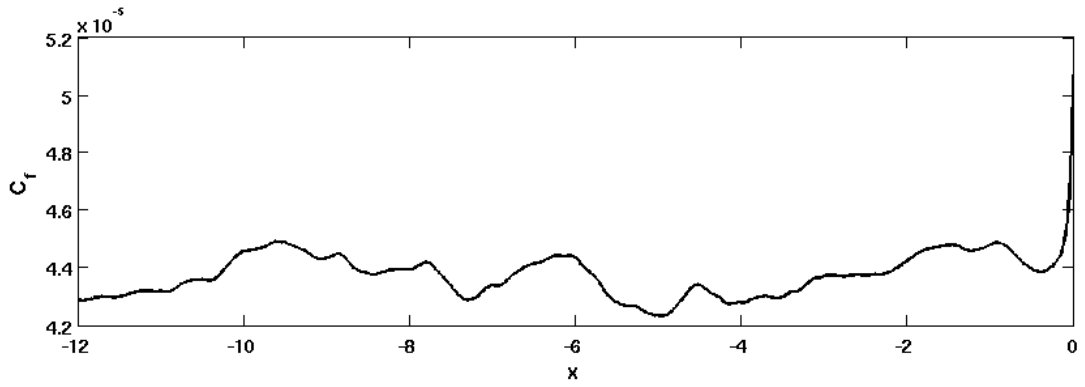

Figure 3.6: Infow-outflow turbulent channel flow simulation - coefficient of friction is affected only locally by the no-stress boundary condition.

3.2.2 Laminar inflow backward-facing step flow simulation

The first test of the backward-facing step flow simulation was a 2D computation of the flow in a channel with a sudden expansion using a parabolic profile inlet condition and Reynolds number $Re = 5000$. The initial condition was a laminar channel flow profile placed in the upper part of the domain, while the lower part of the outflow channel was stationary ($\mathbf{u} = 0$). High Re ensured that Kelvin-Helmholtz oscillations occurred, as can be seen in the figure 3.7. As this simulation was run purely for practising the use of Semtex and preparing for 3D simulations of BFS, no data was collected for analysis.

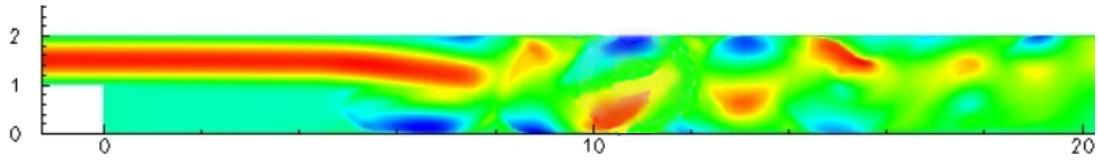

Figure 3.7: Laminar inlet BFS simulation - U velocity contours show Kelvin-Helmholtz oscillations.

3.2.3 Turbulent inflow backward-facing step flow simulation

3.2.3.1 Initial condition

Having obtained the results of simulations described in Sections 3.2.1 and 3.2.2, it was possible to construct a preliminary initial condition by copying the periodic turbulent channel flow velocity and pressure fields and pasting it consecutively into the upper section of the outlet channel with it. Therefore the initial configuration was similar to the 2D laminar inflow case, but the flow in the top part of the outflow channel was a turbulent channel flow, with the result of Section 3.2.1 repeated periodically through the streamwise length of the domain. The lower part of the outflow channel was still at rest. Starting with this initial condition a series of simulations were made by increasing the number of planes in the spanwise direction and increasing the polynomial order. This way a proper initial condition was obtained for a backward-facing flow with $Re_h = 6000$, $N_P = 7$, $N_Z = 128$.

3.2.3.2 Preliminary BFS simulations

Using the initial condition described in section 3.2.3.1, a set of three simulations with different polynomial order ($N_P = 7, 9, 11$) was performed in order to establish maximum Re_h and resolution requirements for the main simulation. Table 3.1 shows parameters of those initial simulations.

Mesh	**Time**	**NZ**	**dt**	**No of points**	X_r
NP7	80	128	0.001	$17.8 \cdot 10^6$	7.4
NP9	20	128	0.0005	$29.5 \cdot 10^6$	7.9
NP11	60	128	0.0005	$44 \cdot 10^6$	8.1

Table 3.1: Initial simulations parameters - $Re_h = 6000$

In order to test the convergence of the solution, the spanwise and time averaged coefficients of friction at the bottom wall are plotted against the distance from the step. Figure 3.8 clearly shows that cases NP9 and NP11 collapse reasonably well and NP7 is only slightly above the converged profile in the reattachment zone. The reattachment positions X_r for NP9 and NP11 cases are close to $X_r = 8$ reported by Armaly *et al.* (1983) for turbulent flow in a BFS geometry with the expansion ratio $ER = 2$, and withing 2% from each other. The problem of all three preliminary simulations is a relatively short averaging time, especially in the NP9 case, which results in not fully converged statistics. Such compromise was necessary due to limited computational resources. While making judgements about the parameters of the main simulation based on those results was somewhat risky, the grid resolution analysis presented in Chapter 4 confirms that the decision regarding the mesh resolution and Re_h was correct. The selected parameters are presented in Section 4.1.

These preliminary simulations also provided an initial condition for the main

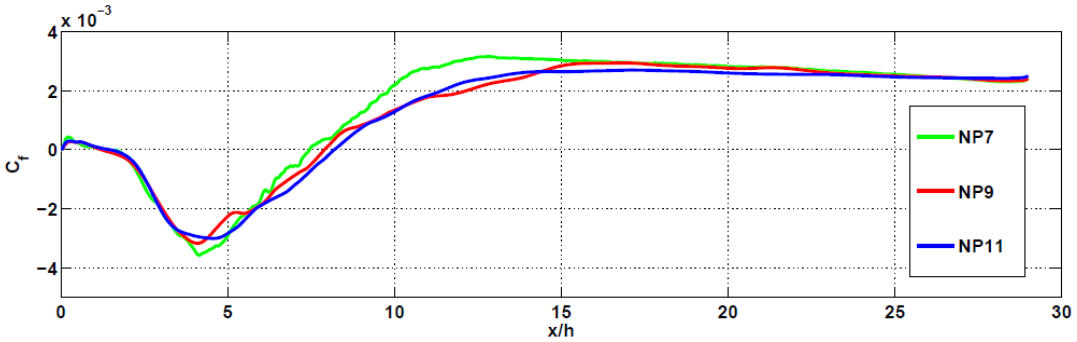

Figure 3.8: Initial simulations - time and spanwise averaged coefficient of friction on the step wall in streamwise direction for different order of p-refinement.

simulation. The time of transition of developed BFS flow from $Re_h = 6000$ to the new Re_h was significantly shorter than the time needed to initialise the simulation with turbulent channel flow initial condition.

Chapter 4

Main Simulation Results

4.1 Simulation Parameters

Based on the preliminary simulations described in Chapter 3, the parameters for the main simulation were defined (see Table 4.1). The maximum Reynolds number, given the limitations of the code and resources, was derived using the $N \sim Re^{9/4}$ criterion (Davidson, 2007, pg. 424), where N is the total number of points. Semtex was able to process the 2845 element mesh on the HECToR XT4 system for $N_P \leq 11$, giving the increase in total number of points, as compared with $N_P = 7$ simulation, equal ≈ 2.5. This allowed for the increase in Reynolds number by a factor of 1.5, therefore the main simulation was run with the Reynolds number $Re_h = 9000$. Note the resolution in the spanwise direction was not changed.

Simulation name	bfs7
Reynolds number	9000
Number of elements	2845
Polynomial order	11
N_Z	128
Total number of points	$44 \cdot 10^6$
Simulation time $t \cdot U_b/h$	250
Time step	0.0005
Resources	$50000 CPUh$

Table 4.1: Overview of the main simulation parameters

4.2 Verification of Results

In order to build confidence in the results of the main simulation, a number of characteristics were compared with the data available in the literature. The velocity profile generated by the copy inflow condition was compared with the results of other turbulent channel flow simulations. The standard quantity of interest in every BFS flow is the reattachment length, usually calculated using the average coefficient of friction distribution at the bottom wall. Therefore those two quantities were examined and compared with previous findings. In order to confirm that the streamwise and vertical resolution is adequate, the grid spacing was compared with the Kolmogorov scale. Finally, the spanwise modal energy decay in the shear layer was investigated in order to check whether the N_Z resolution was adequate.

4.2.1 Inlet

Figure 4.1 shows the U velocity profile in the inlet section of the domain. The statistics were collected over an averaging time of $T_{ave} \approx 200h/U_b$ with a sampling

frequency $f_{ave} = 40U_b/h$. Profiles are compared with results of turbulent channel flow DNS simulations of Kim *et al.* (1987, KMM87), Moser *et al.* (1999, MKM99) as well as the backward-facing step simulation of Le *et al.* (1997, LMK97).

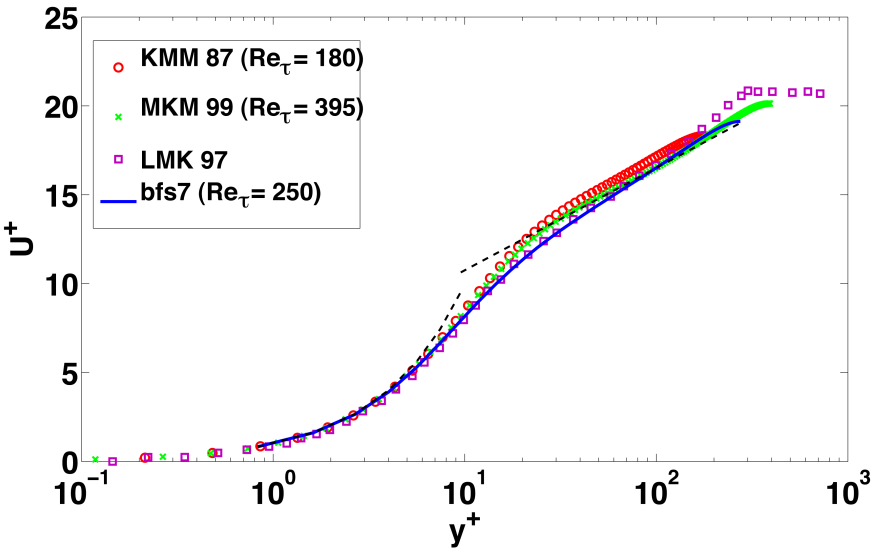

Figure 4.1: Inlet U profile - time and spanwise averaged at $x = -2.0$. bfs7 denotes current simulation results.

The results collapse reasonably well. Interestingly, the current simulation shows the same slope in the log layer as the LMK97 profile, which is slightly different from the channel flow profiles of KMM87 and MKM99. In absence of the present simulation data, one could conclude that the difference is caused by turbulent inflow condition in the BFS simulation, however the agreement between LMK97 and bfs7, where both turbulent inflow conditions are different, points to the fact that it is the presence of the step that causes the difference in the velocity profile slopes in the boundary layer.

Figure 4.2 presents the turbulence intensity profiles. Results are compared with the Moser *et al.* (1999) turbulent channel flow simulation. The figure shows

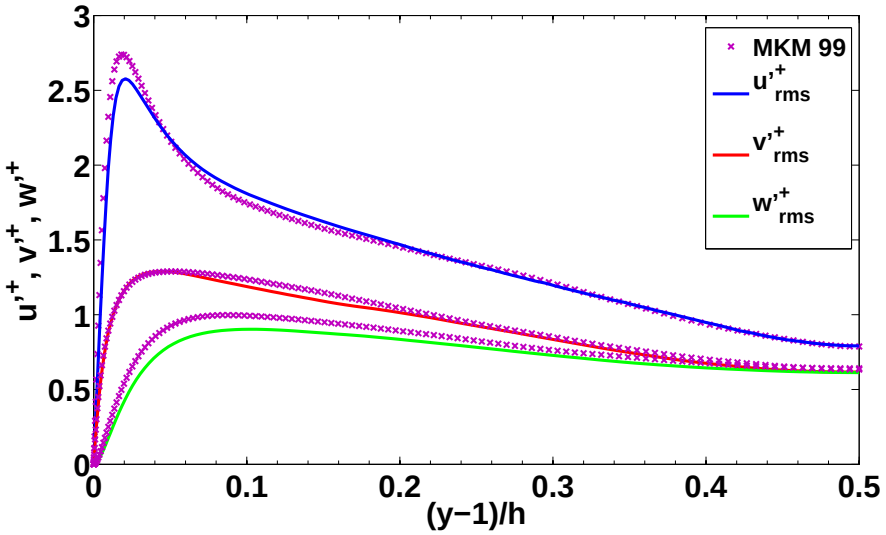

Figure 4.2: $u'_{rms}, v'_{rms}, w'_{rms}$ **profile** - time and spanwise averaged at $x = -2.0$.

a good qualitative agreement of all three profiles with the reference data, however some differences are noticeable, particularly in the peak of u'_{rms} and w'_{rms} profiles. Again, this difference might be attributed to the presence of the step in the bfs7 case, as it was discussed in the paragraph above. Also, the difference in Re_τ might be of significance, as even the simulations of turbulent channel flow with different Re_τ have slightly different turbulence intensity profiles (see Moser *et al.*, 1999 and Kim *et al.*, 1987).

Apart from the statistical properties of the flow in the inlet section, an important concern was the influence of the length of the inlet channel and the periodic (inlet regeneration) section on the dynamics of the flow. The power spectrum of figure 4.3 shows that the periodic regeneration area introduces an artificial frequency $St = 0.127$, and its harmonics, which corresponds to the periodic area length of $8h$. This could be avoided by increasing the periodic area length, however it would increase the computational cost of the simulation. Therefore the

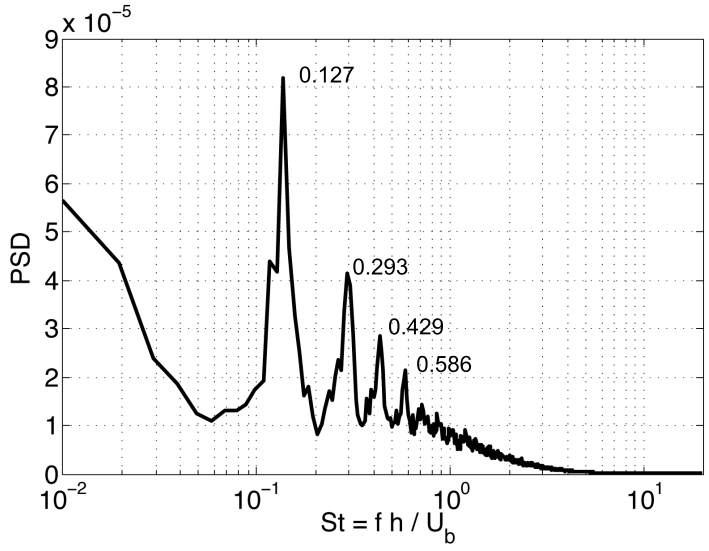

Figure 4.3: Power spectrum of u' - power spectral density of spanwise averaged u' velocity fluctuation at $x = -2.0, y = 1.5$.

periodic length was kept at $8h$, which roughly corresponds to the length of $7h$ used by Le (1995) to regenerate the turbulent properties of the flow after they break down at the inlet. In the case of Le (1995) the turbulent inlet was provided as a mean profile with fluctuations generated from a prescribed spectrum. A thorough examination of spectra at different locations in the flow, which shows that the recycling frequency does not have any significant influence on the dynamics of the flow, is presented in Section 4.4.2.

4.2.2 Reattachment length and coefficient of friction

The *reattachment length* (X_r) is the average distance from the step edge to the flow reattachment position. There are a number of methods for finding the reattachment position. The location of the mean dividing streamline $\psi = 0$ at the bottom wall is one possibility. In the pdf method the reattachment location is

indicated by a point where 50% of the flow is in the forward direction at the first grid-point away from the wall. The method used in this work consists of looking for zeros of the coefficient of friction (C_f) at the bottom wall. In the Le (1995) simulation, the difference between the mean dividing streamline method and the zero wall shear stress method was within 0.1%, while the pdf method gave results within 2% of two other methods. Figure 4.4 compares the coefficient of friction with the computational data of Le *et al.* (1997) and the experiments of Adams & Johnston (1988), Jovic & Driver (1995) and Spazzini *et al.* (2001). All the comparison data was obtained from cases without a top wall. Studies that investigated the cases with $ER = 2.0$ and a top wall either do not report C_f or deal with laminar or transitional flow.

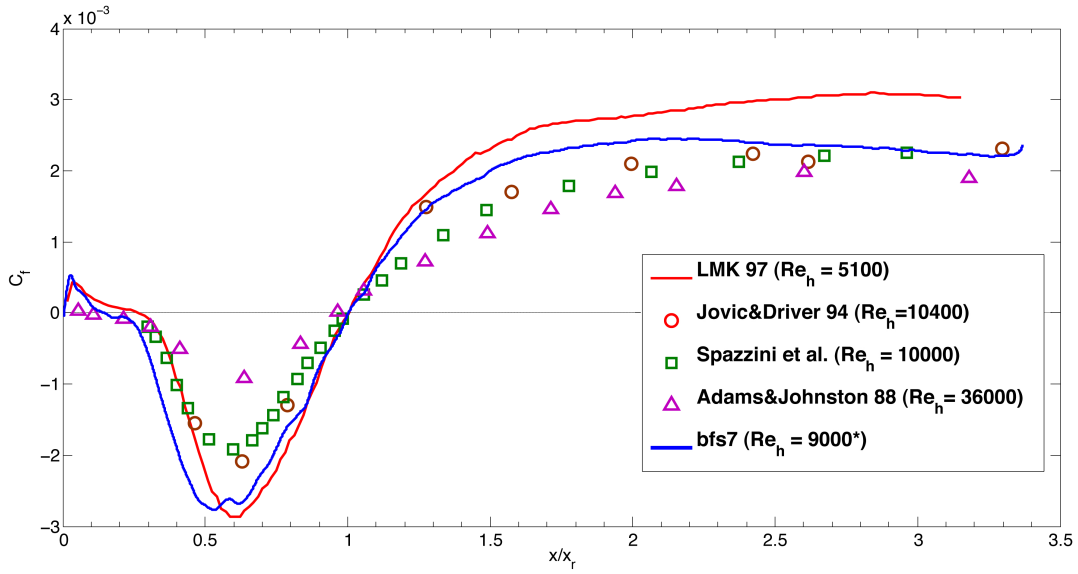

Figure 4.4: Coefficient of friction - comparison with experimental and DNS data.

One issue was the proper scaling of C_f, since in the current case the velocity scale is the mean bulk velocity at the inlet (U_b), while in the comparison cases it

is the maximum inlet velocity (U_0). Therefore for the C_f study the velocity scale was assumed to be the maximum mean inlet velocity $U_0 = 1.22U_b$.

The relatively close minimas of the coefficients of friction of the current case (bfs7) with the LMK97 result were a surprise. Owing to the roughly doubled Reynolds number one would have expected a decreased C_f minimum. Instead, the peak with minimal value is slightly shifted upstream. One reason for this might be that in fact we are comparing two different cases, and the presence of the top wall makes the difference. Another problem, mentioned in the previous paragraph, is the difference in the choice of the reference velocity, which follows from different geometrical set-ups. In the regeneration region, C_f follows the results of Jovic & Driver (1995) and Spazzini *et al.* (2001). The discrepancy between LMK97 and other results in the regeneration zone might be due to low Reynolds number effects, as this case has relatively low Re_h.

Table 4.2 shows X_r values for a number of computational and experimental studies, along with the peak negative C_f, its position downstream from the step, the expansion ratio ER and Reynolds number for each case. Cases bfs6 and bfs7 represent the simulations performed in the frame of this study. Since different authors use different scaling quantities, for all other results the Re column has (in brackets) Reynolds numbers scaled with bulk mean velocity and step height for better comparison.

The case of Armaly *et al.* (1983), which has the same expansion ratio as the present study, revealed that X_r depends strongly on Re in the laminar and transitional regime, however for turbulent flow there is no Reynolds number dependence. Figure 4.5 compares their results with two reattachment lengths com-

Case	Re_h	X_r	ER	$C_{f,min}$	$X_{(C_{f,min})}/X_r$
bfs7	9000	8.62	2.0	$-2.9 \cdot 10^{-3}$	0.62
bfs6	6000	8.16	2.0	$-3.12 \cdot 10^{-3}$	0.53
LMK 97	5100 (4250*)	6.28	1.2	$-2.89 \cdot 10^{-3}$	0.61
Armaly *et al.* 83	8000 (4000*)	8.0	2.0	-	-
Adams & Johnston 88	36000 (30000*)	6.3	1.25	$-0.885 \cdot 10^{-3}$	0.63
Jovic & Driver 94	10400 (8700*)	5.35	1.09	$-2.0 \cdot 10^{-3}$	0.63
Spazzini *et al.* 2001	10000 (8300*)	5.39	1.25	$-1.87 \cdot 10^{-3}$	0.6
Chandrsuda & Bradshaw 81	10^5	6.0	1.4	-	-

Table 4.2: Reattachment length and coefficient of friction

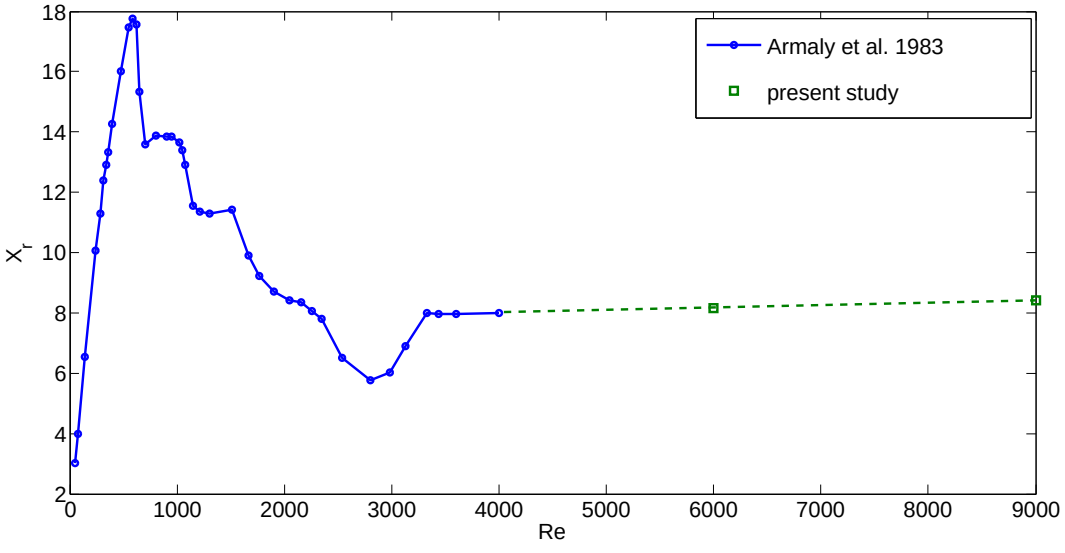

Figure 4.5: Reattachment length as a function of Re - present data (green) compared with Armaly *et al.* (1983) results (blue).

puted for different Reynolds number. Present results indicate that there might be a weak Re dependence of X_r in the turbulent regime, which would not have been apparent in the Armaly *et al.* (1983) study, as it only examined a few very low turbulent Re cases (up to $Re_h = 4000$, where $Re_h = 3300$ was identified as the lower limit of the turbulent regime). Similar conclusions come from the comparison of results of Spazzini *et al.* (2001) and Adams & Johnston (1988), where tripled Re causes $\approx 17\%$ increase in the reattachment length.

4.2.3 Grid resolution study

In order to verify the choice of grid resolution and Re_h, the two-stage resolution study was performed. The first stage consisted of comparing the spectral element mesh size with the Kolmogorov scale of the flow. In the second stage we looked at the modal energy decay in different points of the flow to confirm adequate grid resolution in the spanwise direction.

4.2.3.1 Kolmogorov scale analysis

Unlike in finite difference methods, defining the grid size in the spectral element method poses a challenge. Not only is the computational mesh designed on the elemental scale, but each element also has its internal mesh of nodal points. For the purpose of this study, we define the grid spacing A as a measure of the distance between nodal points: $\Delta_{ij}^{A} = (\Delta x_i \cdot \Delta y_j)^{\frac{1}{2}}$, where Δx_i and Δy_j are the distances between neighbouring nodal points within an element in the streamwise and vertical direction. That means that the areas near the element edges have very small grid spacing, while the element interior always has a coarser

mesh. This does not reflect the true accuracy of the SEM, as the Gauss-Lobatto-Legendre spacing of the nodal points within an element is superior to a uniform distribution (see Section 2.4.3). Therefore another representation of the grid spacing is needed. Let the grid spacing B be a spacing where within each element the nodal points are assumed to be uniformly distributed. In other words, let each element have only one value of grid spacing defined within its boundaries. This spacing is defined as the size of the element divided by the number of points: $\Delta^B_{ij} = \Delta^B_e = (\Delta x_e \cdot \Delta y_e)^{\frac{1}{2}}/N_P$, where Δx_e and Δy_e are the streamwise and vertical sizes of the element for which the spacing is defined. Note that we define the spacing Δ^B_{ij} in all the internal points of the element e, even though the value is identical in all those points within the same element. This will represent the quality of the elemental mesh better, without the interference of the local distribution of nodes within each element.

Figure 4.6 presents the results of this analysis. On each graph the grid spacing calculated using the different approach was divided by the Kolmogorov scale estimated by

$$\eta_K = \left(\frac{\nu^3}{\epsilon}\right)^{\frac{1}{4}}, \tag{4.1}$$

where $\epsilon = 2\nu S_{ij} S_{ij}$ is the energy dissipation rate and S_{ij} represents the rate-of-strain tensor. For simplicity, let $r_r = \Delta/\eta_K$ be called the resolution ratio, where Δ stands for the grid spacing A or B. Figures 4.6 (a) and (b) present the results calculated using grid spacing A and B respectively for an instantaneous flow field. The spacing A clearly gives higher peak values of the resolution ratio. This is expected, as the grid spacing at the centre of each element is much coarser than on the element edges. Very high ratios ($r_r > 8$) are very rare. The shear layer

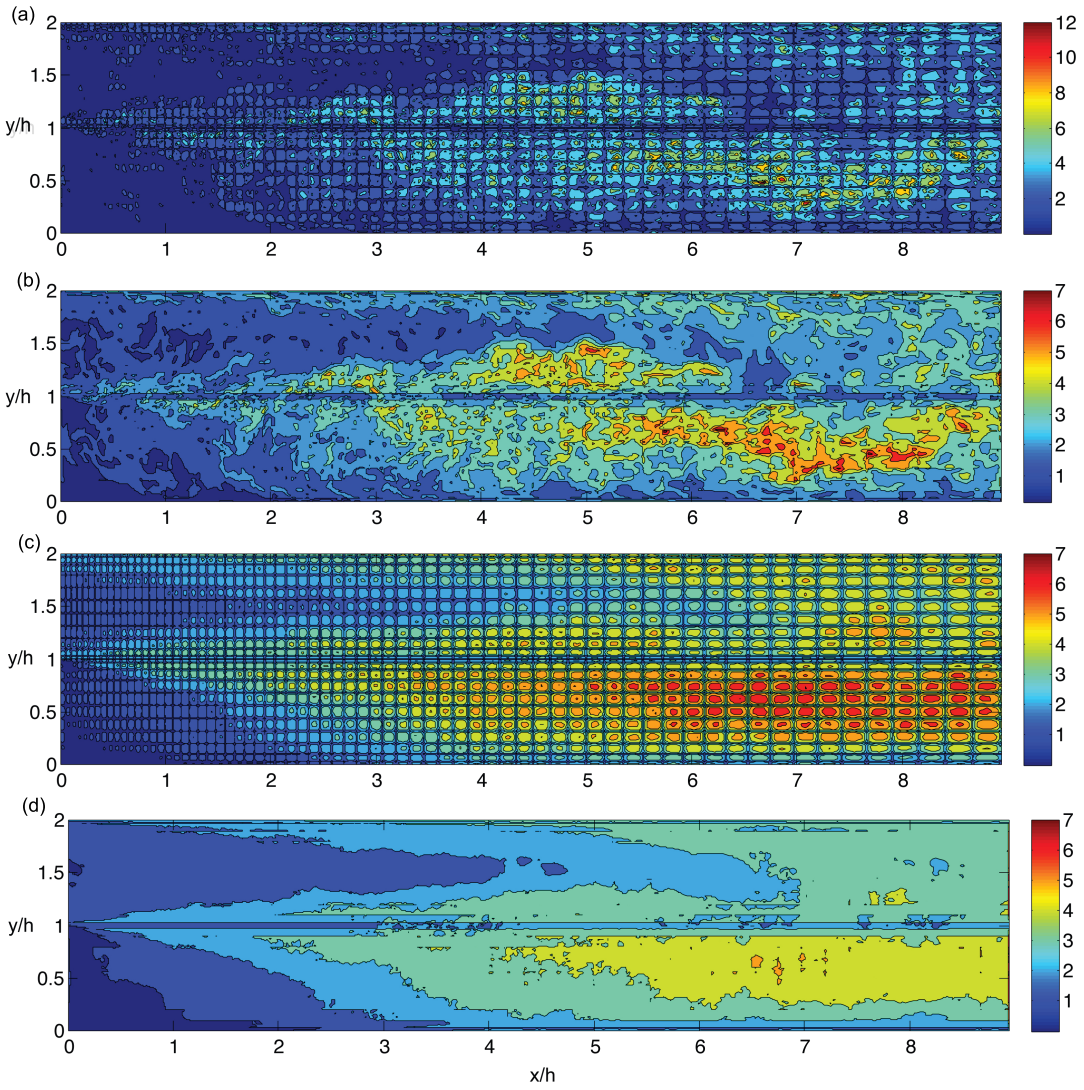

Figure 4.6: Grid spacing divided by the Kolmogorov scale - grid spacing divided by η_K; (a) Instantaneous result for grid spacing A; (b) Instantaneous result for grid spacing B; (c) Spanwise averaged result for grid spacing A; (d) Spanwise averaged result for grid spacing B. Grid spacing B (assumed uniform distribution of points within an element) provides a better result. Ratio of grid spacing to η_K does not exceed 7 in the worst case, and is below 5 in the most active regions (reattachment zone and mixing layer).

near the centre of the channel is very well resolved ($r_r < 2$). The resolution in the reattachment region is at moderate level $r_r \approx 4 - 6$. The clear element boundary outlines that are visible in the figure are the expected result of the grid spacing definition, as Δ^A near the elemental boundaries is much smaller than in the element interior.

When the grid spacing B is used, the elemental boundaries are not as visible (figure 4.6 b). The peak values of r_r are much smaller. The maximum value of resolution ratio is $r_r \approx 7$ and a vast majority of the most active regions (reattachment zone) has $r_r < 5$.

Figures 4.6 (c) and (d) present the spanwise averages of the results shown in figures 4.6 (a) and (b) respectively. In both cases the peak r_r does not exceed 7. The spacing B shows that most of the domain has $r_r < 5$. The wall regions are very well resolved with the resolution ratio below 3. This analysis shows that $\Delta = O(\eta_K)$, which confirms that the grid refinement in the x-y planes is sufficient for $Re_h = 9000$.

4.2.3.2 Modal energy decay

In order to verify the resolution in the spanwise direction, the modal energy decay in several places in the flow was examined. Figure 4.7 (a) shows the result obtained in the inlet channel. 4.7 (b), (c) and 4.8 (a) present the results for different places in the shear layer. All those cases exhibit a clear drop of the modal energy over at least two decades. This indicates the adequacy of the spanwise resolution in the shear layer. Figures 4.7 (d) and 4.8 (b) contain the spectra calculated near the wall in the recirculation and reattachment region

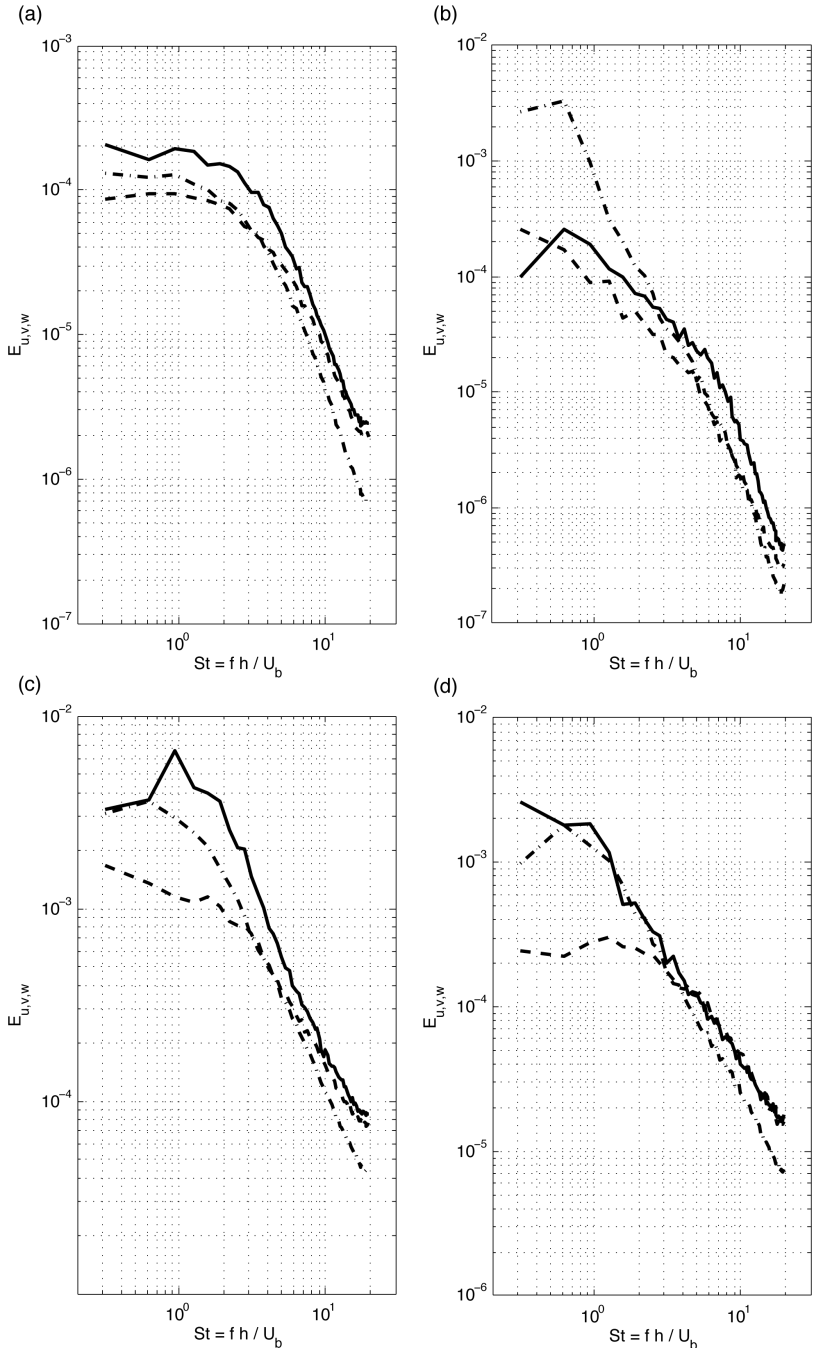

Figure 4.7: Modal energy decay - spectrum of u' (solid line), v' (dashed line) and w' (dot-dashed line) energy at (a) $x = -2h$, $y = 1.5h$, (b) $x = 0.1h$, $y = 1h$, (c) $x = 4h$, $y = 1.0h$, (d) $x = 4h$, $y = 0.1h$. Spectra averaged over time.

respectively. While the drop of E_{uu} and E_{ww} is sufficient, E_{vv} in the reattachment region might suggests that higher spanwise resolution near the wall is needed in order to resolve the small-scale structures.

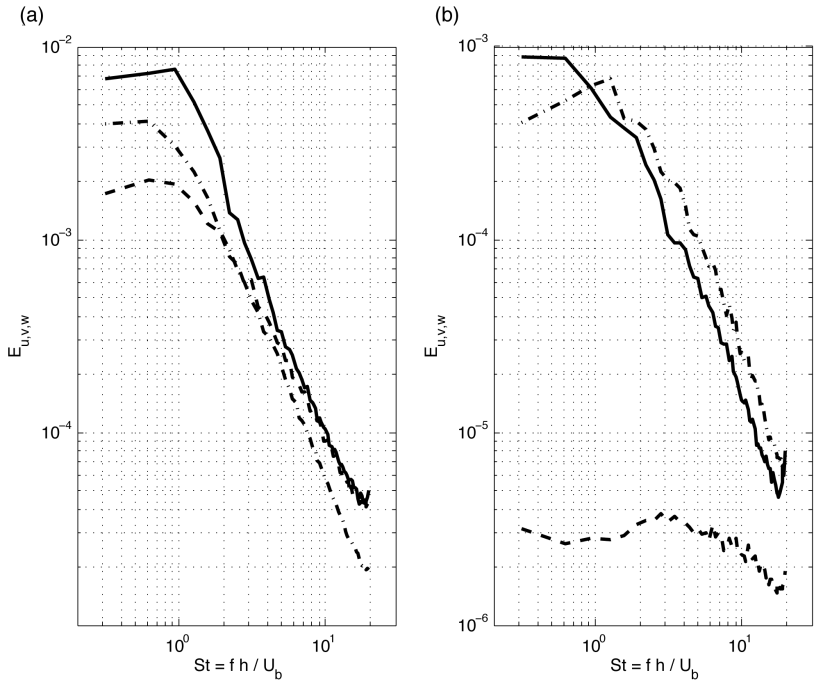

Figure 4.8: Modal energy decay - spectrum of u' (solid line), v' (dashed line) and w' (dot-dashed line) energy at (a) $x = 8h$, $y = 1h$, (b) $x = 8h$, $y = 0.01h$. Spectra averaged over time.

4.3 Averaged Flow Field

This section contains statistical data collected over the total averaging time $T_{ave} = 200h/U_b$. The total number of samples was 8000. The averaging was initiated after initial burn-in time of $T_{BI} = 50h/U_b$, which allowed for passing of the initial transients that followed from the change of Re_h from 6000 in the preliminary simulation to 9000. T_{BI} is equal to roughly two flow-through times. The flow-

through time is defined as the integral of $\frac{1}{U}$ along the streamline S calculated on an averaged velocity field, originating at $x = 0.0$, $y = 1.5$ and finishing at the plane $x = 20.0$.

$$T_{FT} = \int_S \frac{\mathrm{d}S}{U}.$$

The initial condition for the burn-in process was taken from preliminary simulations with $Re = 6000$ and $N_P = 11$. The length of the burn-in process selected was based on the streamwise component of viscous force on walls

$$F_{\tau x} = \int_W \tau_{xj} n_j \mathrm{d}W,$$

where W is the surface on which no-slip condition is defined (top and bottom wall of the channel) and $j = x, y, z$. Spanwise and vertical components are negligible compared to the streamwise.

Figure 4.9 shows that the initial transient behaviour is confined roughly in the first $30h/U_b$ time units of the simulation. Two flow-through times were allowed before the averaging was initiated, in order to be certain that no transient behaviour, that might not show in $F_{\tau x}$, is present in the domain. The statistics of pressure, velocity and Reynolds stress tensor components were collected.

In order to check the statistical convergence of the simulation, the history of time averaged reattachment length was plotted in figure 4.10. The X_r remains within 0.1% of the final value for the last flow-through time and is bounded by $\pm 0.4\%$ limit in the last four flow-through times. This gives a reasonable level of confidence in the convergence of the collected statistics.

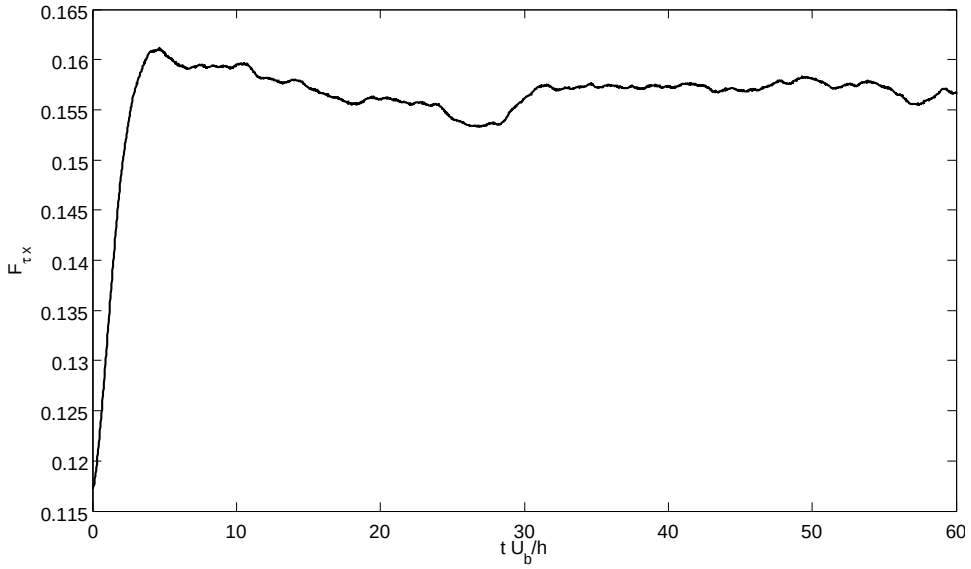

Figure 4.9: Streamwise viscous force on walls - integral over wall surfaces of viscous stresses in the streamwise direction.

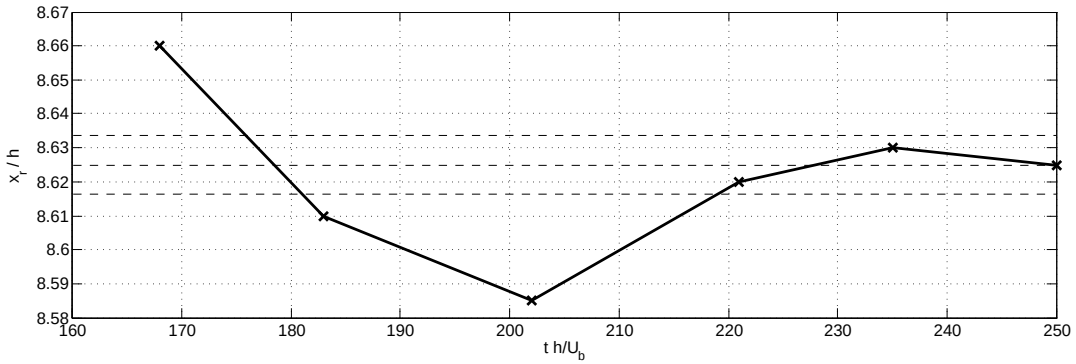

Figure 4.10: Averaged reattachment length history - time and spanwise averaged X_r at different simulation times. Dashed line shows $\pm 0.1\%$ of the final X_r.

4.3.1 Pressure field

Time and spanwise averaged contours of the pressure coefficient are shown in Fig. 4.11. The pressure coefficient is defined as

$$C_P = \frac{P - P_0}{\frac{1}{2}\rho U_b^2},$$

where P_0 is a reference pressure taken at $x = -4h$, $y = 1.5h$. There is a clear pressure drop zone originating at the step edge and spanning up to approximately $x = 4.2h \approx \frac{1}{2}X_r$.

Figure 4.12 shows the static pressure variations across the channel in 8 different locations in the outflow channel. The reference pressure P_w is taken locally at the top wall. The figure pictures the pressure deficit in the recirculation zone, mainly in the mixing layer. There is a significant difference in static pressure at the top and bottom wall throughout the outflow channel. In the recirculation zone the difference is in favour of the top wall, while in the reattachment zone the static pressure at the bottom wall is higher. Far downstream in the regeneration zone the static pressure profile returns slowly towards a uniform distribution across the channel. Figure 4.13 compares the distribution of static pressure coefficient at the top and bottom wall. The deficit of pressure at the bottom wall in the recirculation area is clearly visible. The situation is opposite in the zone between $x \approx 7$ and $x \approx 15$, where the presence of the reattachment increases the pressure on the bottom wall. Further downstream the flow regenerates and both curves collapse.

Figure 4.14 shows maximum C_P as a function of the expansion ratio ER.

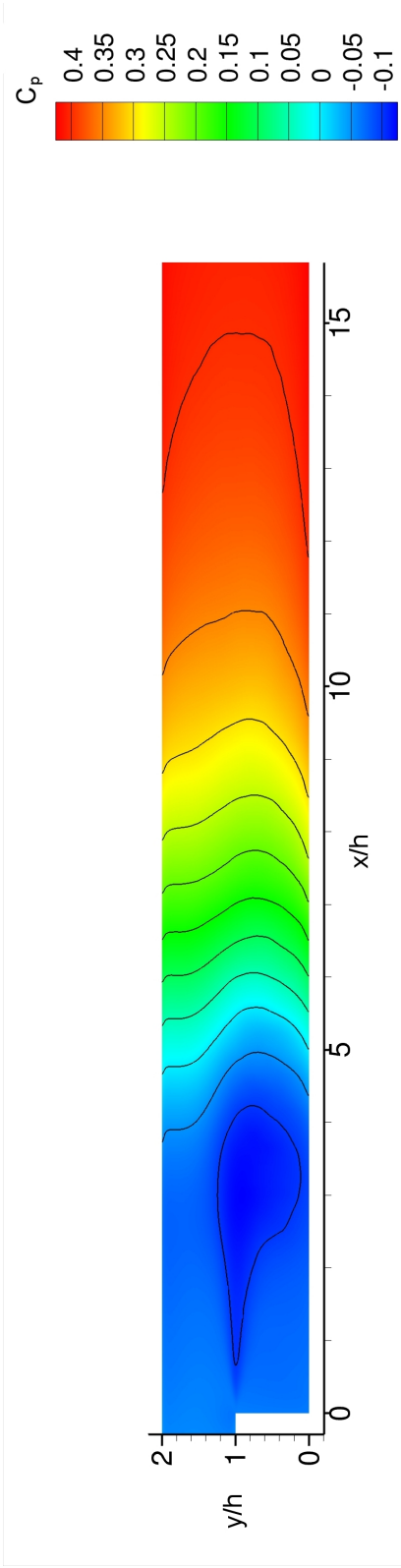

Figure 4.11: Mean static pressure coefficient contours - pressure coefficient given by $C_P = \frac{P-P_0}{\frac{1}{2}\rho U_b^2}$.

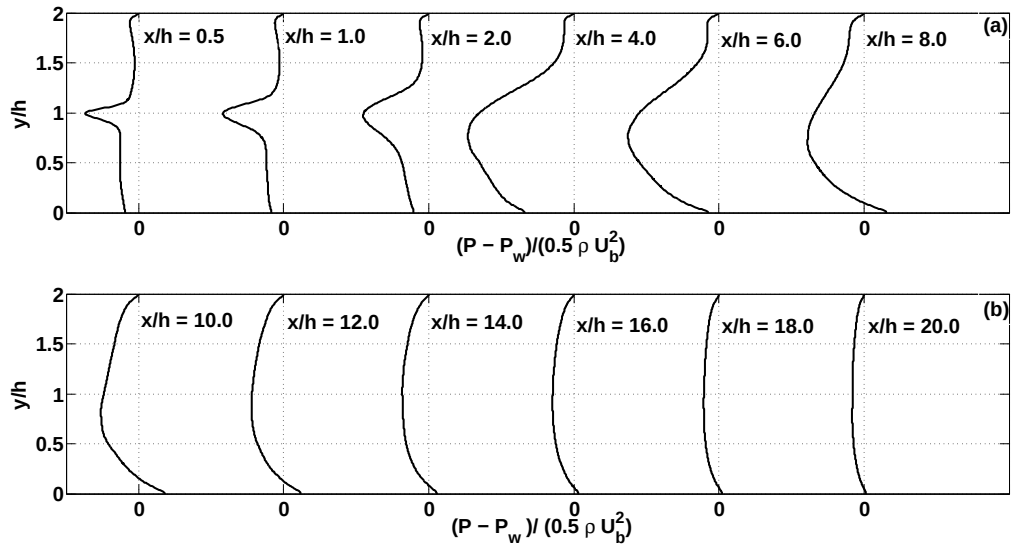

Figure 4.12: Static pressure variation across the channel - (a) recirculation region; (b) Reattachment and recovery region.

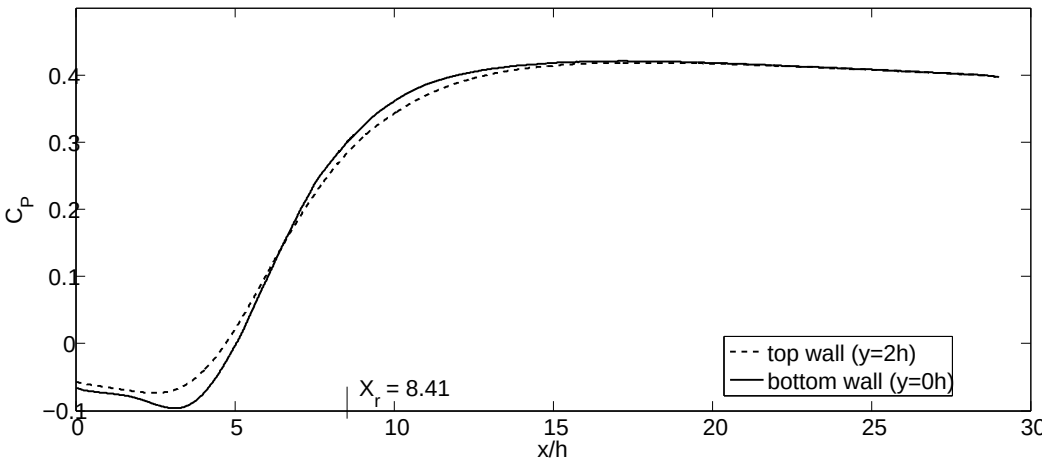

Figure 4.13: Static pressure coefficient distribution - dashed line - top wall; solid line - bottom wall.

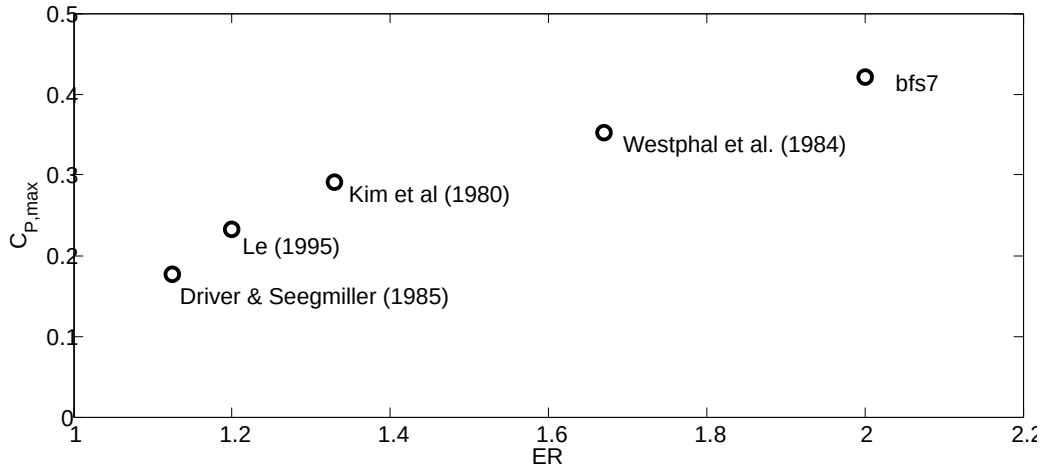

Figure 4.14: Maximum of the static pressure coefficient in different experiments and simulations - $C_{P,max}$ against expansion ratio.

The results were obtained from the present case (bfs7), as well as the previous investigations of Le (1995), Driver & Seegmiller (1985), Kim *et al.* (1980) and Westphal *et al.* (1984) (the last data set obtained from Le, 1995). It is clear from the experimental data that the static pressure maximum grows with the ER. The bfs7 results continue this trend. To the author's knowledge there is no simulations and experiments with $ER > 2$.

In order to investigate the wall pressure distribution further, the figure 4.15 presents the bottom wall static pressure coefficient compared with the DNS of Le (1995) as well as experiments quoted in the previous paragraph. To collapse the results better, the streamwise coordinate was scaled by the reattachment position:

$$x^* = \frac{x - X_r}{X_r}.$$

The results diverge significantly in the regeneration zone. As shown in figure

4.14, this is caused by a wide spectrum of expansion ratios in the reference data. There is also a clear difference between the present case and reference data in the recirculation area, which is caused by a different reference pressure. In order to

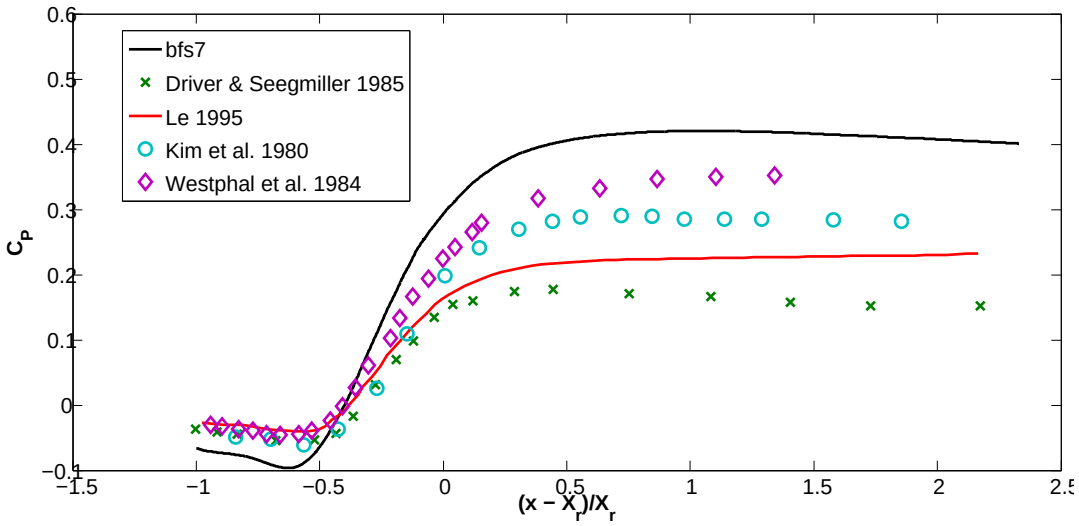

Figure 4.15: Pressure coefficient at the bottom wall - comparison with results of Driver & Seegmiller (1985), Kim *et al.* (1980) and Le (1995) (results of Westphal *et al.*, 1984 cited after Le, 1995).

collapse the pressure data several authors proposed different scaling. Roshko & Lau (1965) proposed to use the minimum pressure coefficient

$$\tilde{C_P} = \frac{C_P - C_{P,min}}{1 - C_{P,min}}.$$

Kim *et al.* (1980) extended this idea by introducing an additional parameter based on the ER only:

$$C_P^* = \frac{C_P - C_{P,min}}{C_{P,BC} - C_{P,min}},$$

where $C_{P,BC}$ is the Borda-Carnot pressure coefficient:

$$C_{P,BC} = \frac{2}{ER}\left(1 - \frac{1}{ER}\right).$$

Figure 4.16 shows the two scaling techniques applied to the present simulation data as well as the reference data sets. With the first scaling of Roshko & Lau (1965), the choice of the reference pressure is not longer a problem, as all the profiles collapse well in the recirculation region. Large discrepancies still occured in the reattachment and regeneration zones. The second scaling managed to collapse the data in both recirculation and regeneration regions. In particular, the present result and the Le (1995) data collapse well, regardless of the difference in the ER. The experimental data sets still maintain the ER dependence in the reattachment region.

4.3.2 Streamwise velocity field

The mean streamwise velocity colour-map and streamlines are presented in figure 4.17. Subplot (a) shows the flow domain without the inlet and far downstream sections, while subplot (b) presents the close-up of the recirculation zone. The incoming flow is expanding slowly towards the bottom wall, reattaches to it around $x = 8.41h$ and regenerates downstream towards a fully developed channel flow. The interaction of the incoming flow and the fluid trapped by it in the corner after the step causes the recirculation bubble to form. The recirculation bubble turnover time ($T_{BT} \approx 400h/U_b$ integrated along streamlines of the averaged velocity field) is much larger than the flow-through time of the main

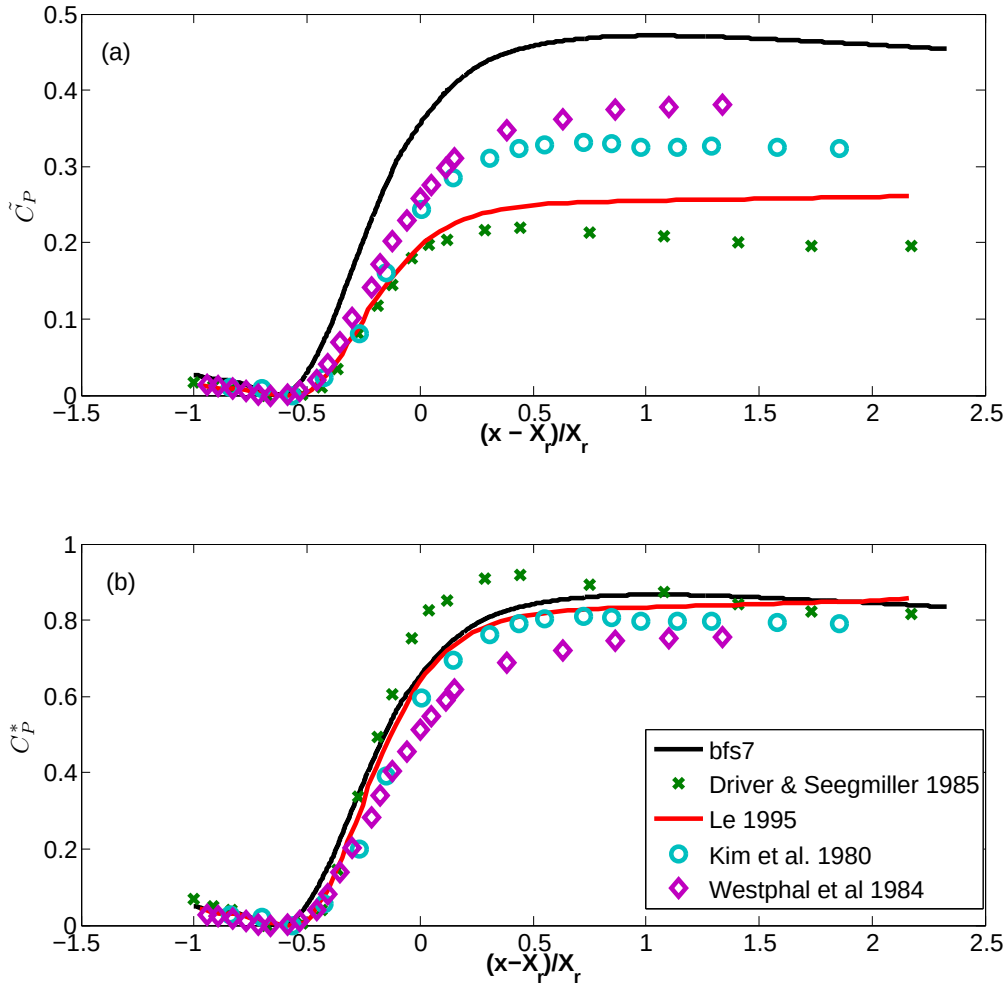

Figure 4.16: Pressure coefficient at the bottom wall - (a) scaling of Roshko & Lau (1965); (b) scaling of Kim *et al.* (1980).

flow ($T_{FT} \approx 25h/U_b$). The maximum reverse flow region in the recirculation zone occurs between $x = 2.0h$ and $x = 6.0h$ with $U_{min} = -0.25$ at $x = 3.91$, $y = 0.08$. There is no evidence of the recirculation bubble at the top wall, which is in agreement with previous findings.

Figure 4.17 (b) shows that apart from the primary recirculation bubble there is another, secondary eddy in the step corner. Closer examination reveals the tertiary eddy (close-up in figure 4.19 a). This resembles the prediction by Moffat (1964) made for the low Reynolds number flow in the vicinity of the sharp corner. The theory predicted an infinite number of eddies decreasing in size and strength in the limit of $Re \to 0$. Computations by Biswas *et al.* (2004) showed two corner eddies for $Re = 1$. Experiments by Hall *et al.* (2003) investigated the secondary vortex in the turbulent backward-facing step flow, however did not reveal any tertiary eddies. Le *et al.* (1997) report the presence of secondary and tertiary corner eddies: the secondary eddy extends to $1.76h$ in x direction and $0.8h$ in y, while tertiary eddy is $0.042h$ in size.

The secondary eddy shown in figure 4.18 exhibits the following structure: streamlines show that there is an additional secondary eddy present right at the tip of the main secondary eddy (see figure 4.18 b). This additional vortex has the same anti-clockwise direction as the main secondary eddy. To differentiate between two structures, the main secondary eddy will be called the secondary corner eddy, and the additional structure will be refered to as the additional secondary eddy. The total streamwise dimension of the entire secondary structure is equal to $1.44h$ (based on the $U = 0$ isoline). It is difficult to judge any clear separation point between the two structures - some insight might be provided by

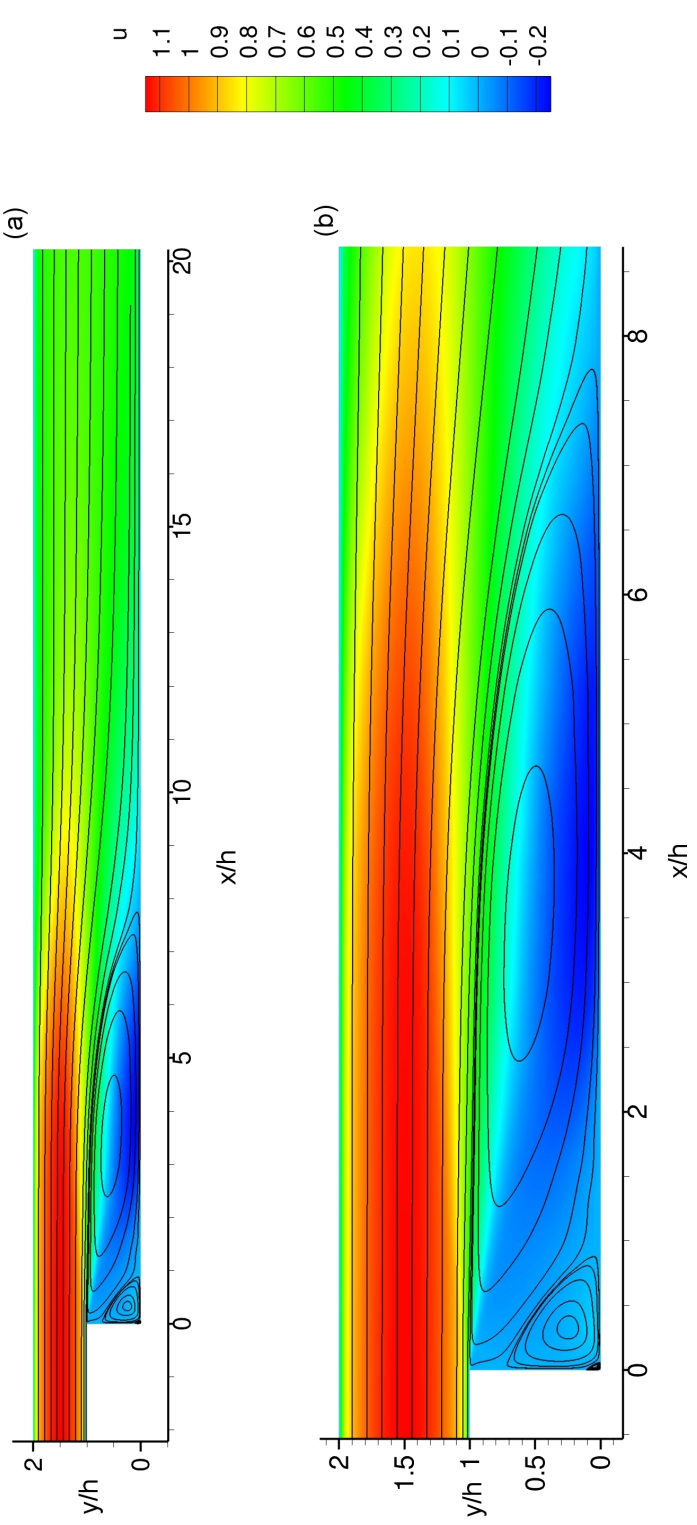

Figure 4.17: U **velocity field and streamlines** - (a) recirculation, reattachment and regeneration zones; (b) recirculation zone.

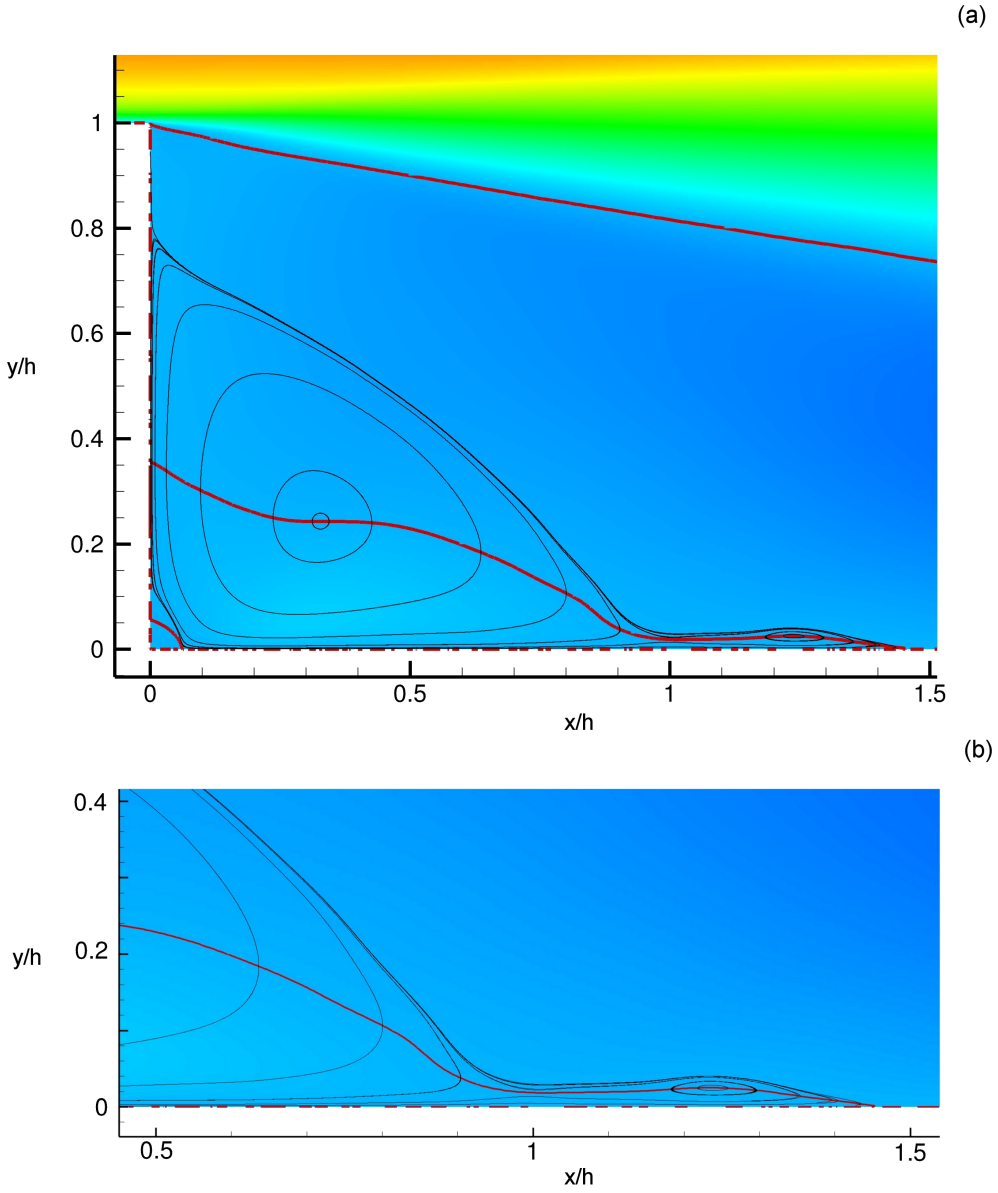

Figure 4.18: Secondary recirculation bubble - U velocity colour-map and streamlines. Red solid line marks $U = 0$.

the position of the $V = 0$ isoline attachment to the bottom wall ($x = 0.99h$). The vertical span of the secondary corner eddy is $0.8h$, which is in excellent agreement with Le *et al.* (1997). The centre of the secondary corner structure is located at $x = 0.328h$, $y = 0.243h$, and the additional structure is centred at $x = 1.237h$, $y = 0.025h$. The tertiary corner eddy size is $0.062h$ in horizontal and $0.11h$ in vertical dimension. Its centre is located at $x = 0.03h$, $y = 0.042h$.

Both the additional secondary and the tertiary corner eddies are small structures. Figure 4.19 shows the spectral element mesh overlapping both structures. The additional secondary structure is covered by roughly 5 elements in the streamwise direction and over 1 element in the vertical direction, while the tertiary eddy is covered by over 1 element in the horizontal and 2 elements the vertical direction. One needs to keep in mind that a variable in each element is expanded using 11×11 nodal points, which gives the resolution of roughly 55×11 for the additional secondary structure and 11×22 for the tertiary corner eddy. This shows that both structures are well resolved. Given the mesh resolution, absence of further corner eddies is evident.

Consistent with these findings are PIV measurements by Hall *et al.* (2003), which indicate that an additional secondary structure might be present in the BFS flow. Their results, shown in figure 4.20, show that at the tip of the secondary eddy a part of the primary recirculating flow turns just ahead of the secondary vortex and flows in the direction perpendicular to the cross-sectional plane. The authors argue that it is unlikely to be a result of PIV error and concluded, that this might indeed be a new flow structure. This structure coincides in space with the additional secondary vortex revealed by the present study.

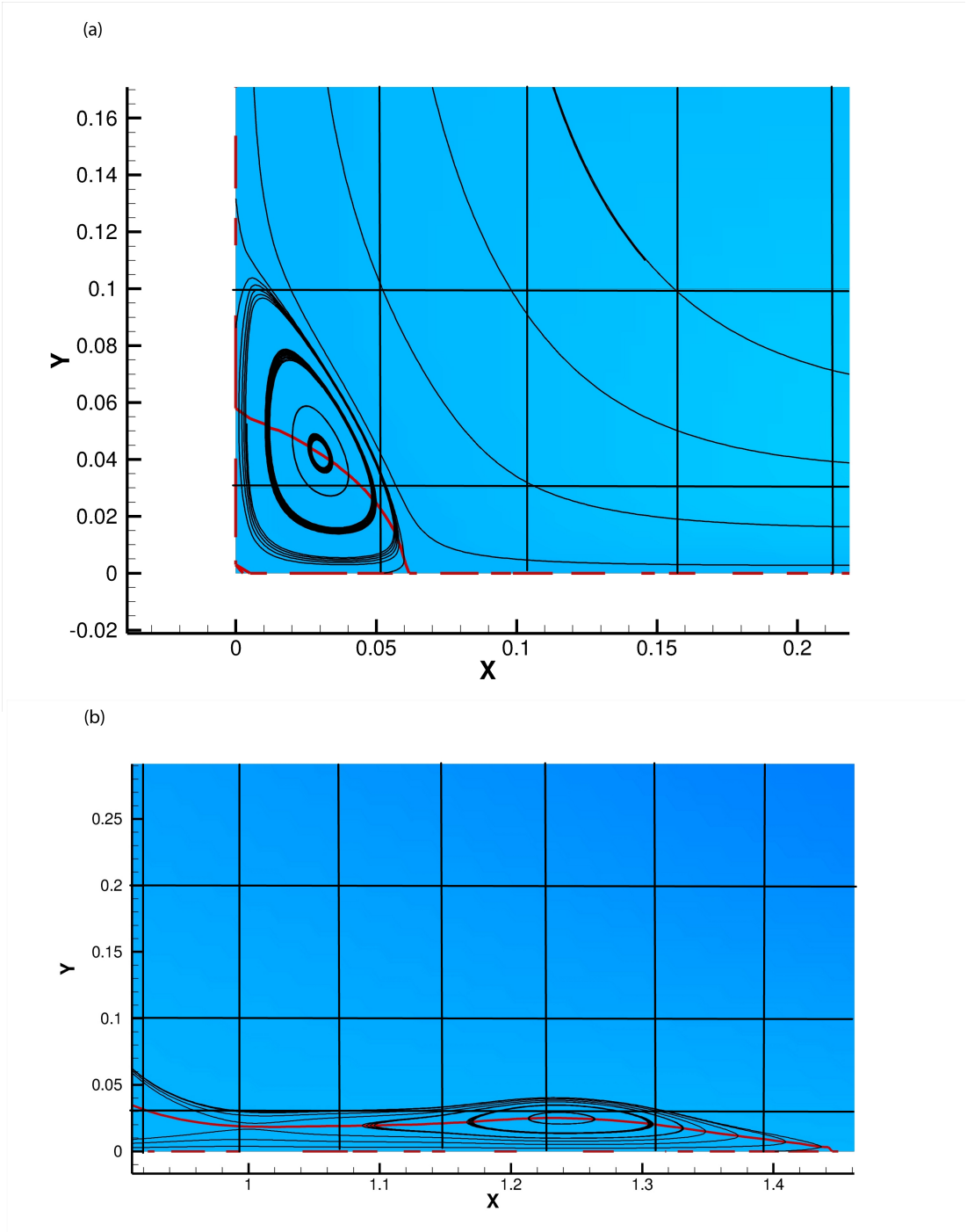

Figure 4.19: Mesh resolution of additional secondary and tertiary eddies - U velocity colormap and streamlines. Red solid line marks $U = 0$.

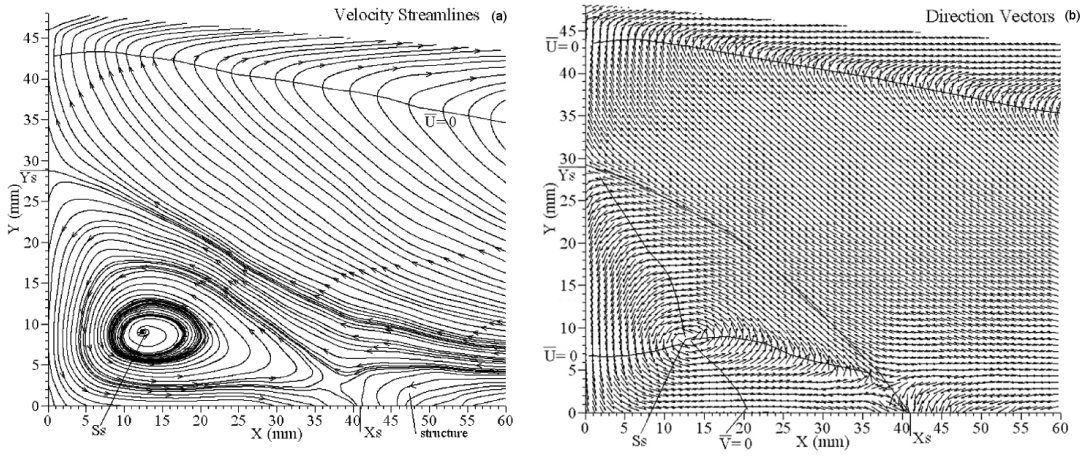

Figure 4.20: Additional secondary structure in the recirculation zone by Hall *et al.* (2003) - source: Hall *et al.* (2003).

It is worthwhile to examine the differences between structures in Fig. 4.18 and 4.20. The experimental study by Hall *et al.* (2003) revealed a spiral shape of the streamlines in the secondary vortex, which indicates a mass flow into the core that produces a spanwise flow in the secondary vortex. The presence of walls in the experimental setup might cause the secondary vortex to generate the Ekman pumping effect, which would explain the spanwise flow. Additionally, the flow in the spanwise direction in the additional secondary structure could be a part of the Ekman pumping effect balancing the flow within the secondary corner eddy. This does not exist in the present study. Streamlines are closed loops or spiral very slowly. Current results show that the additional secondary structure takes the form of another counterclockwise vortex forming at the tip of the secondary corner eddy. Despite differences in streamlines shape, which might be caused by the different spanwise boundary conditions, the fact that both structures occur at the same place indicates that the tip of the secondary vortex may indeed hold a new structure in the backward-facing step flow, as suggested by Hall *et al.* (2003).

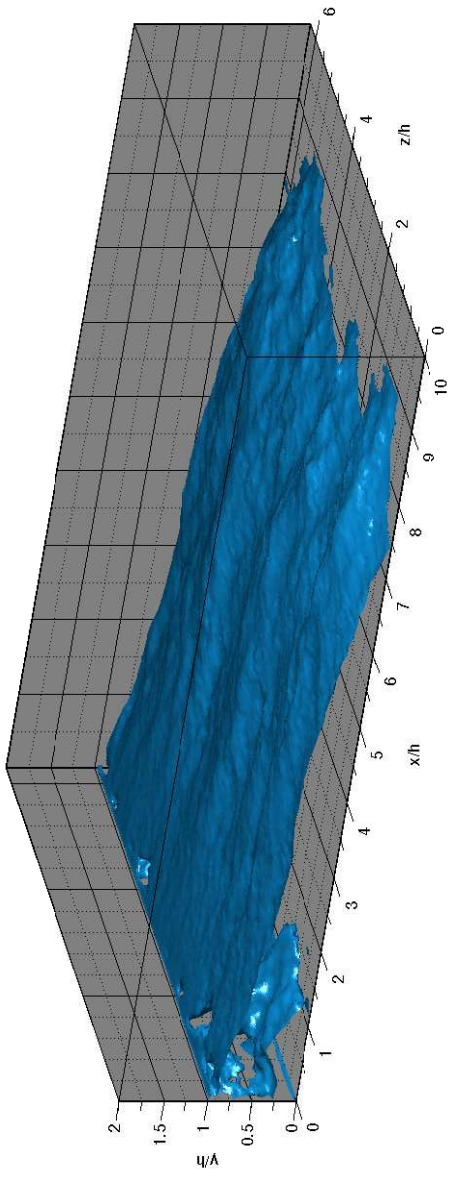

Figure 4.21: $U = 0$ **isosurface representing the primary recirculation eddy** - time averaged only.

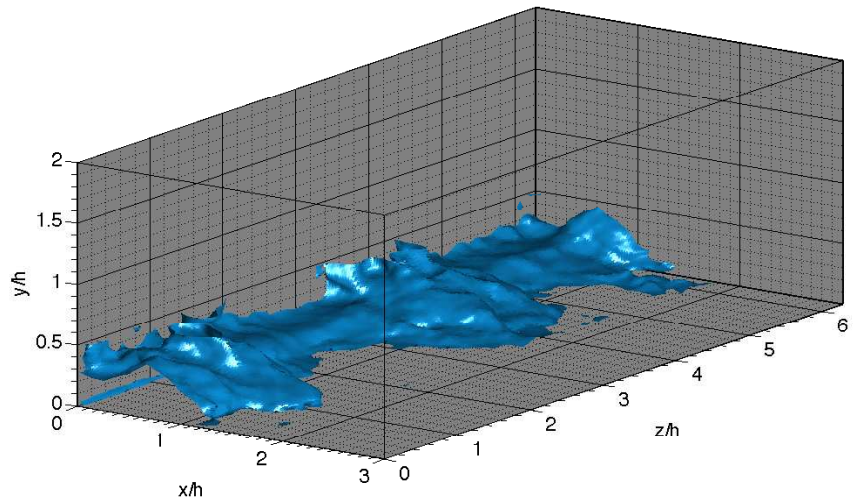

Figure 4.22: $U = 0$ **isosurfaces representing the secondary and tertiary recirculation eddies** - time averaged only. Tertiary eddy can be seen in the very corner ($x = 0$, $y = 0$).

Figure 4.21 presents the U isosurface averaged over time. The reattachment line is not a straight line in spanwise direction, as might be expected in a long time averaged flow, but exhibits a periodic wavy structure. This might be an effect of too short averaging time, however the convergence analysis in figure 4.10 shows that eight flow-through times are enough to obtain statistics converged within 0.1%. Also, the spanwise confinement might be the cause of such structure. This problem is addressed in Section 4.3.5. A similar wavy behaviour can be observed on the isosurface itself. There appear to be 3 to 4 lobes of the isosurface in $L_z = 2\pi$ span of the domain. This might be an evidence for persistent streamwise vortices present in the flow (see Section 4.3.5).

The isosurface in the figure 4.22 (which is a close-up of figure 4.21) that corresponds to the secondary eddy, exhibits similar wavy structure with 4 main lobes. Clearly the behaviour of the main recirculation bubble is influencing the

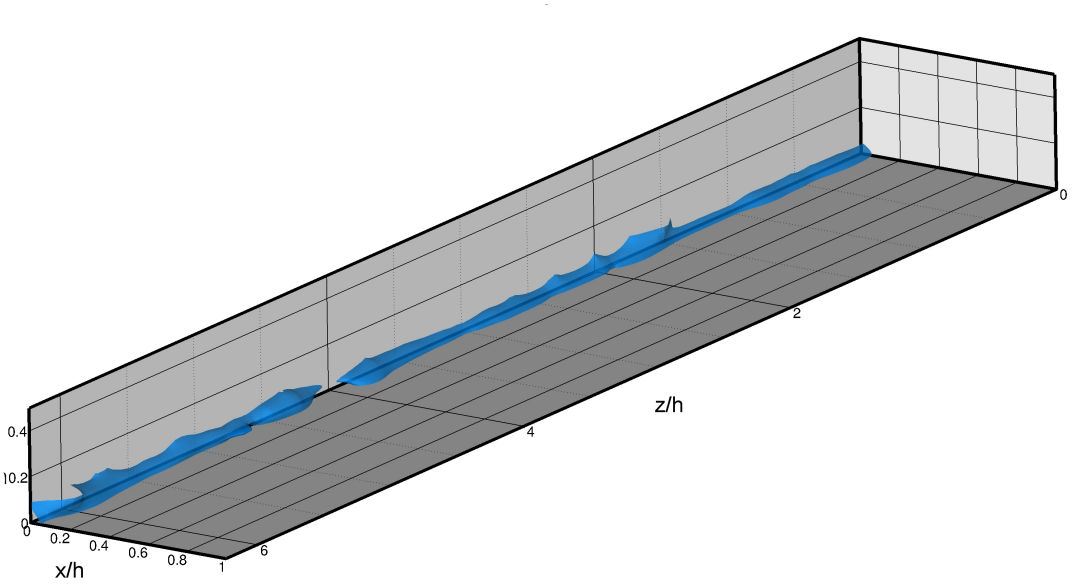

Figure 4.23: $U = 0$ **isosurface representing the tertiary recirculation eddy** - time averaged only.

secondary eddy. Moreover, the new structure identified in figure 4.18 does not span the entire domain. It rather represents the average effect of the secondary eddy lobes extruded into the main recirculation vortex. The tertiary corner vortex (figure 4.23) spans the entire width of the channel and does not show any waves in its structure.

4.3.3 Flow recovery

Figure 4.24 shows U profiles at different x locations. Initially fully developed turbulent flow expands freely in the expanded channel. Figure 4.24 (a) shows profiles in the recirculation zone and in the main flow prior to reattachment. The reversed flow is clearly visible. The maximum negative U position moves upwards as one gets further upstream from the reattachment position. The backward flow

is not visible at $x = 8.0h$ profile, even though the wall shear stress plot (figure 4.4) and Table 4.2 indicates the mean reattachment position at $X_r = 8.62$.

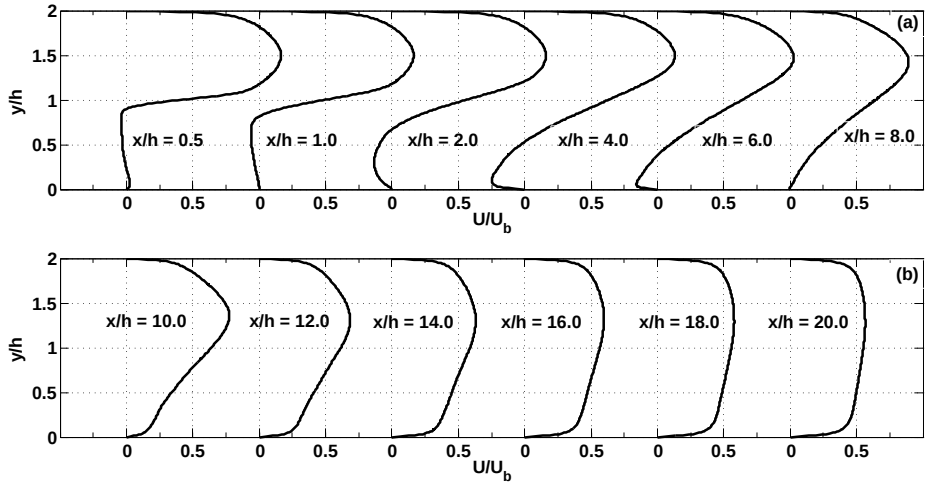

Figure 4.24: U **velocity profiles** - (a) recirculation region; (b) reattachment and recovery region.

Figure 4.24 (b) shows the development of the U profile downstream of reattachment. Initially the bottom part of the profile is clearly at a deficit compared to the top part, however the profile slowly recovers towards equilibrium as it goes downstream. Figure 4.25 presents streamwise velocity profiles in wall units (velocity normalised by a local friction velocity). It is clear that even very far downstream the fully developed profile has not been reached. The profile recovered well close to the wall (up to $y^+ \approx 40$) but the central part is still at a deficit compared to the profile upstream of the step. This result is in agreement with findings of Le *et al.* (1997). The authors referenced in Le (1995, p. 118) also report that even at long distances downstream ($50h$ - Bradshaw & Wong, 1972)

the velocity profile is still not fully recovered. Note that even though the reference profile taken at $x = -2.0$ has a different slope than a fully developed channel flow profile (as discussed in Section 4.2.1 and shown in figure 4.1), velocity profiles downstream of the step regenerate towards the correct slope, which suggests that indeed it is the presence of the step that deforms the inlet velocity profiles.

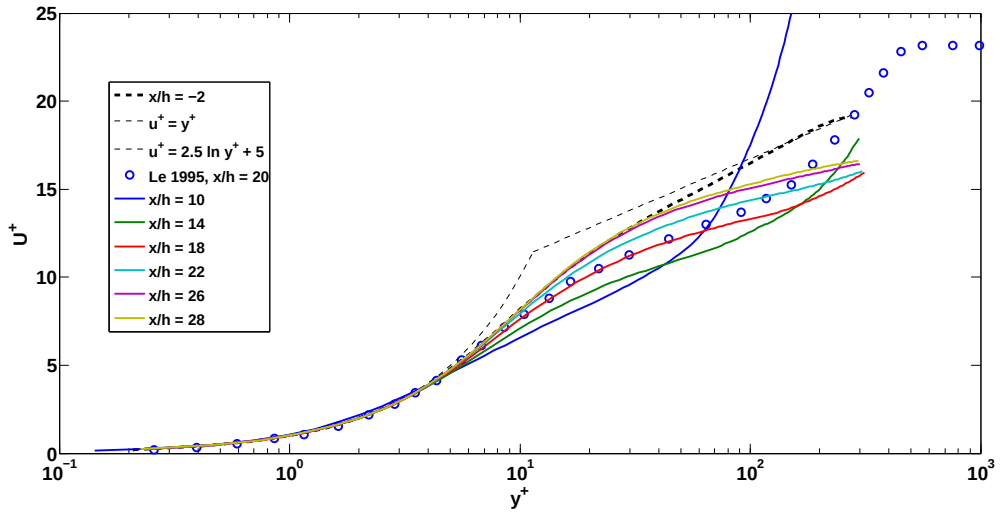

Figure 4.25: Recovery of the U velocity profile - comparison with the profile at $x = -2.0$.

4.3.4 Vertical velocity field

The profiles and contours of V velocity are presented in figure 4.26 and figure 4.27 respectively. There is a clear downward movement in the main flow area, with strong V gradient in the mixing layer shortly downstream of the step. The downward tendency, although minimal, is still present as far as $x = 20h$ downstream of the step. The recirculation zone close to the step edge exhibits strong upward

motion. The maximum value of the average vertical velocity $V_{max} = 0.045U_b$ is located at $x = 1.83h$, $y = 0.61h$. The strongest downwards motion $V_{min} = -0.06U_b$ occurs at $x = 6.58h$, $y = 1.01h$.

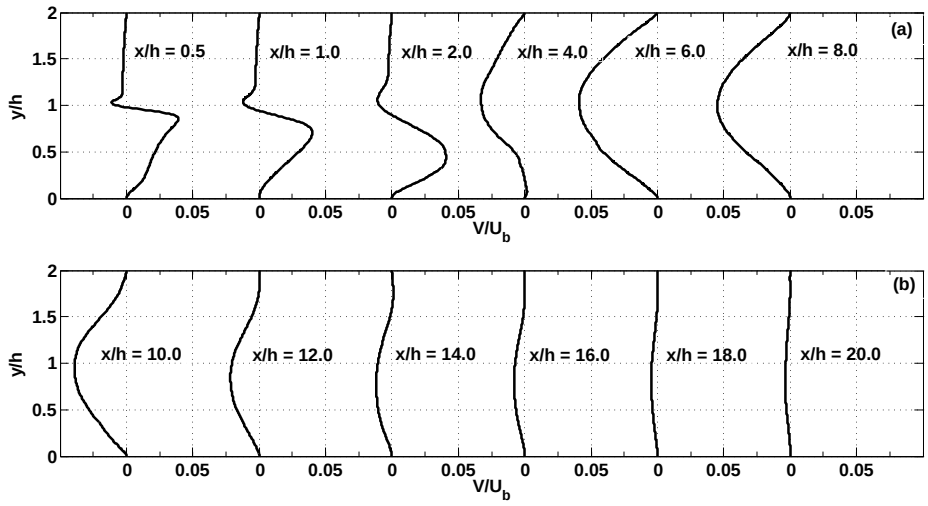

Figure 4.26: V **velocity profiles** - (a) recirculation region; (b) reattachment and recovery region.

Figure 4.28 shows cross-flow slices of V contours that have been time-averaged only. On top of the contours there is an outline of the $U = 0$ isosurface. The four lobes discussed in section 4.3.2 and depicted in figure 4.21 are clearly visible, especially in figure 4.28 (b). Alternate positive and negative V areas show strong upward and downward motions which indicate the presence of permanent streamwise vortices. As the flow goes further downstream from the step, streamwise vortices developing in the mixing layer cause the $U = 0$ isosurface to take a wavy shape in the spanwise direction and form the four lobes presented in figure 4.21, which results in a wavy shape of the mean reattachment line.

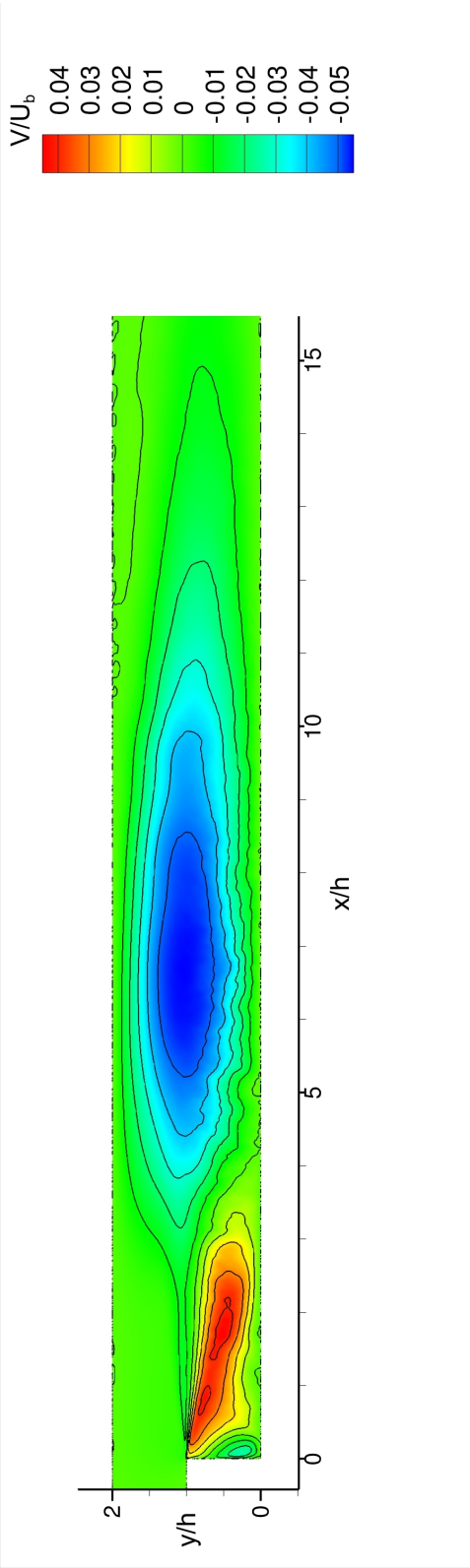

Figure 4.27: V velocity field contours.

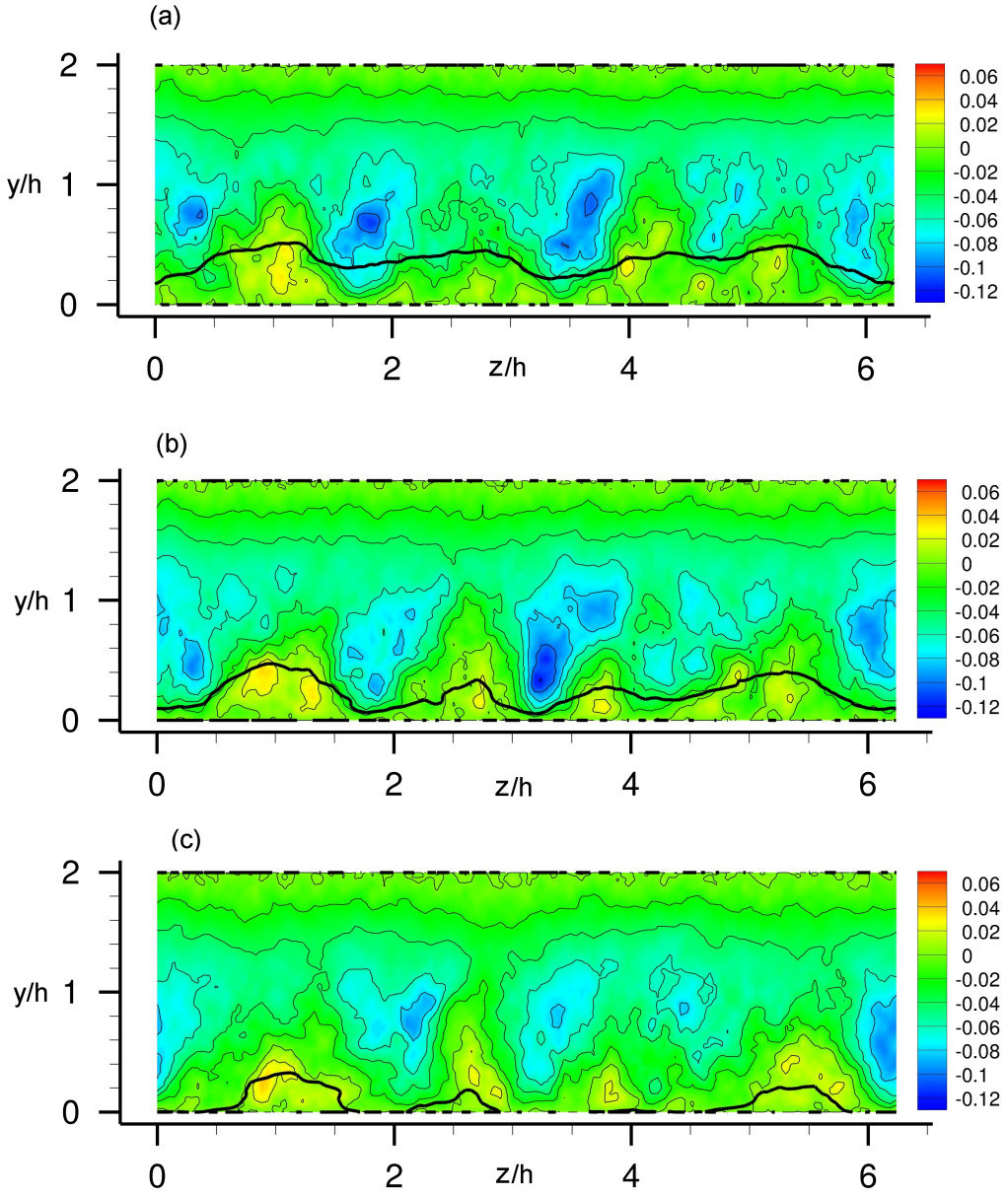

Figure 4.28: V velocity contours y-z slice - (a) $x = 6.0h$; (b) $x = 7.0h$; (c) $x = 8.0h$. Bold solid line marks $U = 0$.

4.3.5 Permanent streamwise vortices

The previous subsection along with figure 4.21 indicates that permanent streamwise vortices could form in the flow. This section investigates this matter further by examining the streamwise vorticity and the λ_2 vortex identification criterium by Jeong & Hussain (1995).

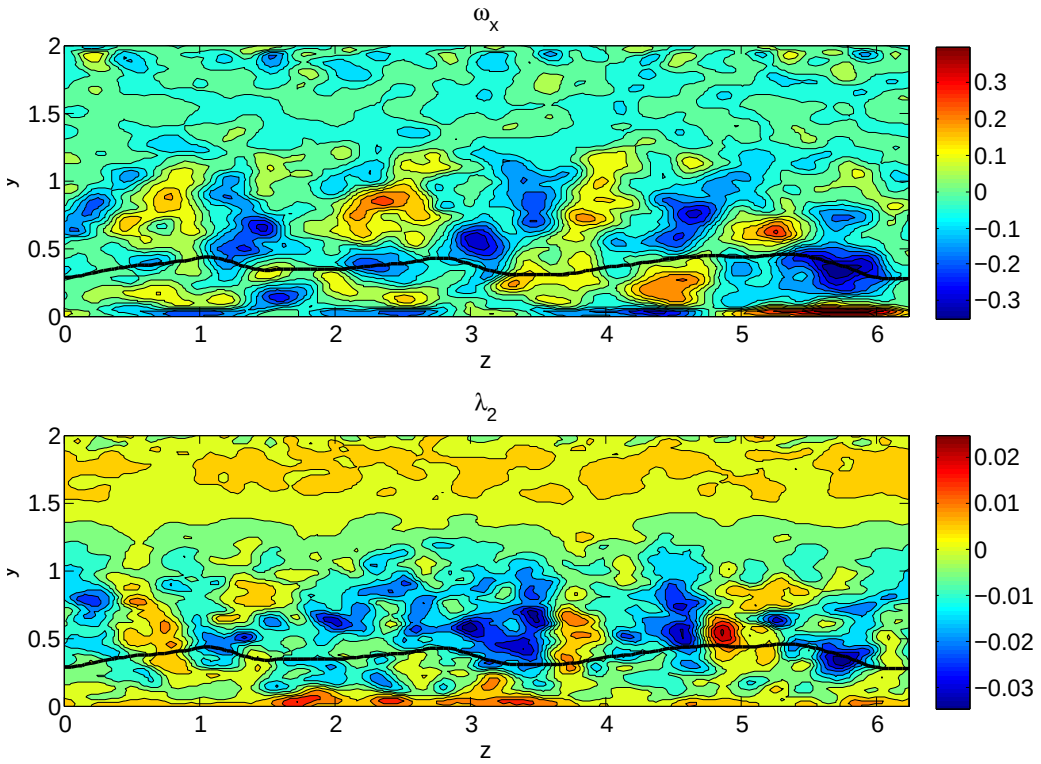

Figure 4.29: Streamwise vorticity and λ_2 contours y-z slice - $x = 6.0h$, top - ω_x, bottom - λ_2. Bold solid line marks $U = 0$. Smoothing extracted four areas where high negative vorticity coincides with high negative λ_2 ($x = 1.3h$, $x = 3h$, $x = 4.6h$, $x = 5.8h$, $y \approx 0.5h$). Those four vortices interact with the recirculation zone represented by the solid black line.

Figure 4.29 presents the y-z slice through ω_x (top) and λ_2 (bottom) at $x = 6h$. In order to obtain a clearer picture of the permanent streamwise vortices a

smoothing operation was performed on both graphs. The smoothing was done by interpolating data on an evenly spaced mesh and locally averaging values at neighbouring points.

It can be noted that the smoothing produced local errors near the domain boundaries, however they does not influence the picture in the area of interest. The vorticity revealed four pairs of positive and negative vorticity regions. Each negative vorticity area corresponds to one lobe of the $U = 0$ isoline. The λ_2 criterium indicates four negative regions in the vicinity of the isosurface lobes, which clearly indicates that the streamwise vortices do exist in this flow and cause the spanwise wavy structure of the recirculation eddy.

The question arises, however, whether this is a real physical phenomenon, or merely an effect of spanwise confinement in a too narrow computational domain. To address this problem two additional simulations were run with narrower domains: $L_z = 0.75\pi$ and $L_z = 1.25\pi$ with $N_z = 48$ and $N_z = 80$ respectively. The initial condition was generated from the original $N_z = 128$ simulation by keeping only the first 24 and 40 Fourier modes respectively and adding some random noise to the velocity field obtained this way. The simulations were run for $T = 120h/U_b$ time units. Figure 4.30 presents the streamwise vorticity and λ_2 criterium y-z slice showing two vortical structures and two recirculation region lobes marked by $U = 0$ isoline. Similar results are shown in figure 4.31, where two vortices are also clearly visible and possibly a third is forming near the right end of the domain (strongly negative area visible at the λ_2 plot). This shows that the presence of the persistent streamwise vortices is not caused by a spanwise confinement, but is a real phenomenon. Domains confined to $L_z < 2\pi$ produced reduced number

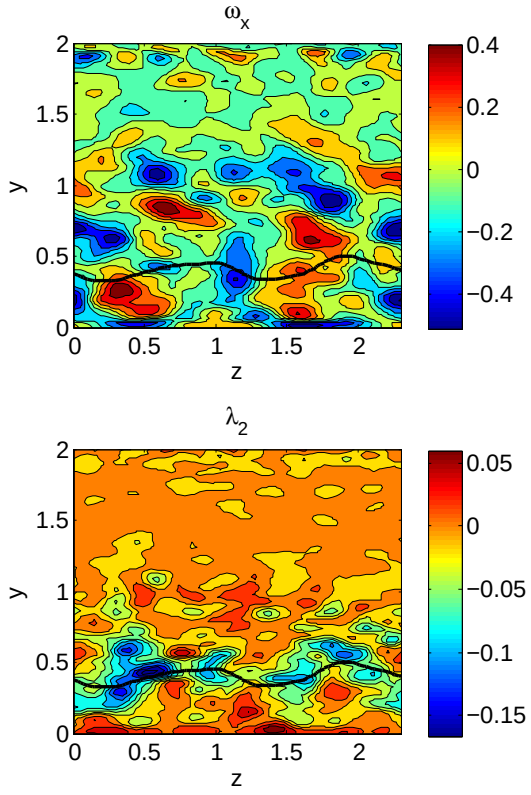

Figure 4.30: Streamwise vorticity and λ_2 contours y-z slice for $L_z = 0.75\pi$ simulation - $x = 6.0h$, top - ω_x, bottom - λ_2. Bold solid line marks $U = 0$. Two spanwise lobes of the recirculation eddy (solid black line) coincide with λ_2 minima.

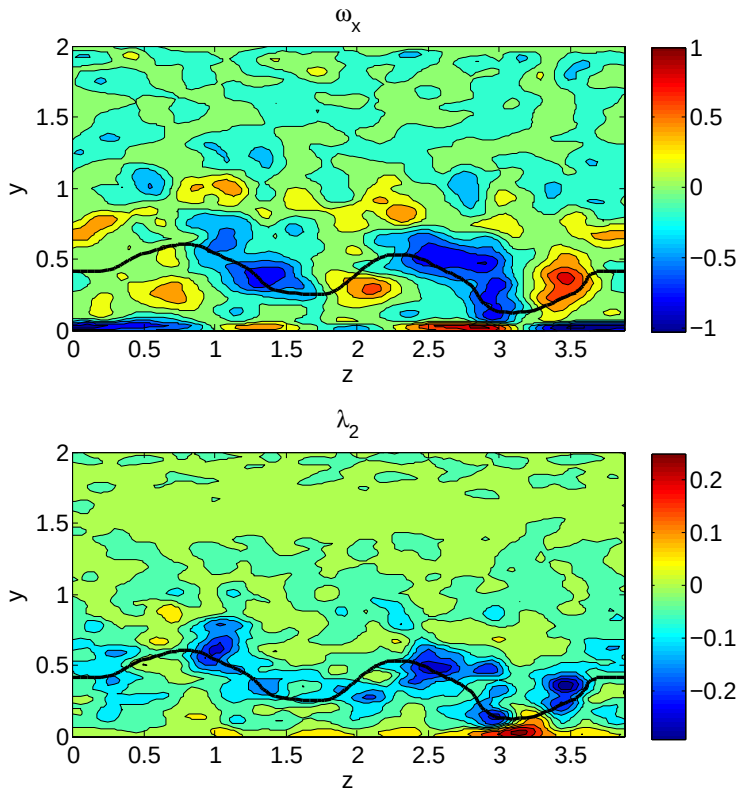

Figure 4.31: Streamwise vorticity and λ_2 contours y-z slice for $L_z = 1.25\pi$ simulation - $x = 6.0h$, top - ω_x, bottom - λ_2. Bold solid line marks $U = 0$. Three spanwise lobes of the recirculation eddy (solid black line) coincide with λ_2 minima. Two leftmost eddies on the bottom graph coincide with negative vorticity on the top graph. The rightmost vortex coincides with positive vorticity on the top graph.

of streamwise vortices.

4.3.6 Average wall shear stress

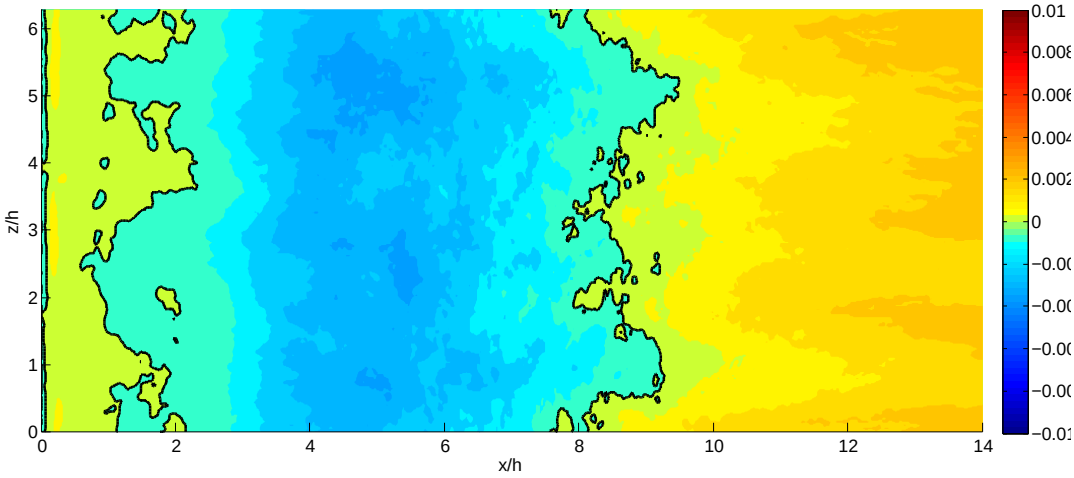

Figure 4.32: Average shear stress at the bottom wall - solid black line marks $\tau_w = 0$ and separates the regions of forward and reversed flow.

Figure 4.32 shows the average wall shear stress at the bottom wall. Three to four spanwise lobes of the main reattachment line are visible. This is the same effect as the one presented in figure 4.21 and discussed in Section 4.3.5. The structure of the secondary corner eddy can also be observed. It corresponds to the structure of the primary reattachment line. The tertiary corner eddy is visible as well. The figure shows that it does not necessarily span the entire width of the domain, as two regions of positive flow near the step wall are present at $y = 1.8$ and $y = 3.9$.

4.3.7 Turbulence intensity and Reynolds shear stress

Figure 4.33 to 4.37 present the streamwise evolution and contours of turbulence intensities $\sqrt{\overline{u'u'}}$, $\sqrt{\overline{v'v'}}$, $\sqrt{\overline{w'w'}}$ and Reynolds shear stress $\overline{u'v'}$ normalised with U_b^2. Turbulence intensity profiles (figure 4.33, 4.34, 4.36) show a sharp increase in the mixing layer up to $x = 2.0h$ downstream from the step. The streamwise turbulence intensity component maintains its original peak near the top wall until the flow enters the reattachment zone ($x = 8.0h$ to $x = 12.0h$, Fig. 4.33). Further downstream the peak is slowly regenerated. The first appearance of a near-wall peak in $\overline{u'u'}$ for the bottom wall is around $x = 8.0h$ in the reattachment area. The peak grows as the flow moves downstream. The initial profile from the inlet channel is not fully recovered within the domain.

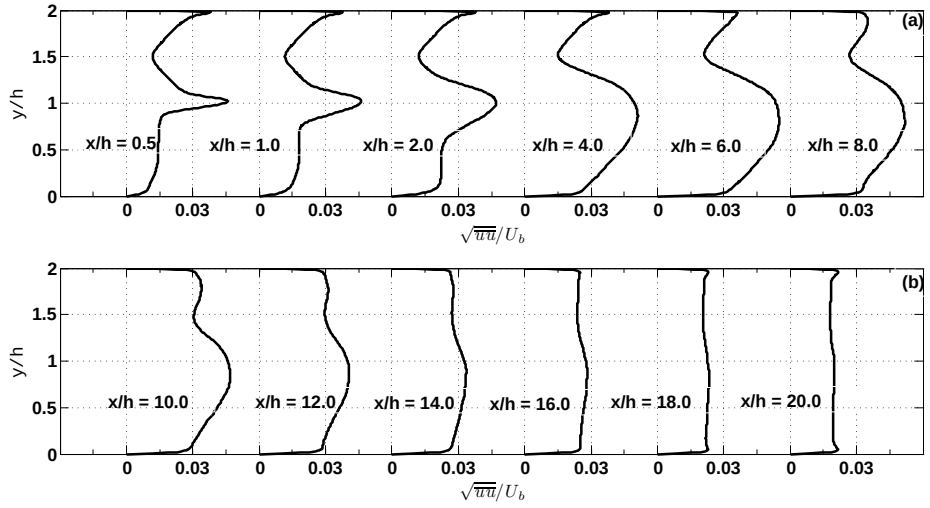

Figure 4.33: Streamwise turbulence intensity profiles $\sqrt{\overline{u'u'}}/U_b$ - (a) recirculation region; (b) reattachment and recovery region.

The initially slim high turbulence area ($x < 2.0h$) visible in figure 4.35 is spreading across the channel, mainly towards the bottom wall. The peak value $(\overline{u'u'})_{max} = 0.054U_b^2$ is located at $x = 5.3h$, $y = 0.85h$.

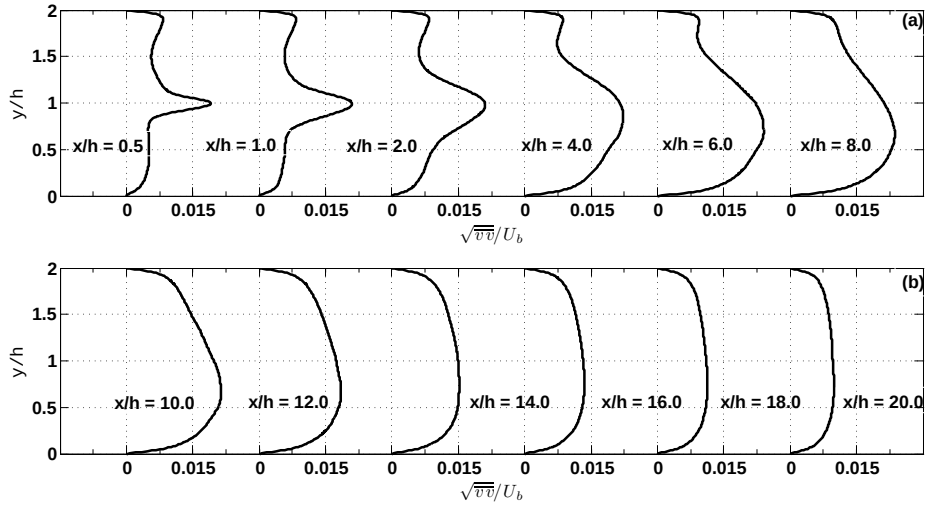

Figure 4.34: Vertical turbulence intensity profiles $\sqrt{\overline{v'v'}}/U_b$ - (a) recirculation region (b) reattachment and recovery region.

The vertical turbulence intensity component behaves similar to the horizontal one in the mixing layer. The maximum $(\overline{v'v'})_{max} = 0.026U_b^2$ is located at $x = 5.63h$, $y = 0.74h$. As the flows undergoes reattachment, the slight initial peak at the top wall disappears and does not regenerate further downstream, at either the top or the bottom wall. Far downstream the $\overline{v'v'}$ profile takes a more convex shape, as opposed to the initial profile in figure 4.2. This is due to the increased turbulence intensity in the middle of the channel.

The spanwise component $\overline{w'w'}$ follows the behaviour of the other turbulence intensity components in the mixing layer. The maximum $(\overline{w'w'})_{max} = 0.035U_b^2$

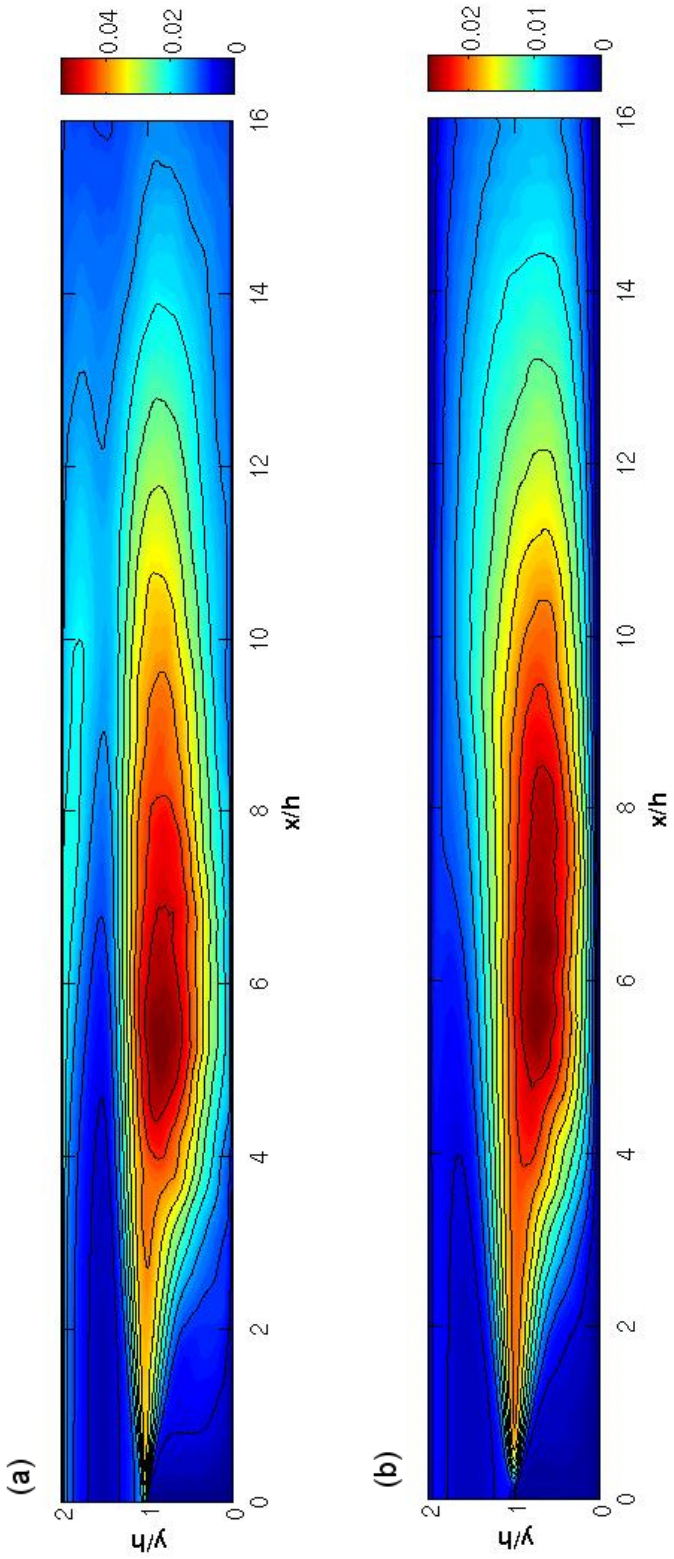

Figure 4.35: Contours of longitudinal and vertical shear stresses - (a) $\overline{u'u'}/U_b^2$; (b) $\overline{v'v'}/U_b^2$.

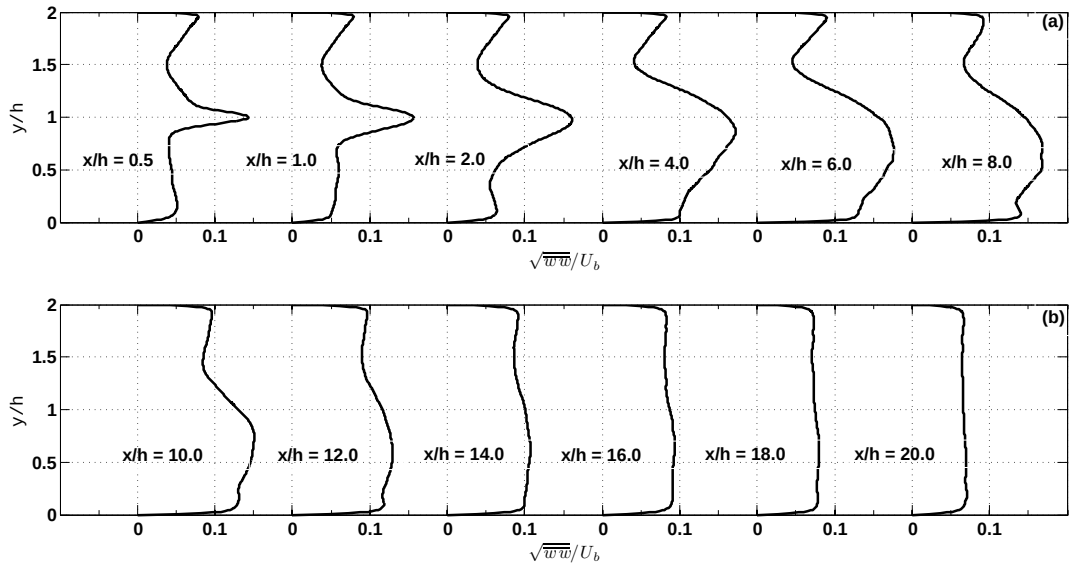

Figure 4.36: Spanwise turbulence intensity profiles - (a) recirculation region; (b) reattachment and recovery region.

is located at $x = 6.27h$, $y = 0.75h$. The profile in the regeneration zone shows increased turbulence intensity in the middle of the channel compared with the inlet profile in figure 4.2. As opposed to the other components of the Reynolds stress tensor, $\overline{w'w'}$ shows increased values near the bottom wall, especially in the area prior to the mean reattachment position ($6.5 < x < 8.0$).

The Reynolds shear stress component reaches its maximum $(-\overline{u'v'})_{max} = 0.019$ at $x = 5.47h$, $y = 0.8h$. The initial shape of the profile is almost recovered at $x = 20.0h$. However the middle part of the profile is still not linear.

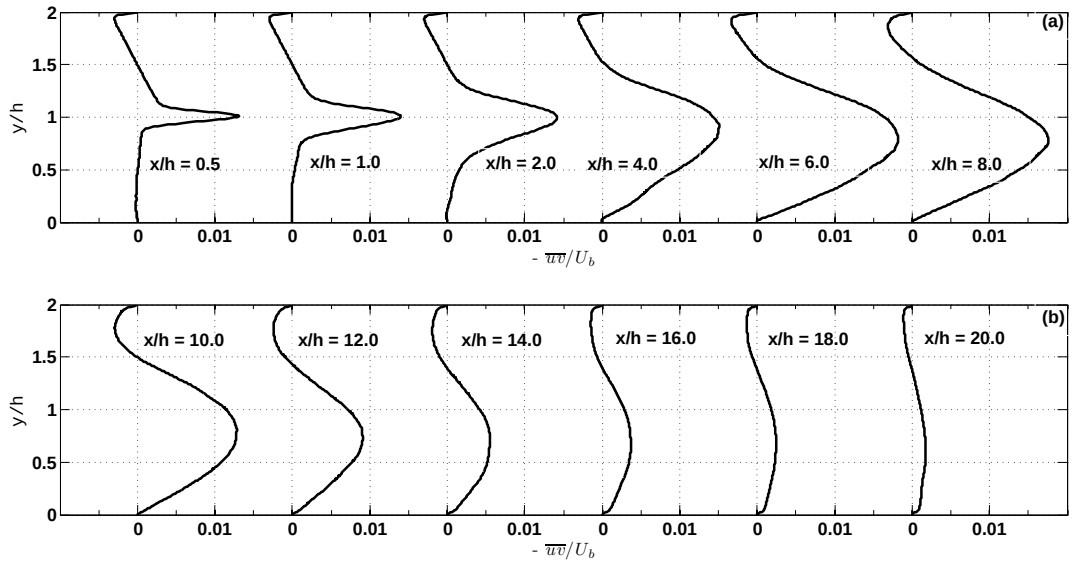

Figure 4.37: Reynolds stress profiles - (a) recirculation region; (b) reattachment and recovery region.

4.4 Instantaneous Results and Dynamics of BFS Flow

This section focuses on instantaneous results with special attention to the dynamics of the reattachment position. The wall shear stress dynamical behaviour is analysed, followed by an investigation of the interactions of vortical structures with the recirculation bubble. The snapshots shown were taken from animations used for the analysis of the flow.

4.4.1 Wall shear stress

In order to determine the reattachment position the location of zero wall shear stress was found. The time and spanwise averaged wall shear stress presented in

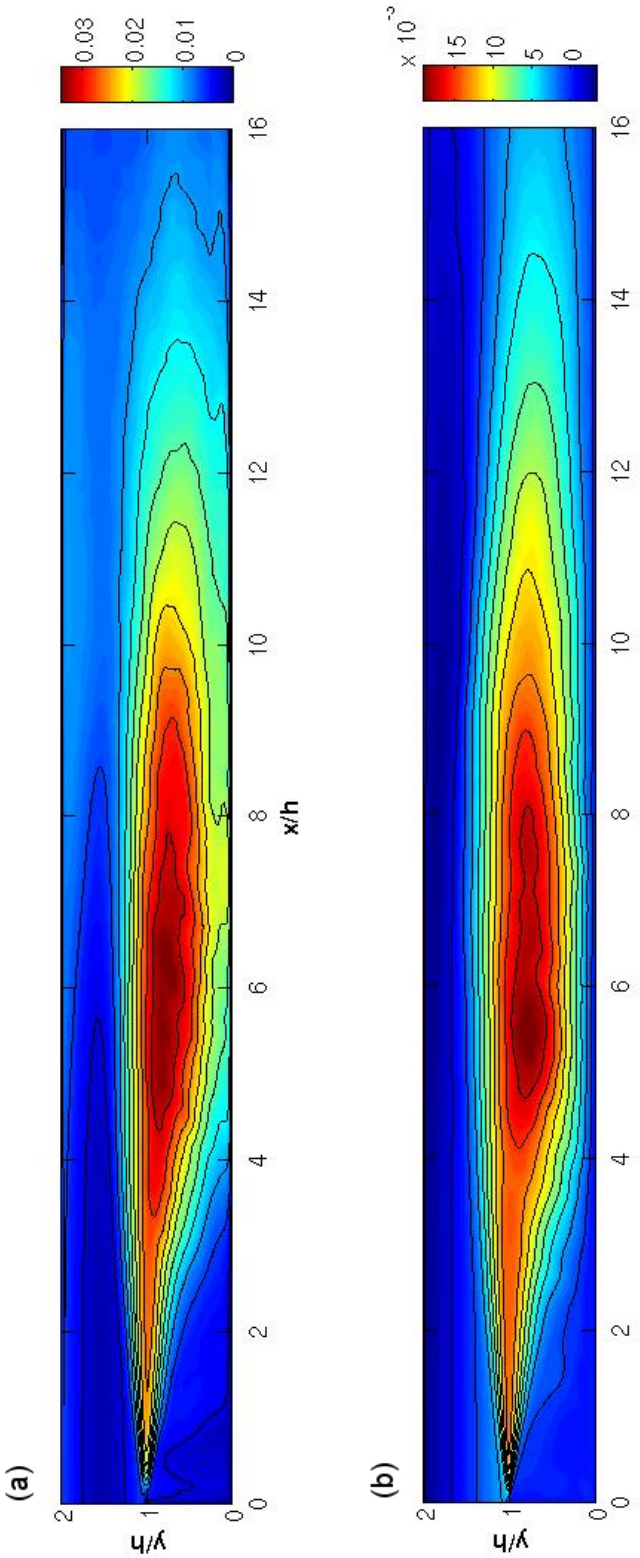

Figure 4.38: Contours of spanwise and Reynolds shear stresses - (a) $\overline{w'w'}/U_b^2$; (b) $-\overline{u'v'}/U_b^2$.

figure 4.4 and data in Table 4.2 indicate that the mean reattachment position is $X_r = 8.62h$. The discussion in Section 4.2.2 shows that these results fits with the prediction made by Armaly *et al.* (1983). Figure 4.39 presents a sequence of instantaneous wall shear stress contours. It is clear that in any instant there is no clear cut reattachment position, but rather a complex structure of forward and reverse flow patches. Four main regimes can be defined: forward flow for $x > 12h$, mixed flow - the reattachment zone for $6 < x < 12$, reversed flow for $2.5 < x < 6$ and the secondary bubble with forward flow near the wall for $x < 2.5$. Very close to the wall also the tertiary bubble exists, as discussed in section 4.3.2, however it is not clearly visible here due to the large scale of the picture.

The initial snapshots show a footprint of streamwise vortices discussed in Section 4.3.5. Three long streamwise areas of positive flow are forming between $t = 57.5h/U_b$ and $t = 62.5h/U_b$. At the same time the reverse flow area is moving downstream, which results in an increase of the instantaneous reattachment length X_r. At $t = 65.0h/U_b$ the three streaks of forward flow start to merge together into a larger spanwise structure that starts to cut-off a zone of reverse flow between $x = 7.5h$ and $x = 9.0h$. Further snapshots show how this enclosed reverse flow zone moves downstream and disappears at around $t = 70.0h/U_b$.

At the same time the complex structure of the secondary bubble can be observed. Instead of one compact zone of positive flow there is an intricate mixture of forward and reverse flow patches. No clear correlation between the behaviour of the main reattachment location and secondary bubble is visible.

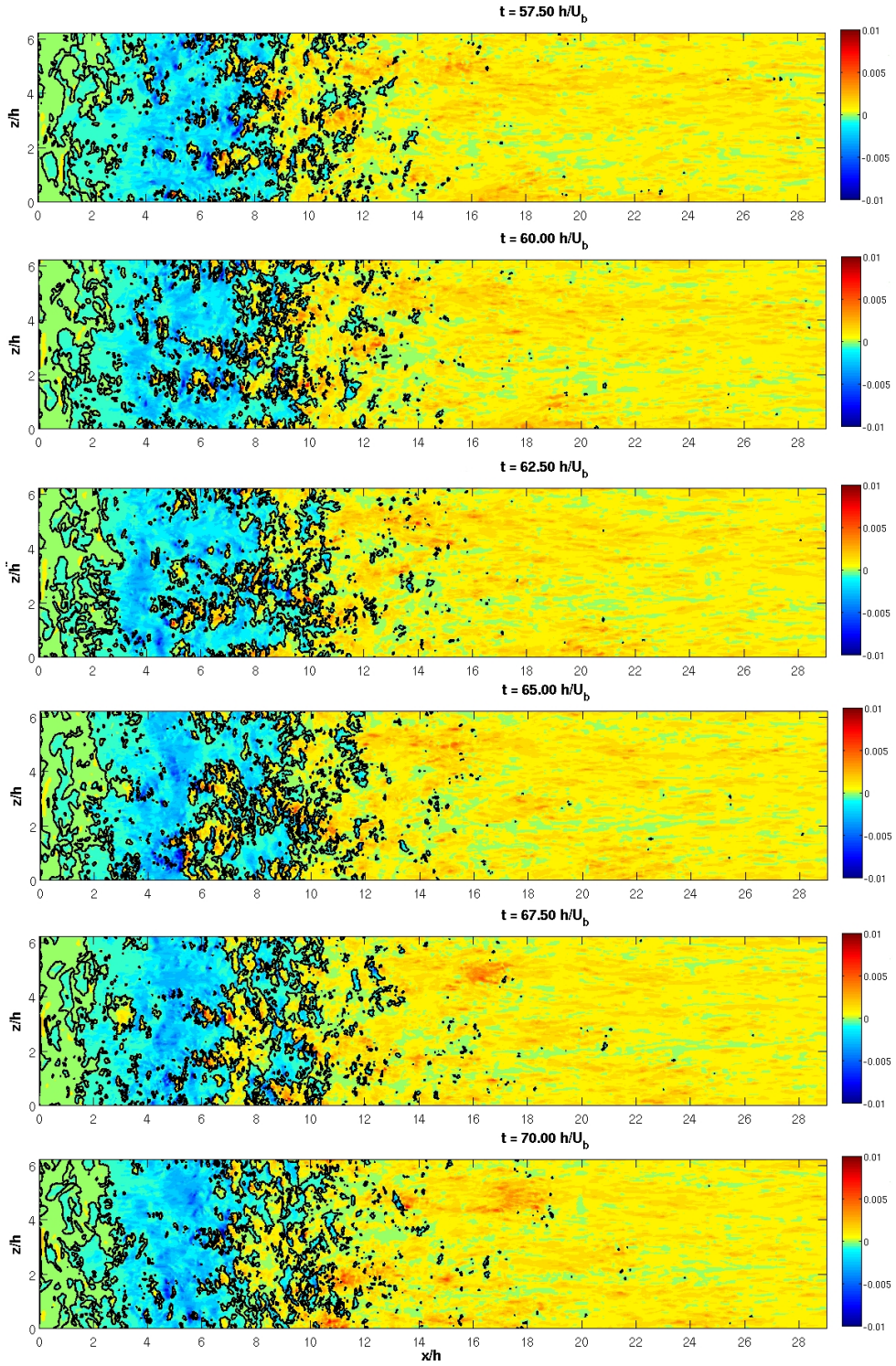

Figure 4.39: Instantaneous shear stress contours at the bottom wall - solid black line marks $\tau_w = 0$ and separates the regions of forward and reversed flow.

4.4.2 Oscillations of the Reattachment Position

The spanwise averaged time evolution of the bottom wall shear stress is plotted in figure 4.40. The solid line denotes zero shear stress. The evolution of the reattachment length forms an oscillating pattern of leaning saw-tooth shape. This visualises more clearly the behaviour of the reattachment position shown in figure 4.39. The reattachment length is increasing slowly in a roughly linear fashion (the average slope is $0.3U_b$). At some point in this evolution an area of forward flow starts to form upstream of the main reattachment position ($t = 65 - 67.5h/U_b$). This forward flow zone will eventually take over the downstream reverse flow zone closing the leaning saw-tooth shape ($t = 70h/U_b$). Simultaneously the upstream limit of the new forward flow area becomes the new reattachment position. This oscillating pattern is not very regular and carries some small scale structures on top of it.

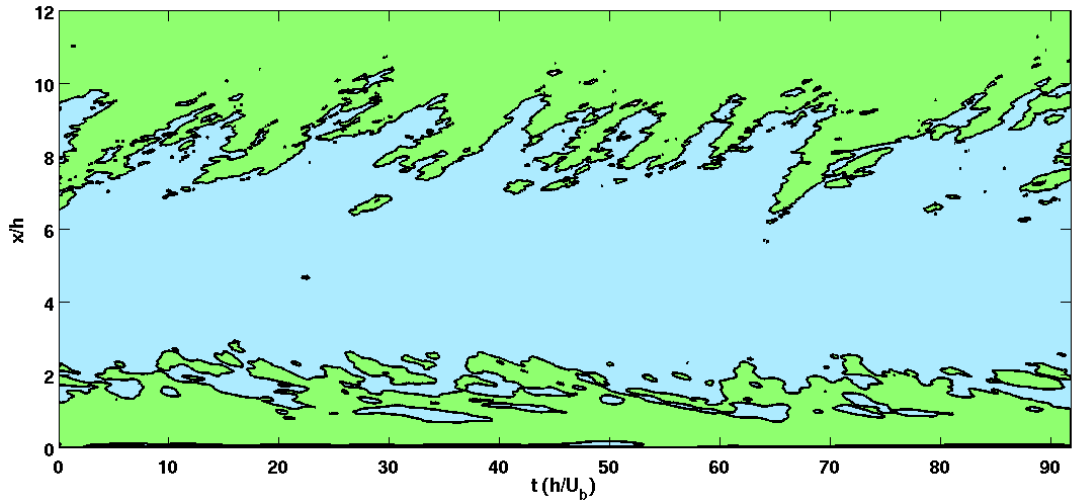

Figure 4.40: Evolution of the mean reattachment position - spanwise averaged wall shear stress: blue - negative, green - positive, black solid line - $\tau_w = 0$.

The secondary bubble lacks the small scale structure of the main recirculation zone, yet it appears to exhibit a pattern inverse to that of the primary reattachment position. The secondary bubble pattern is not as clear as the primary one, however there appears to be a negative slope of secondary structures (roughly $-0.08U_b$). The tertiary corner bubble does not exhibit any significant dynamic behaviour.

Oscillatory behaviour of the main reattachment position in a turbulent flow was observed by Le *et al.* (1997). Figure 4.41 shows the time evolution of the reattachment length for $Re_h = 4250$ (originally $Re = 5100$ based on U_0) and $ER = 1.2$. The saw-tooth shape is present, but it does not appear to be leaning like in figure 4.40. The slow increase in the reattachment length (slope $\approx 0.15U_0$) is followed by a rapid drop. Note that a roughly doubled Reynolds number results in doubled speed of reattachment length increase, however one needs to keep in mind that the two cases differ in geometry (expansion in a channel flow vs boundary layer flow over a step). Another similarity between the two cases is the frequency of the oscillations. In both figures there are approximately 8 saw-tooth shapes in $100h/U_b$ period.

A similar analysis was performed recently by Schafer *et al.* (2009). Figure 4.42 presents the same reattachment length evolution for transitional flow with a laminar inflow profile ($Re_h = 3000$, $ER = 2.0$). The reattachment position exhibits similar leaning saw-tooth shape as in the present study, however it is much more regular and its frequency is clearly higher. The approximate slope of the reattachment length increase is equal to $0.6U_b$.

Schafer *et al.* (2009) explain this phenomena by visualising vortices being shed

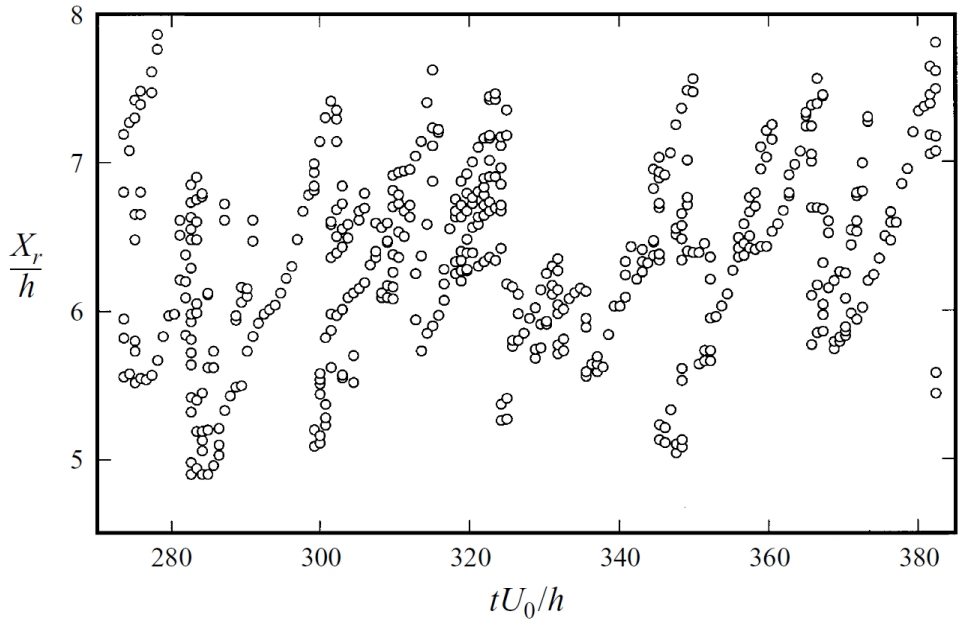

Figure 4.41: Time evolution of the spanwise averaged reattachment position - results of DNS simulation of turbulent flow over a step with $ER = 1.2$ by Le *et al.* (1997).

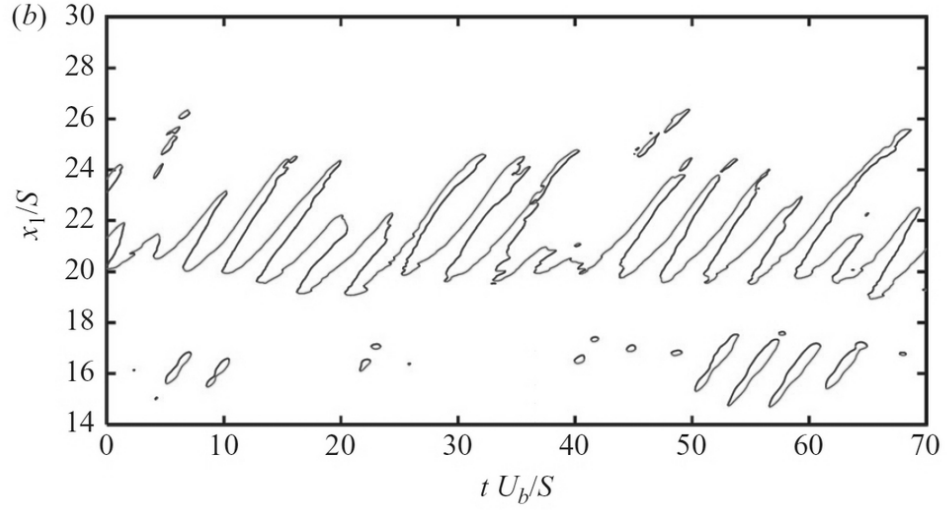

Figure 4.42: Time evolution of the spanwise averaged reattachment position - results of DNS simulation of transitional flow in a channel with $ER = 2$ by Schafer *et al.* (2009).

off the step edge, growing in the mixing layer and interacting with the recirculation zone. Vortices are visualised by low pressure isosurfaces (see figure 4.43), as the vortex cores are often characterised by pressure minima. The behaviour of the recirculation zone is represented by a streamwise velocity isosurface (figure 4.44). Vortical structures that impinge on the bottom wall cause a part of the reversed flow to separate from the main recirculation bubble. The separated reverse flow area is then convected downstream along with the vortex.

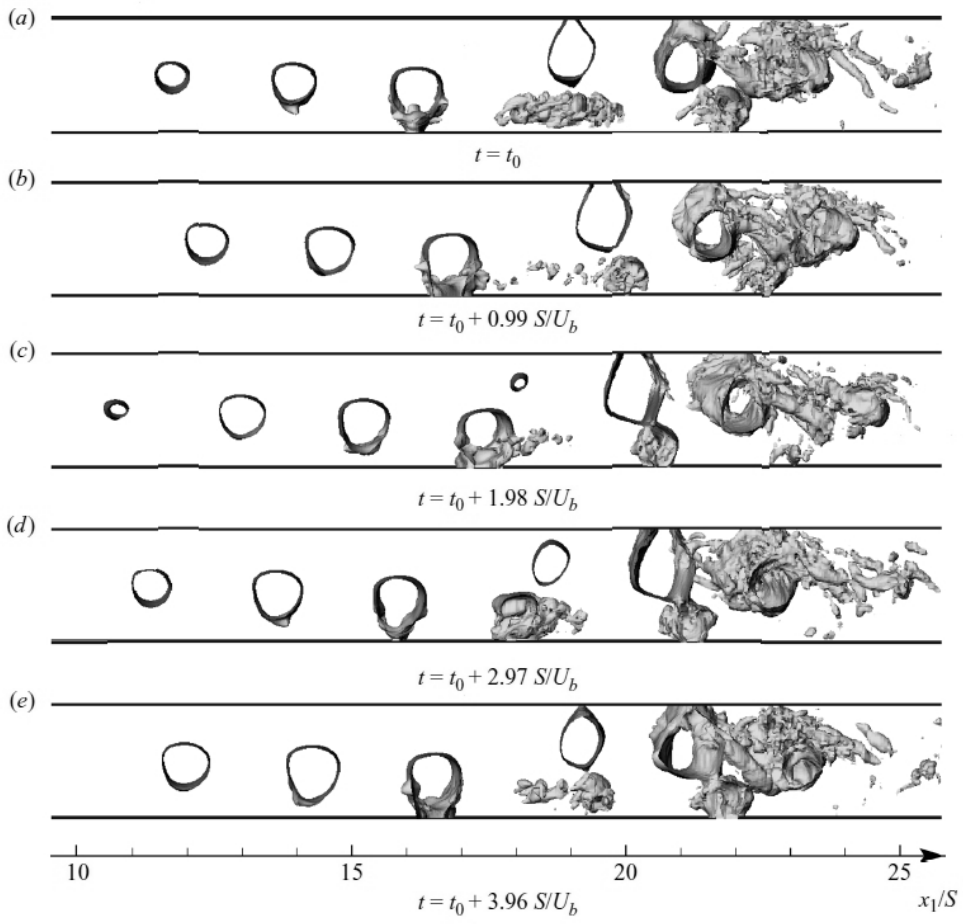

Figure 4.43: Snapshots of low pressure fluctuation isosurfaces - result by Schafer *et al.* (2009).

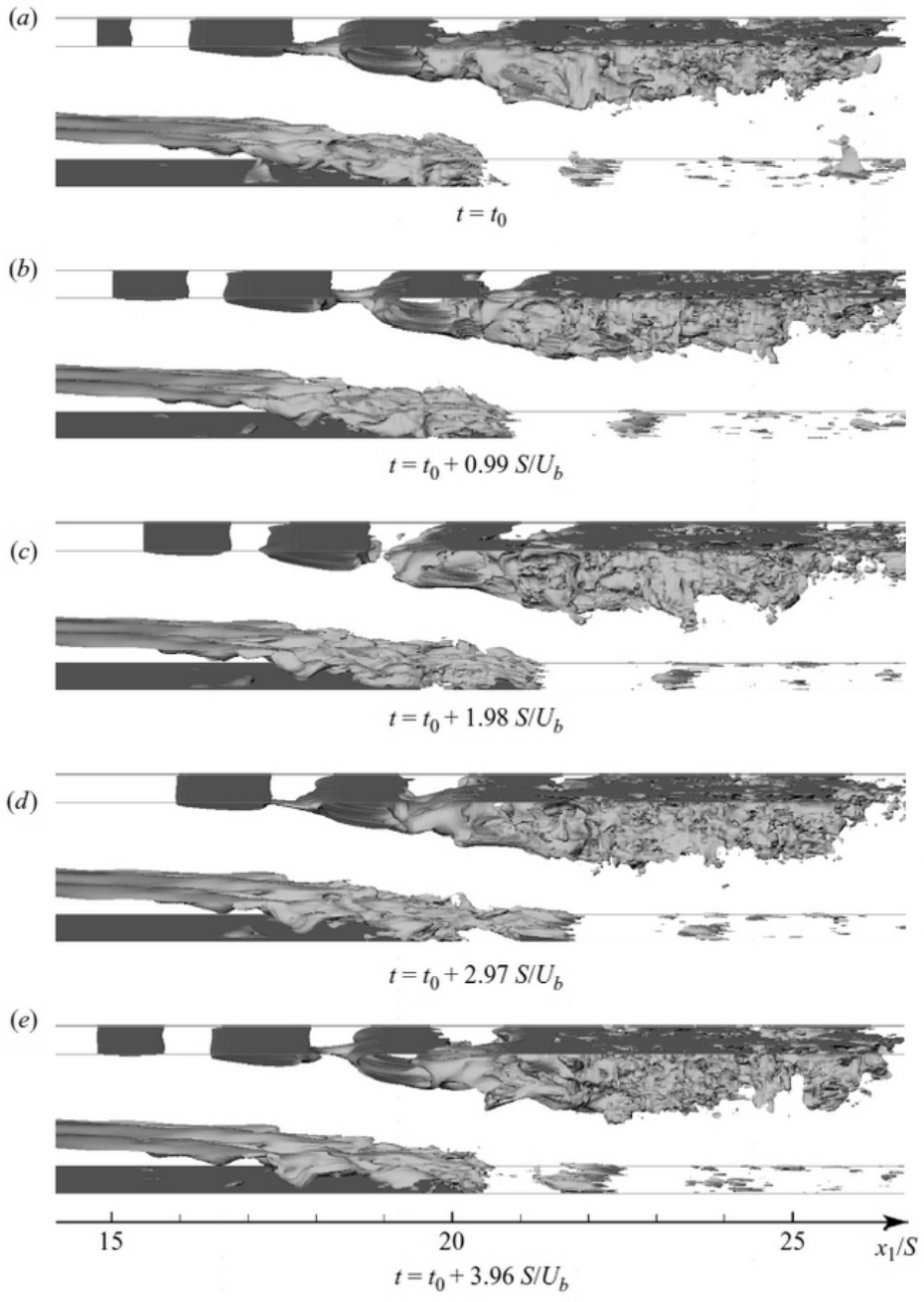

Figure 4.44: Snapshots of streamwise velocity isosurfaces - result by Schafer *et al.* (2009).

A similar visualisation for the present case is shown in figure 4.45. In the case of Schafer *et al.* (2009), the laminar inflow and low Re caused the vortices in the mixing layer to be very regular, spanning the entire width of the domain and breaking only after reattachment. In the present study the vortical structure in the shear layer is much more complex.

It is very difficult to draw any conclusions from this visualisation, therefore a spanwise-averaged result is presented in figure 4.46. It shows a much clearer picture of splitting of the recirculation eddy. Initially the recirculation area forms a compact bubble. The low pressure zone causes the bubble to stretch downstream. At $t = 65.0h/U_b$, the bubble starts to separate. The separated part of the reversed flow travels downstream with the low pressure zone, while the main recirculation bubble contracts quickly. The separated bubble vanishes as it travels downstream, while the main recirculation zone starts to grow again.

Figure 4.46 shows that the mechanism which governs the flapping of the primary reattachment position in turbulent flow is the same as for the transitional case studied by Schafer *et al.* (2009). The vortical structures that grow in the mixing layer interact with the wall by inducing a zone of reversed flow near the wall and causes the recirculation bubble to stretch. As the structure is convected downstream it carries the reversed flow zone with it, which causes the recirculation bubble to split. As the reversed flow zone disappears, the reattachment length rapidly shrinks. The difference for turbulent flow is that the vortical structures in the mixing layer are more complex than those in a transitional flow.

The quantitative analysis of the oscillatory behaviour of the reattachment position can be performed by studying the pressure and streamwise velocity fluc-

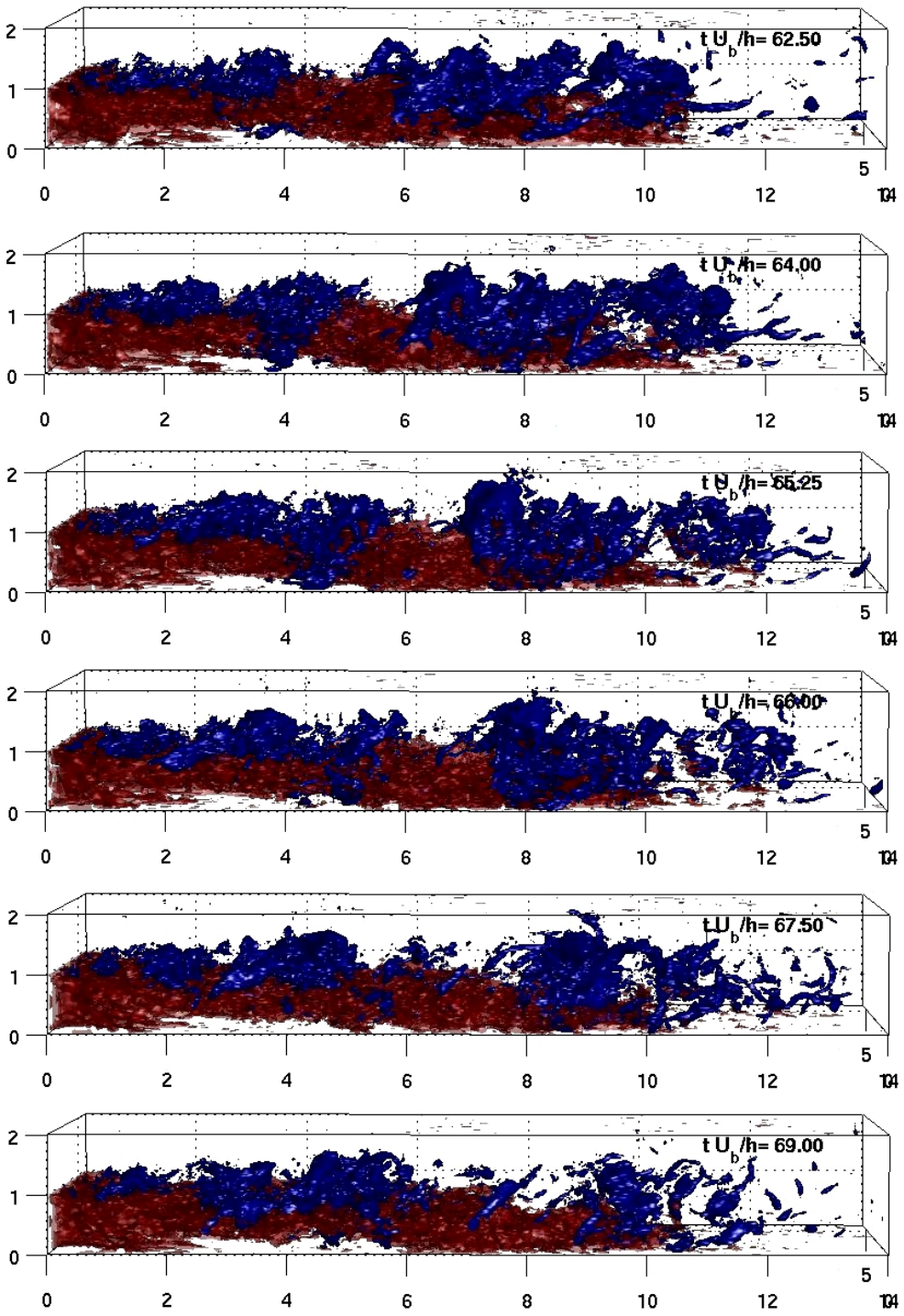

Figure 4.45: Negative pressure fluctuation p' and $U = 0$ isosurfaces - snapshots at different times: red - $U = 0$, blue - p'.

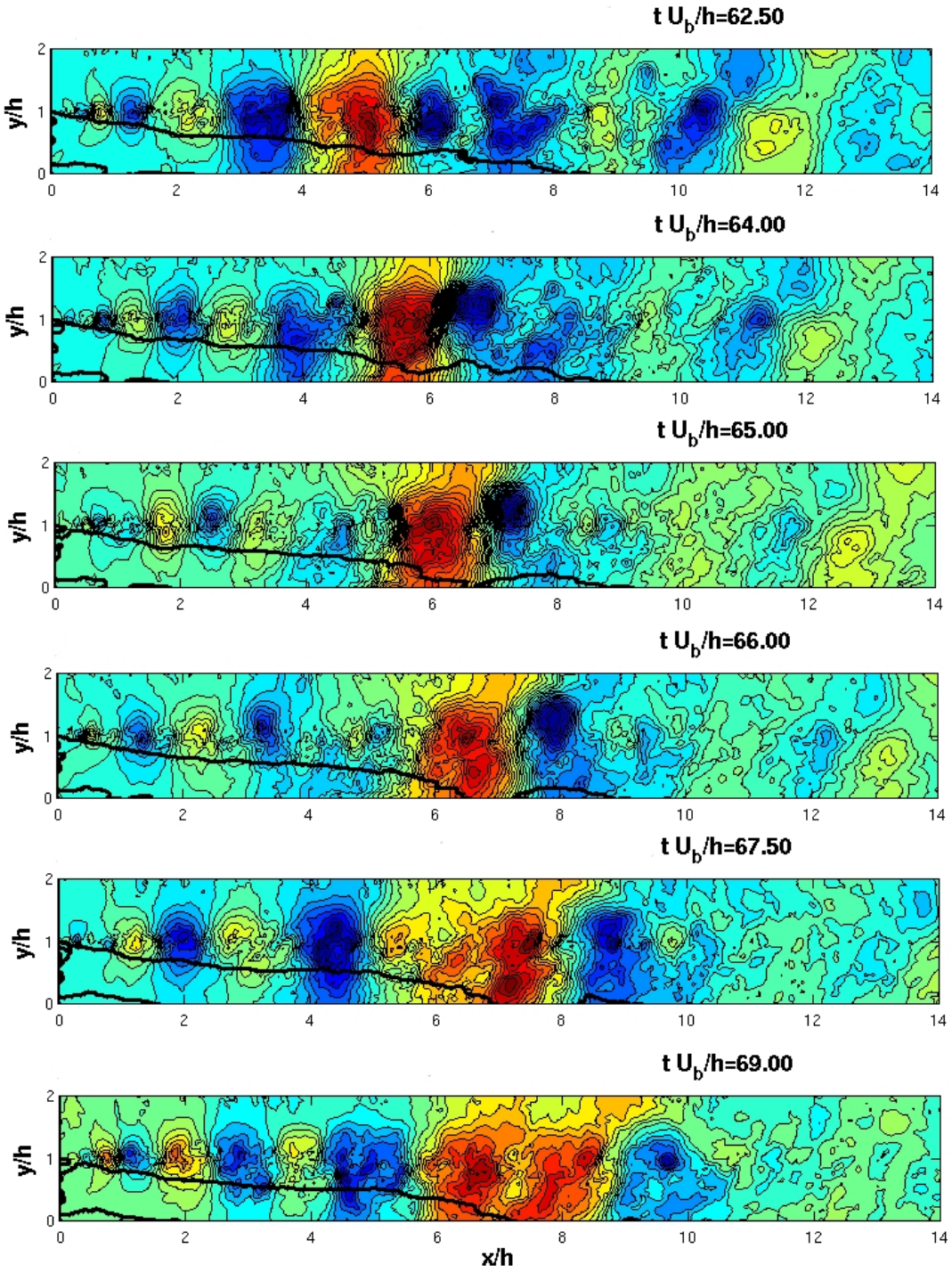

Figure 4.46: Snapshots of the spanwise averaged pressure fluctuation p' - pressure contours and $U = 0$ isoline (black solid line).

tuations near the reattachment position. Figure 4.47 (a) shows the history of spanwise averaged p' at $x = 8.0h$, $y = 0.01h$, and figure 4.47 (b) shows the history of spanwise averaged u' at the same point. Both signals look highly correlated on a large scale. The time history of velocity fluctuation represents the behaviour of the reattachment bubble, while the pressure fluctuations indicate the presence of vortical structures.

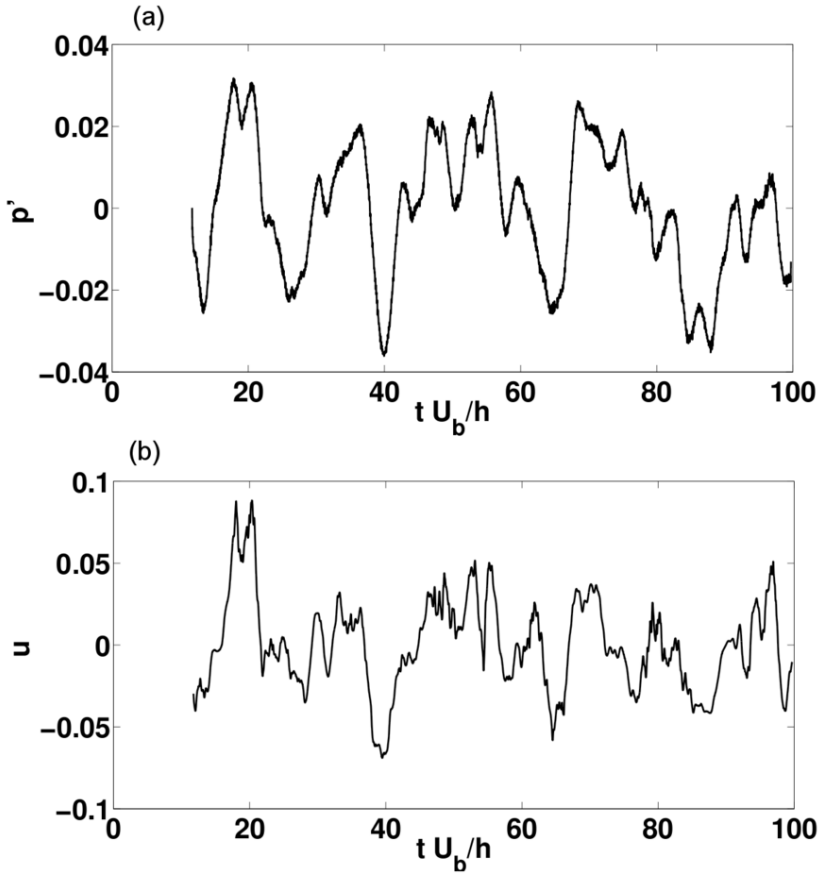

Figure 4.47: Pressure and streamwise velocity fluctuations history - spanwise averaged at $x = 8.0$, $y = 0.01$. (a) p' pressure fluctuation; (b) u' velocity fluctuation.

In order to investigate the correlation further, the spanwise averaged power spectrum of pressure and velocity fluctuation was taken at a number of locations

presented in figure 4.48. The locations cover the entire domain, including the inlet channel, recirculation bubble, mixing layer and reattachment.

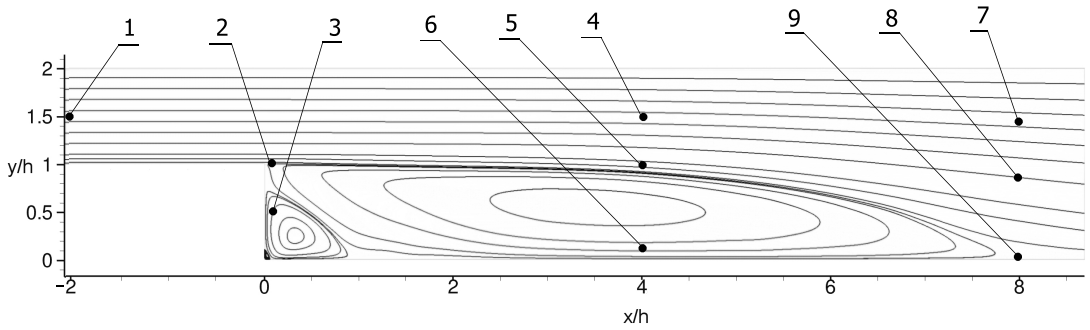

Figure 4.48: Location of pressure and velocity fluctuation measurements - point #1 (x=$-2h$, y=$1.5h$), #2 (x=$0.1h$, y=h), #3 (x=$0.1h$, y=$0.5h$), #4 (x=$4h$, y=$1.5h$), #5 (x=$4h$, y=h), #6 (x=$4h$, y=$0.1h$), #7 (x=$8h$, y=$1.5h$), #8 (x=$8h$, y=h), #9 (x=$8h$, y=$0.01h$).

Figure 4.49 shows the spectra for the inlet channel (a and b), a location near the step edge (c and d) and in the secondary corner eddy (e and f). The inlet spectrum shows clearly the peak corresponding to the inlet periodicity generated by the regeneration technique ($St = 0.127$), and subsequent subharmonics. In the following figures we will examine whether this frequency is present elsewhere in the flow and if it influences the oscillations of the reattachment position. Spectra near the step edge (figure 4.49 c and d) show only a slight peak at the regeneration frequency $St = 0.127$, both for the velocity and pressure fluctuations. Also a small peak near $St = 0.068$ is visible. A similar low frequency shows in the secondary corner eddy (figure 4.49 e and f). Other than that the spectra for the secondary eddy are smooth.

The velocity fluctuation spectra in the main flow and the mixing layer shown in the figure 4.50 (a) and (c) are fairly broadband. The regeneration frequency

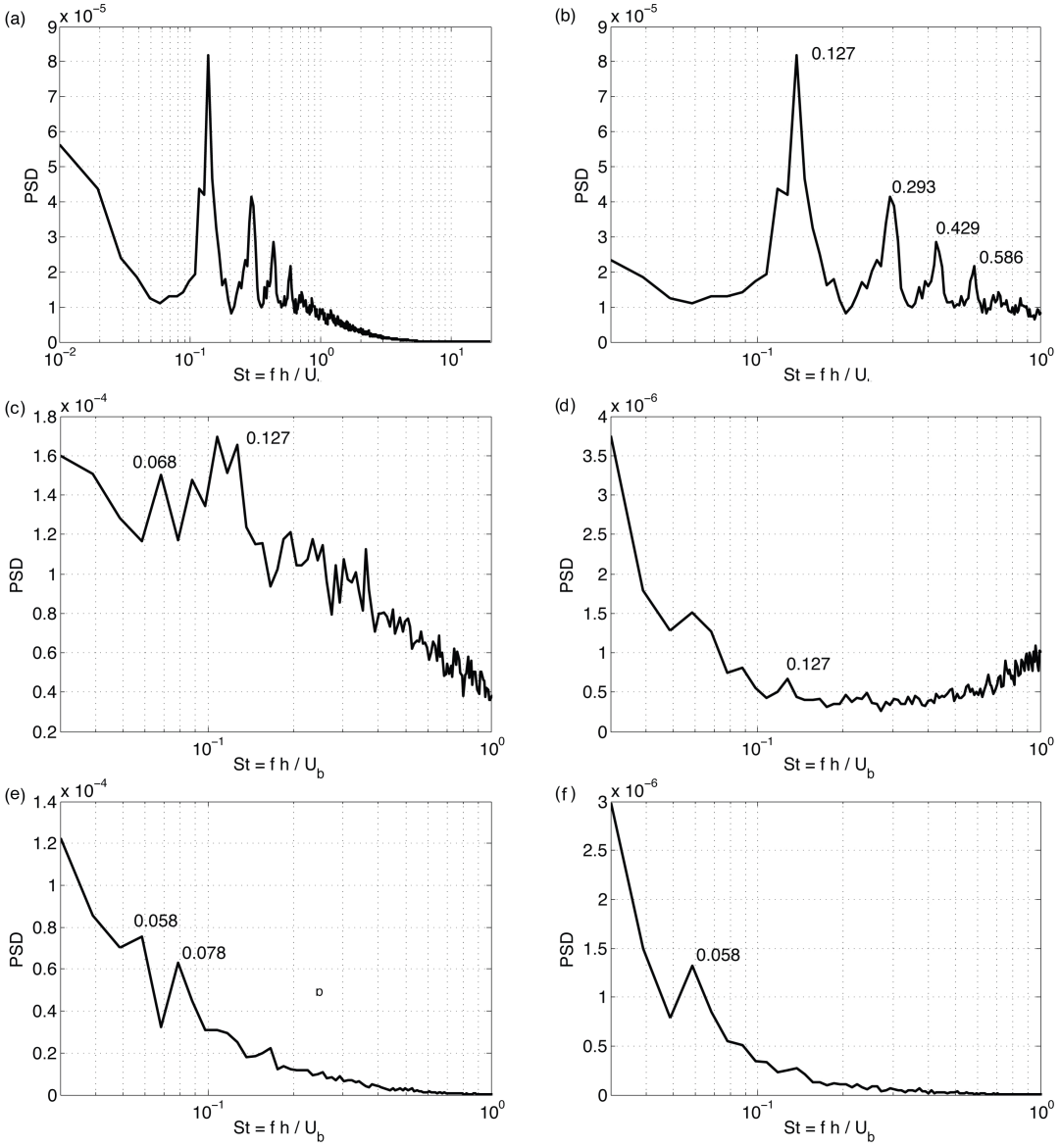

Figure 4.49: Spanwise averaged power spectrum of pressure and velocity fluctuation A - (a) point #1, full u' spectrum; (b) #1, range of frequencies of interest - clearly visible peaks due to inlet periodicity; (c) #2, u' spectrum; (d) #2, p' spectrum; (e) #3, u' spectrum; (f) #3, p' spectrum.

is present in the main flow (point #4), but the higher frequency of $St = 0.195$ is also present, and not only in the u' spectrum, but also in pressure fluctuations. Again, lower frequency of $St = 0.068$ shows up in all three locations in figure 4.50. This frequency is especially pronounced for p' graphs and for point #6 in the recirculation zone.

In figure 4.51 (a) and (b), which shows point #7 in the main flow, one can see the most pronounced frequency of $St = 0.078$, which occurs for both u' and p' spectra. A strong peak at this frequency is also present in the pressure fluctuation spectrum for point #8 (figure 4.51 d), but disappears in the velocity spectrum. Finally, it is strongly accented at the point near the reattachment (point #9, figure 4.51 e and f) for both pressure and velocity spectra. This clearly indicates that the presence of a vortex (represented by a pressure fluctuation) and behaviour of the reattachment position is correlated and tuned to a characteristic frequency of $St \approx 0.078$. As we have seen above, the frequency in the range $St = 0.068 - 0.078$ is present in the entire recirculation region and is fed back from the reattachment, through the primary recirculation eddy to the step edge at point #2. This in turn generates vortices of similar frequency in the mixing layer, which can be seen in figure 4.50 (c) and (d) as well as 4.51 (c) and (d). Those vortices cause the oscillations of the reattachment position (point #9), which influences the entire recirculation eddy and closes the feedback loop. Moreover, this result agrees with previous findings of Le *et al.* (1997) who report $St \approx 0.06$ as a frequency of the reattachment flapping. Similarly Metais (2001) found the characteristic flapping frequency $St \approx 0.07$, while Silveira Neto *et al.* (1993) provides the value $St = 0.08$ for large Kelvin-Helmholtz structures in the mixing

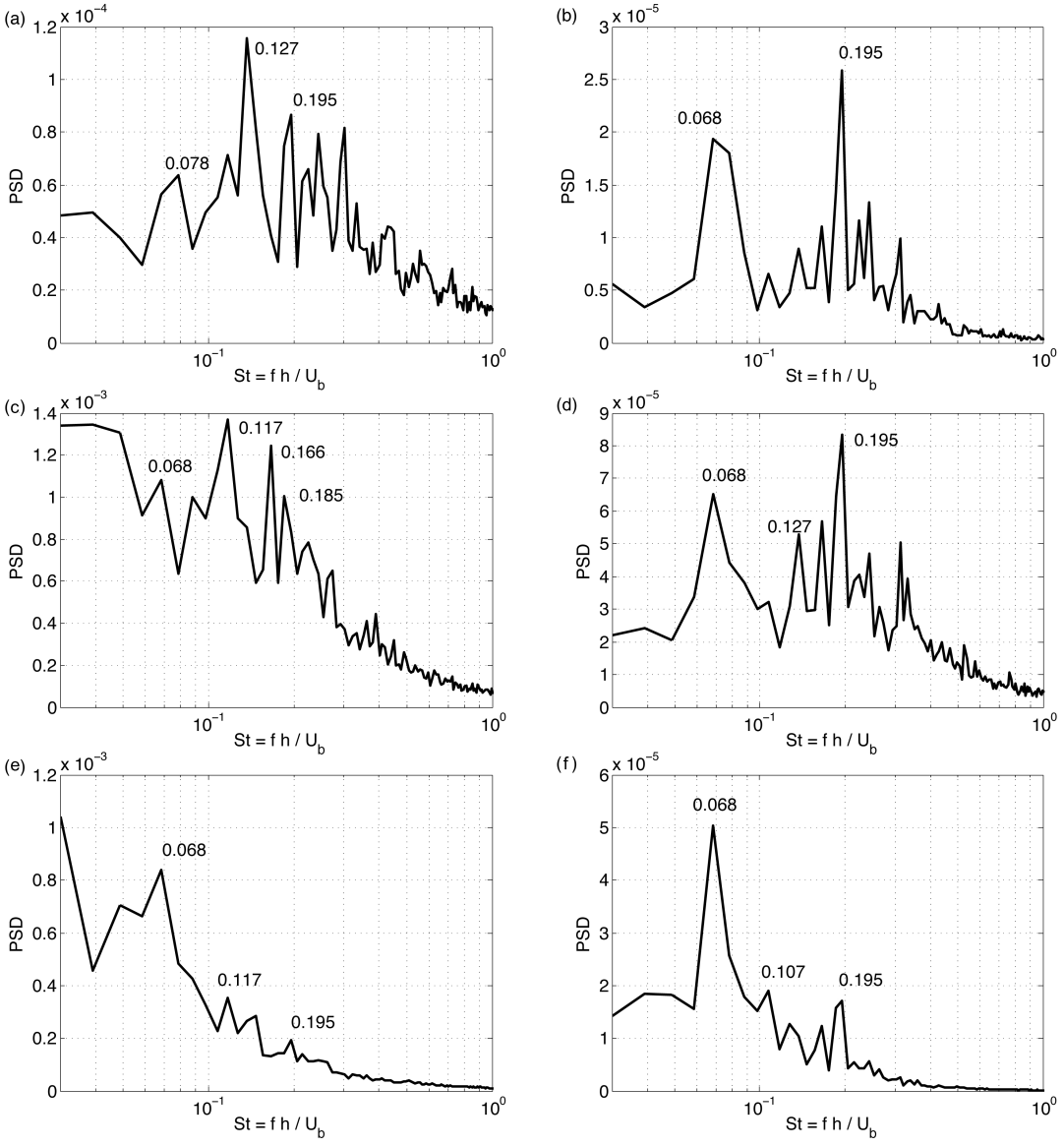

Figure 4.50: Spanwise averaged power spectrum of pressure and velocity fluctuation B - (a) point #4, u' spectrum; (b) #4, p' spectrum; (c) #5, u' spectrum; (d) #5, p' spectrum; (e) #6, u' spectrum; (f) #6, p' spectrum.

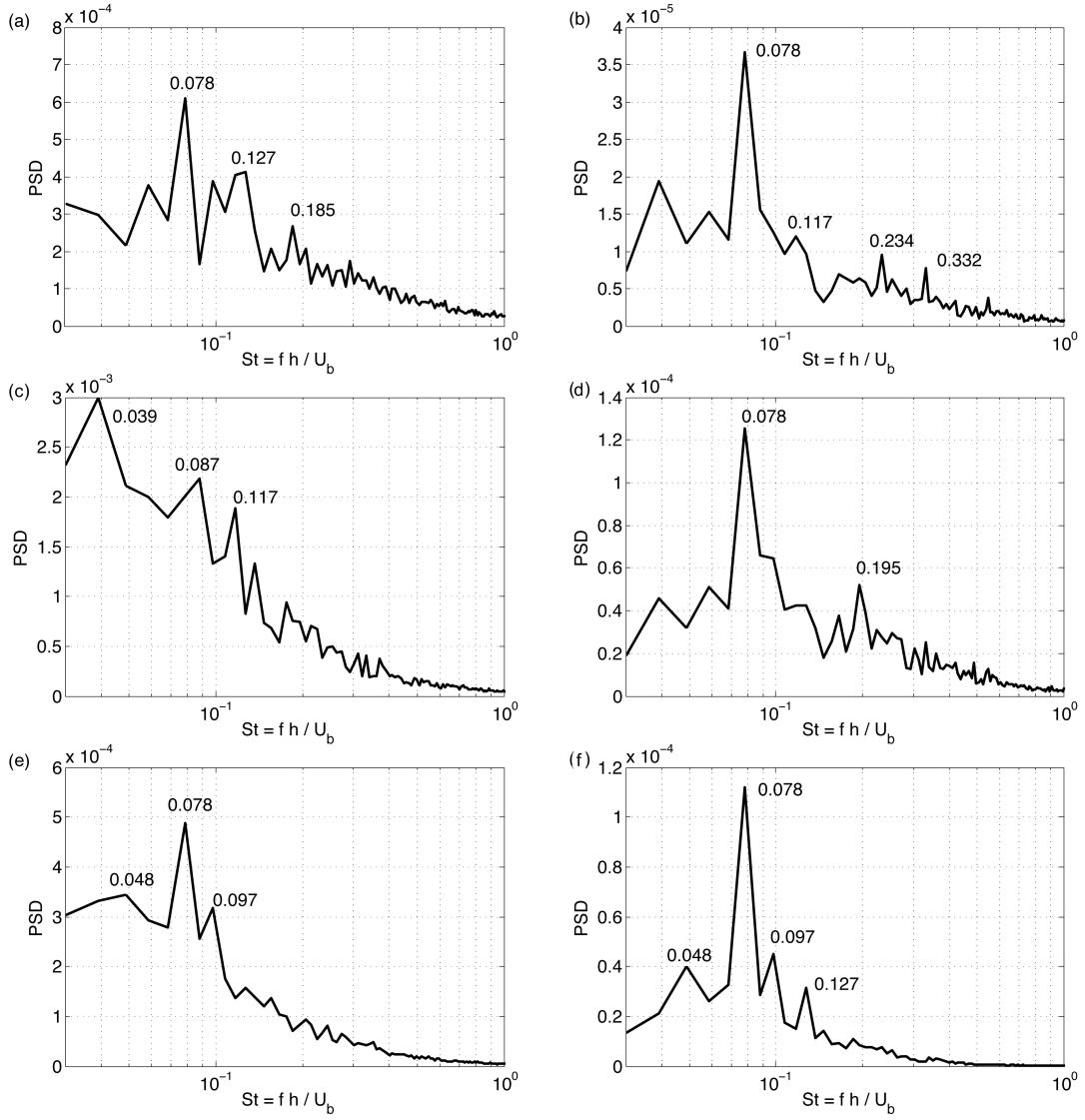

Figure 4.51: Spanwise averaged power spectrum of pressure and velocity fluctuation C - (a) point #7, u' spectrum; (b) #7, p' spectrum; (c) #8, u' spectrum; (d) #8, p' spectrum; (e) #9, u' spectrum; (f) #9, p' spectrum.

layer. Schafer *et al.* (2009) report $St = 0.266$, however the quantitative agreement in this case cannot be expected due to the presence of the laminar flow at the inflow of this simulation.

The regeneration frequency of $St = 0.127$ is present in the flow, especially in the main stream (figure 4.49 a, 4.50 a and 4.51 a), but it tends to show up in the u' spectra, which could indicate that it does not have an influence on the vortex formation in the mixing layer.

In many places in the mixing layer and the main flow the higher frequency of $St = 0.195$ shows up, which is not present in the recirculation area or the inflow channel (see figure 4.50 a, b and d). Its origins cannot therefore be explained by the regeneration technique or reattachment flapping.

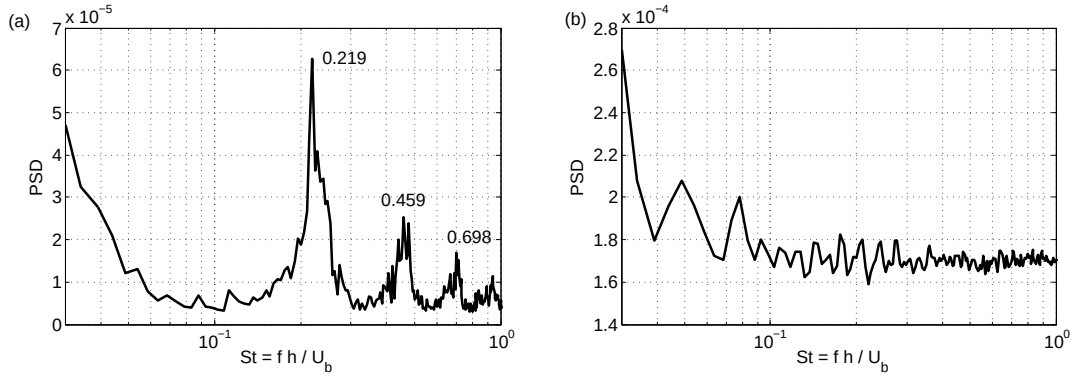

Figure 4.52: Spanwise averaged power spectrum at the inlet of the additional simulation - point #1. (a) u' spectrum; (b) p' spectrum.

In order to further exclude the influence of the regeneration frequency on the reattachment oscillations, an additional simulation with shorter regeneration length ($L_i = 5h$) was performed. In order to save computational resources the spanwise length was set to $L_z = 0.75\pi$ and the spanwise resolution $N_z = 48$.

Figure 4.52 presents the spectrum taken in the inlet channel of this additional simulation. It clearly shows the new regeneration frequency of $St = 0.219$ and its harmonics. Figure 4.53 presents velocity and pressure fluctuation spectra near the reattachment position at point #9. The characteristic frequency is $St = 0.068$, which is slightly lower than for the original simulation, but still in the regime $St = 0.068 - 0.078$ identified as a characteristic frequency of the recirculation zone. This shows that the increased regeneration frequency does not have an influence on the reattachment oscillations.

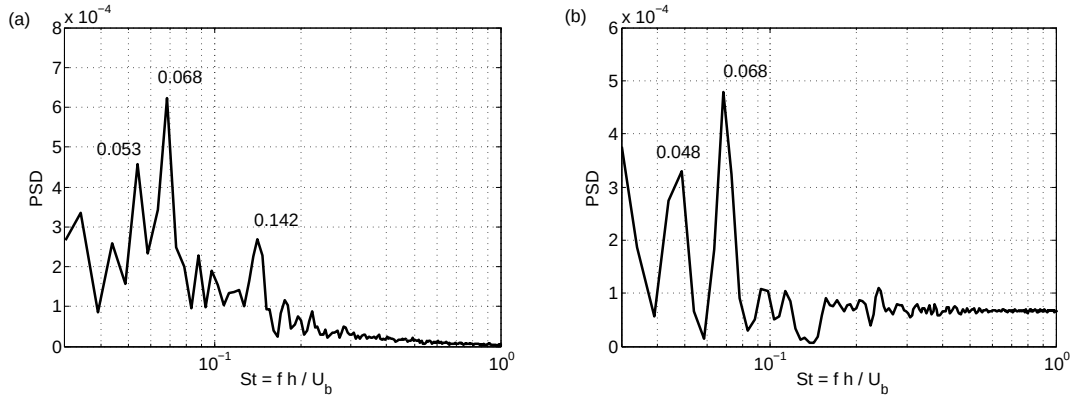

Figure 4.53: Spanwise averaged power spectrum near the reattachment position of the additional simulation - point #9. (a) u' spectrum; (b) p' spectrum.

4.5 Small-Scale Energy Transfer

The energy transfer analysis consists of the decomposition of the velocity field into large and small scales and an investigation of the non-linear interactions between them. The large scale flow field represents the solution that could be

obtained by LES, and is computed from the DNS result using filtering techniques described in Section 2.7. In order to make up for the lack of resolution, an LES model has to represent the effect of small (subgrid) scales on the large scale flow. By studying the small scale energy transfer we can assess existing subgrid-scale models and investigate the possibilities for deriving new ones.

This kind of approach was used by Domaradzki *et al.* (1993) and Kerr *et al.* (1996) to look for correlations of large-scale quantities with small-scale transfer in isotropic turbulence simulations. This section presents results of similar analysis applied to the flow around a backward-facing step, with a special interest in the reattachment area.

4.5.1 Basic quantities

The Navier-Stokes equation (2.1) can be rewritten as

$$\frac{\partial u_i}{\partial t} = -\frac{\partial p}{\partial x_i} - \nu \Delta u_i + \mathbb{N}_i(\mathbf{x}), \tag{4.2}$$

where the nonlinear term

$$\mathbb{N}_i(\mathbf{x}) = -u_j \frac{\partial u_i}{\partial x_j}. \tag{4.3}$$

The summation convention applies, and $\mathbf{u} = \{u_i\}$ corresponds to $\mathbf{u} = [u, v, w]$ in previous chapters.

If $\mathcal{L}$ denotes a quantity filtered using (2.101) and $\mathcal{S}$ denotes small scales that are defined as

$$u_i^{\mathcal{S}} = u_i - u_i^{\mathcal{L}}, \tag{4.4}$$

then the large-scale part of (4.2) can be expressed as

$$\frac{\partial u_i^{\mathcal{L}}}{\partial t} = -\frac{\partial p^{\mathcal{L}}}{\partial x_i} - \nu \Delta u_i^{\mathcal{L}} + \mathbb{N}_i^{\mathcal{L}}(\mathbf{x}) + \mathbb{N}_i^{\mathcal{S}}(\mathbf{x}). \tag{4.5}$$

The contribution of small-scale velocities is expressed through the non-linear term $\mathbb{N}_i^{\mathcal{S}}(\mathbf{x})$.

The transport equation of a large-scale turbulent kinetic energy is given by

$$\frac{\partial E(\mathbf{x})}{\partial t} = \nu u_i^{\mathcal{L}} \Delta u_i^{\mathcal{L}} + T^{\mathcal{L}}(\mathbf{x}) + T^{\mathcal{S}}(\mathbf{x}), \tag{4.6}$$

where

$$E(\mathbf{x}) = \frac{1}{2} u_i^{\mathcal{L}} u_i^{\mathcal{L}}, \tag{4.7}$$

$$T^{\mathcal{L}}(\mathbf{x}) = u_i^{\mathcal{L}} N_i^{\mathcal{L}}(\mathbf{x}), \tag{4.8}$$

$$T^{\mathcal{S}}(\mathbf{x}) = u_i^{\mathcal{L}} N_i^{\mathcal{S}}(\mathbf{x}), \tag{4.9}$$

$T^{\mathcal{L}}(\mathbf{x})$ is the large-scale energy transfer and $T^{\mathcal{S}}(\mathbf{x})$ is the small-scale energy transfer.

Traditionally (4.5) is presented as

$$\frac{\partial \overline{u}_i}{\partial t} = -\frac{\partial \overline{p}}{\partial x_i} - \nu \Delta \overline{u}_i + \frac{\partial \mathcal{T}_{ij}}{\partial x_j} + \frac{\partial \tau_{ij}}{\partial x_j}, \tag{4.10}$$

where

$$\mathcal{T}_{ij} = \overline{\overline{u}_i \overline{u}_j}, \tag{4.11}$$

$$\tau_{ij} = \overline{u_i u_j - \overline{u}_i \overline{u}_j} \tag{4.12}$$

and $\overline{u}$ corresponds to $u^{\mathcal{L}}$. The term τ_{ij} is the subject of modelling efforts, usually expressed also as a subgrid-scale dissipation $\epsilon_{SGS} = \tau_{ij} S_{ij}$, where S_{ij} is given by (4.16) below. By comparing (4.5) and (4.10) it is clear that $N_i^{\mathcal{S}}$ corresponds to $\frac{\partial \tau_{ij}}{\partial x_j}$, and that, instead of τ_{ij}, will be the focus of this investigation.

4.5.2 Large scale quantities correlations

In order to approximate the small-scale non-linear term $\mathbb{N}_i^{\mathcal{S}}$, we are going to compare the small-scale energy transfer $T^{\mathcal{S}}(\mathbf{x})$ given by (4.9) to four large-scale quantities:

- kinetic energy

$$E(\mathbf{x}) = \frac{1}{2} u_i^{\mathcal{L}} u_i^{\mathcal{L}}, \tag{4.13}$$

- enstrophy

$$O(\mathbf{x}) = \frac{1}{2} \omega_i^{\mathcal{L}}(\mathbf{x}) \omega_i^{\mathcal{L}}(\mathbf{x}), \tag{4.14}$$

  where $\omega_i^{\mathcal{L}}(\mathbf{x})$ is the large-scale vorticity defined as $\omega^{\mathcal{L}}(\mathbf{x}) = \nabla \times \mathbf{u}^{\mathcal{L}}$

- viscous dissipation

$$D(\mathbf{x}) = \frac{1}{2} \nu S_{ij}(\mathbf{x}) S_{ij}(\mathbf{x}), \tag{4.15}$$

where

$$S_{ij}(\mathbf{x}) = \frac{1}{2}\left(\frac{\partial u_i^{\mathcal{L}}}{\partial x_j} + \frac{\partial u_j^{\mathcal{L}}}{\partial x_i}\right) \tag{4.16}$$

is the rate-of-strain tensor,

- enstrophy production

$$\omega \mathbf{S} \omega(\mathbf{x}) = \omega_i^{\mathcal{L}}(\mathbf{x}) S_{ij}(\mathbf{x}) \omega_j^{\mathcal{L}}(\mathbf{x}). \tag{4.17}$$

Figure 4.54 presents the qualitative comparison of those four quantities with a x-y slice of the subgrid-scale energy transfer. Only a section of the full plane is presented in order to illustrate the small scale details. The colour-map represents the exactly computed small-scale energy transfer $T^{\mathcal{S}}(\mathbf{x})$. It is clear that along strong positive (forward) transfers there are areas of backward energy transfer (blue). This phenomenon, called *backscatter*, was investigated by Piomelli *et al.* (1991) for a turbulent channel flow. They showed that even though on average the flow of energy is directed from large to small scales following the energy cascade, strong local positive and negative flows occur. Magnitudes of those events are much larger than the average forward transfer. Also, they correlated the highest magnitude transfers with near-wall areas where the largest Reynolds stresses occurred. In the present work, the strongest (positive and negative) transfers occur in the middle of the channel, away from the wall. The large scale coincidence with high Reynolds stress areas is maintained, as can be observed by comparing figures 4.54 and 4.38.

Qualitative comparison of all four quantities (4.13) to (4.17) shows reasonable agreement on a large scale. The areas of large transfers in the middle of the chan-

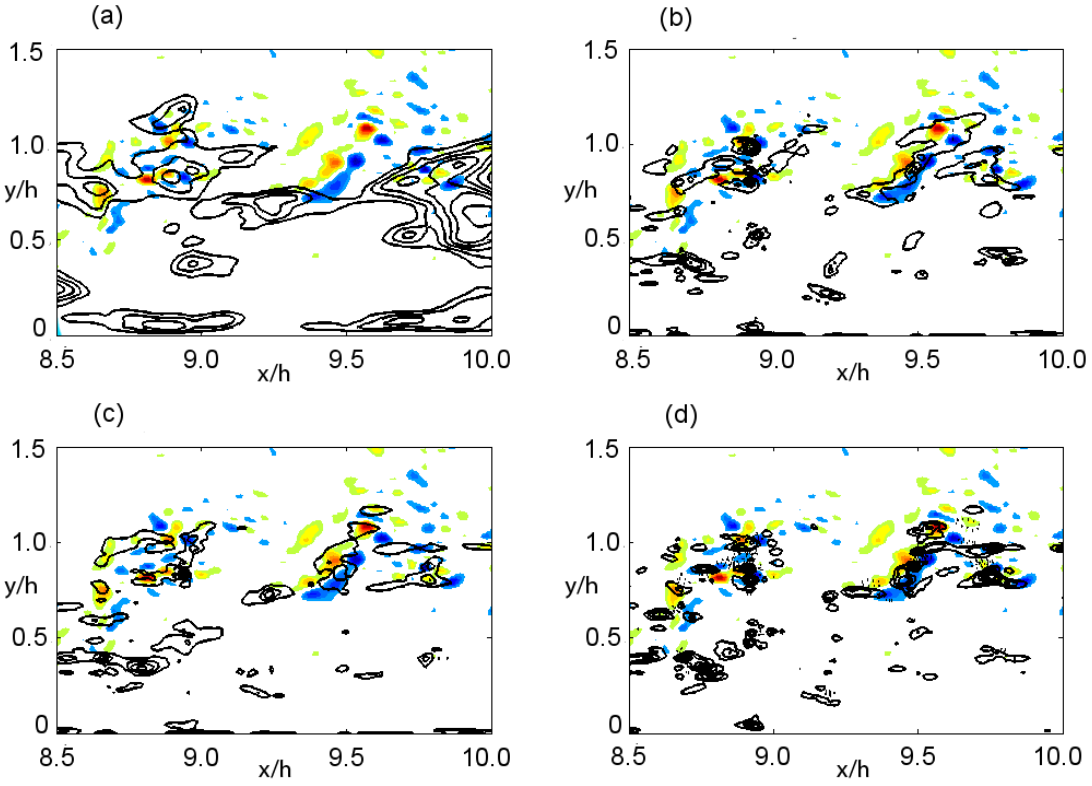

Figure 4.54: Subgrid-scale energy transfer vs large scale quantities - colour-maps represent $\mathbb{T}^S(\mathbf{x})$. Hot colour stand for positive value, cold for negative. Contours represent (a) kinetic energy, (b) enstrophy, (c) dissipation, (d) enstrophy production. Dotted line represents negative values.

nel (around $y = 1h$) are covered by the areas of large quantity value. However, all four quantities also have large values close to the wall and below the channel centre. On a small scale, none of the four matches the structure of the small-scale energy transfer. Kinetic energy, enstrophy and viscous dissipation have only positive values, therefore will never represent backscatter correctly. Negative values of the enstrophy production are sparse and do not correspond to backscatter areas either. Figures 4.54 (b-d) show that enstrophy, its production and viscous dissipation have similar intermittent structure to the energy transfer, as opposed to kinetic energy, which is much more regular. Backscatter areas in figure 4.54 (b) and (c) tend to occur near the areas of high enstrophy and dissipation, but rarely inside the contour. This is consistent with results of Kerr *et al.* (1996), where similar tendency was observed for isotropic turbulence. More recently Natrajan & Christensena (2006) documented the relationship between backscatter areas and hairpin vortices in the turbulent boundary layer. They report that strong negative energy transfers occur "upstream/above and downstream/below" each hairpin head, as well as at the trailing edge of a vortex packet. The mixing zone in backward-facing step configuration lacks the structure of wall bounded turbulence, but the present results indicate that the backscatter events occur near the areas of high vorticity.

In order to perform quantitative analysis the correlation coefficient was introduced

$$C_{pq} = \frac{\langle p(\mathbf{x})q(\mathbf{x})\rangle}{\sqrt{(p(\mathbf{x}))^2}\sqrt{(q(\mathbf{x}))^2}} \tag{4.18}$$

where $p(\mathbf{x})$ and $q(\mathbf{x})$ are scalar functions and $\langle\cdot\rangle$ stands for averaging over the entire slice. Table 4.3 presents the coefficients for correlations of $T^{\mathrm{S}}(\mathbf{x})$ with $E(\mathbf{x})$,

$O(\mathbf{x})$, $D(\mathbf{x})$ and $\omega\mathbf{S}\omega(\mathbf{x})$. All correlation factors are small, which confirms that none of the selected large-scale quantities can indicate the forward and backward energy transfer zones accurately.

Correlated quantity	C
$E(\mathbf{x})$	0.026
$O(\mathbf{x})$	0.0015
$D(\mathbf{x})$	0.056
$\omega\mathbf{S}\omega(\mathbf{x})$	0.017

Table 4.3: Correlation factors of large-scale quantities with small-scale energy transfer

4.5.3 Smagorinsky model

In order to benchmark the performance of existing LES models in the presented framework, the Smagorinsky model was used to predict the small scale energy transfer given only the large-scale flow. The Smagorinsky model's transfer is given by

$$T_{Smag}(\mathbf{x}) = u_i^{\mathcal{L}}(\mathbf{x})\tau_{ij,j}, \tag{4.19}$$

where

$$\tau_{ij} - \frac{\delta_{ij}}{3}\tau_{kk} = -2C\Delta^2(S_{ij}S_{ij})^{1/2}S_{ij}. \tag{4.20}$$

C is the Smagorinsky constant and Δ is the mesh size. Neither C nor Δ affects the correlation factor, so their value can be chosen arbitrary. Figure 4.55 presents a qualitative comparison of T_{Smag} and $T^{\mathcal{S}}(\mathbf{x})$. The maxima of the Smagorinsky model coincide with most of exactly computed energy transfers. Also, very few of T_{Smag} maxima are not located over the biggest energy transfers. Unfortunately the Smagorinsky model is based on the assumption that the energy is transferred

in the forward direction only, therefore it does not predict backscatter. This does contribute to the fact, that for T_{Smag} the correlation factor $C = 0.036$ is still very small. Improvement over raw large-scale quantities is visible, yet it is not very significant.

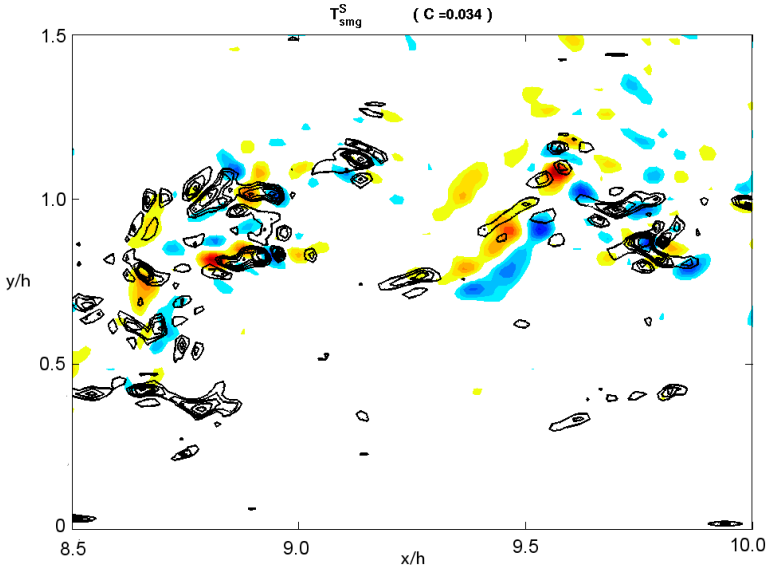

Figure 4.55: Small-scale energy transfer vs Smagorinsky transfer - colour-map represents $T^{\mathcal{S}}$.

4.5.4 Decomposition of small-scale non-linear term

Quantities (4.13) to (4.17) and the Smagorinsky model are based on first derivatives of the large-scale flow. Kerr *et al.* (1996) propose a different approach to small-scale energy transfer investigations, by utilising the rotation form of the Navier-Stokes equation

$$\frac{\partial \mathbf{u}}{\partial t} + \mathbf{u} \times \omega = -\frac{1}{\rho}\nabla P + \nu \Delta \mathbf{u}, \tag{4.21}$$

where $\omega = \nabla \times \mathbf{u}$ is the vorticity and $P = p + \frac{1}{2}\mathbf{u} \cdot \mathbf{u}$ is the total pressure. Now if the non-linear term is $N(\mathbf{x}) = \mathbf{u} \times \omega$, it can be decomposed as

$$\mathbf{u} \times \omega - \underbrace{\mathbf{u}^{\mathcal{L}} \times \omega^{\mathcal{L}}}_{I} = \underbrace{\mathbf{u}^{\mathcal{L}} \times \omega^{\mathcal{S}}}_{II} + \underbrace{\mathbf{u}^{\mathcal{S}} \times \omega^{\mathcal{L}}}_{III} + \underbrace{\mathbf{u}^{\mathcal{S}} \times \omega^{\mathcal{S}}}_{IV}, \tag{4.22}$$

which can be written as

$$N_i^{tot} - N_i^{\mathcal{L}} = N_i^{II} + N_i^{III} + N_i^{IV}. \tag{4.23}$$

The terms on the left-hand-side give the small-scale non-linear term $N_i^{\mathcal{S}}$, therefore the terms on the right-hand-side effectively decompose the small-scale energy transfer $T^{\mathcal{S}}$ into three components T^{II}, T^{III},T^{IV}.

Figure 4.56 presents qualitative comparison of $T^{\mathcal{S}}$ with T^{II}, T^{III} and T^{IV}. Table 4.4 gathers corresponding correlation coefficients.

Correlated quantity	C
T^{II}	0.89
T^{III}	0.59
T^{IV}	0.57
$T^{II} + T^{III} + T^{IV}$	1.0

Table 4.4: Correlation factors for decomposed energy transfer terms

As found by Kerr *et al.* (1996), $T^{\mathcal{S}}$ has strong correlation with T^{II}, which represents the small-scale vorticity advected by the resolved velocity field. This result supports the suggestion of Kerr *et al.* (1996), that a model for energy transfer, which also represents backscatter, could be sought by modelling the subgrid-scale vorticity.

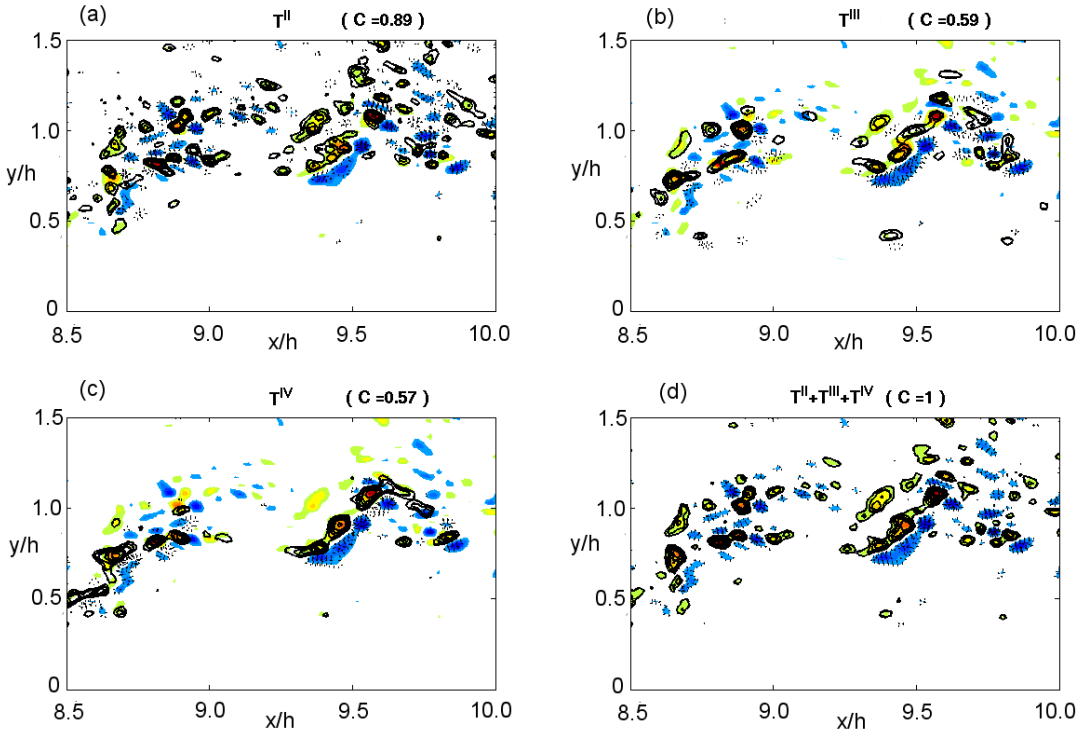

Figure 4.56: Small-scale energy transfer term decomposition - correlation factors in brackets.

Chapter 5

Conclusions and Future Work

The objective of the project was to utilise the existing high-order spectral element method code Semtex to generate high-resolution, high Reynolds number statistics and establish a database for turbulence modelling. Direct numerical simulation of turbulent flow over a backward-facing step was performed for the highest-to-date Reynolds number $Re_h = 9000$. To the author's knowledge, it is also a first DNS of a fully turbulent 3D backward-facing step flow in a channel. Apart from the statistics of pressure, velocity and Reynolds stress tensor components, the 3D history of pressure and velocity have been archived. In addition, analysis of the structure and dynamic properties of the flow was performed and revealed interesting results for the secondary recirculation eddy and reattachment position oscillations.

This chapter summarises the work done and gives the outline of future work regarding this topic.

5.1 Numerical Method

5.1.1 hp-refinement of the mesh

The spectral element method turned out to be very well suited to this kind of problem. The flexibility in generation of the element mesh allowed the computational grid to be concentrated in the areas of interest. The Gauss-Lobatto-Legendre distribution of nodal points within elements provided a natural refinement near the walls, at the step edge and within the mixing layer. The minimum distance between the nodes in the streamwise direction (located at the step edge) was $\Delta x^+ = 1.78$. Vertical resolution mimicked a Chebyshev distribution across the inlet channel. The first node away from the wall was located at $\Delta y^+ = 0.528$. In the outflow channel the vertical distribution of elements from the top part was reproduced in the bottom part of the channel, forming a natural refinement in the mixing layer. The mesh in the centre of the channel was coarsened further downstream. In the spanwise direction, 128 evenly spaced points provided enough resolution for the spanwise kinetic energy spectrum to exhibit sufficient modal decay of E_{uu} and E_{ww}. Like in Le *et al.* (1997) the E_{vv} modal decay near the wall was not sufficient, which could indicate the need for more spanwise resolution in order to better resolve the smallest scales near the wall.

The use of an unstructured grid would lead, possibly, to a more optimal element mesh. Having the average flow field and statistics it is possible to generate *a posteriori* an optimal unstructured mesh that would be refined in the areas of large gradients and coarsened accordingly downstream of the reattachment. Such an unstructured grid could be used in future simulations of this case, given the

fact that X_r does not change much with respect to Re in the turbulent regime.

Apart from the flexibility of h-refinement of the element mesh, the possibility of global p-refinement proved very effective in generation of an initial condition and convergence study. The high order approximation of the solution within elements allowed for the easy projection between different order polynomial bases. The flow could be easily initialised using a low-order expansion basis, which allowed for cheap preliminary simulations with short running time. By gradually increasing the polynomial order, the initial condition could be easily and effectively generated.

5.1.2 Boundary conditions and flowrate control

The crucial part in setting up a simulation of a turbulent BFS flow was to enable a turbulent inflow to the domain. This was achieved by a modification of the Lund *et al.* (1998) technique, who proposed extracting the necessary data from an auxiliary simulation of a turbulent channel flow. In the present case the limitations of Semtex did not allow for such a manoeuvre, therefore a periodic channel was incorporated into the main simulation by a copy boundary condition. Using this technique we have taken the velocity and pressure fields from a plane downstream of the inlet and used them as Dirichlet conditions for the inlet plane.

An important limitation of this approach was the necessity of maintaining a constant mass flow rate. In the Lund *et al.* (1998) technique, constant flowrate could be easily maintained in the auxiliary simulation. Attempts to set a variable pressure gradient to force the flow did not yield good results, as the time it took the simulation to converge to a quasi-steady flowrate was very long. This

approach was inefficient for the BFS flow, as finding the forcing that results in the desired flowrate would be very costly and time-consuming. Another method, utilising Green functions in a form of Stokes equation solutions as a correction to the velocity field in the periodic inlet section was applied. It allowed for very accurate flowrate control at little extra computational cost.

The copy inlet boundary condition managed to reproduce a streamwise velocity profile that collapses well with computational results for channel flow by Kim *et al.* (1987) and Moser *et al.* (1999). The turbulence intensity profiles also fit the results of Moser *et al.* (1999).

The outflow condition was prescribed as a no-stress Neumann condition. By placing it sufficiently far downstream, we avoided possible problems with convecting vortical structures through the outlet plane. The distortion to the flow-field was fully confined within the distance of $2h$ from the exit plane.

5.2 Simulation Results

5.2.1 Reattachment length and coefficient of friction

The mean reattachment length was $X_r = 8.62h$ for $ER = 2.0$ and $Re_h = 9000$. This result, along with $X_r = 8.16h$ for $Re_h = 6000$ preliminary simulation, fits the prediction made by Armaly *et al.* (1983) for turbulent flow over BFS with $ER = 2.0$. The streamwise profile of the coefficient of friction at the bottom wall, with abscissas scaled by X_r, agreed with previous experimental and computational results, taking into account the difference in Re_h and ER. The position of a maximum negative skin friction was predicted at $0.62X_r$ which is in good

agreement with previous experimental findings. The dependence of the value of maximum negative peak on Re_h was confirmed.

5.2.2 Coefficient of pressure

The coefficient of pressure at the bottom wall, collapsed using the scaling of Kim *et al.* (1980), agreed very well with previous numerical and experimental results. The position of maximum C_P with respect to X_r confirms the strong dependence on ER and complements previous experimental and numerical results obtained for lower expansion ratios.

5.2.3 Velocity field

The time and spanwise averaged velocity field exhibits, apart from the main recirculation bubble, the secondary and tertiary corner eddies. The secondary eddy appears to have an additional vortical structure located at its downstream tip and rotating in the same direction. Hall *et al.* (2003) indicated that such a new structure in the neighbourhood of the secondary eddy might exist, but the PIV technique used for its investigation did not provide any conclusive evidence. This study confirms those suggestions and investigates this structure further. The time average of the velocity field revealed a spanwise structure of the secondary recirculation eddy and suggests that the additional secondary eddy present in the spanwise-averaged flow is a result of averaging of the four lobes of the secondary eddy. A similar spanwise structure was present in the primary recirculation bubble, which suggests there is a strong correlation between those two eddies. This confirms the suggestion of Spazzini *et al.* (2001) that the behaviour

of the primary and secondary recirculation bubbles might be two aspects of the same phenomenon. The wavy shape of the recirculation bubbles is explained by the presence of permanent streamwise vortices in the mixing layer.

The question then arises of whether this is a real physical phenomenon, or if it is a numerical effect caused by an inadequate spanwise domain length. Simulations on reduced spanwise domain length showed a reduced number of spanwise vortices, which supports the adequacy of the domain size in the main simulation.

A fully developed velocity profile is not recovered within the computational domain. This is in agreement with previous experimental studies reporting very long regeneration distances downstream of the step.

5.2.4 Wall shear stress and oscillations of the reattachment position

The wall shear stress time history was closely examined and revealed persistent large-scale spanwise structure, oscillations in the reattachment as shown in figure 4.39, and additional small-scale intermittent behaviour. A cycle of reattachment oscillations was identified and documented using a series of snapshots. A time average of wall shear stress revealed a persistent wavy shape of the reattachment line, with four main lobes in the spanwise direction. Subsequent analysis of spanwise averaged wall shear stress time history showed a saw-tooth shape of the primary reattachment position, similar to results reported in Le *et al.* (1997) and Schafer *et al.* (2009). The dynamic behaviour of the secondary reattachment position (the downstream tip of the secondary corner eddy) also revealed a weak periodic behaviour. The analysis of the spectrum of pressure and velocity

fluctuations at a position near the primary reattachment showed a matching primary frequency with $St = 0.078$, which agrees very well with previous findings. Investigation of the spectra in different points in the flow, as well as additional simulation with different inlet length, showed that the regeneration frequency $St = 0.127$ does not influence the reattachment flapping. The visualisation of the interaction of pressure minima, which correspond to the vortex cores, with the primary recirculation bubble explains the origins of reattachment position oscillations. Similar analysis was performed by Schafer *et al.* (2009) for transitional flow with laminar inflow, but the characteristic frequency was significantly different from the present result. This work extends the validity of Schafer *et al.* (2009) argument and provides a visualisation of the reattachment flapping phenomenon in a fully turbulent BFS flow.

5.2.5 Small-scale energy transfer

The analysis of the small-scale energy transfer along the lines of Kerr *et al.* (1996) was performed in order to present its usefulness in non-isotropic turbulence flow and provide additional data for turbulence modelling. The work by Piomelli *et al.* (1991) reported large positive and negative energy transfers in the regions of high Reynolds stresses near the wall in a turbulent channel flow. The current investigation also revealed high transfers in the high Reynolds stress zone, which occurred in the mixing layer near the reattachment position. The recent work by Natrajan & Christensena (2006) links the backscatter events with the heads of hairpin vortices in the boundary layer. The current work indicated the presence of negative energy transfer near the regions of high enstrophy.

The decomposition of the nonlinear term confirmed the result of Kerr *et al.* (1996) that the large-scale velocity - small-scale vorticity interactions are strongly correlated with the small-scale energy transfer and can be used in turbulence modelling for predicting regions of backscatter.

Surprisingly, the near wall reattachment region did not show significantly increased energy transfers. It appears that no additional terms would be needed in modelling the reattachment, contrary to the suggestion by Chandrsuda & Bradshaw (1981). Nonetheless, an accurate modelling of the backscatter events is needed.

5.3 Future Work

Future work involves continuing the DNS simulation with extended spanwise dimension to collect fully converged statistics. Such simulation was started, but the computational resources were insufficient to run it long enough to obtain any conclusive results.

Another interesting possibility would be a DNS simulation of a channel with a double expansion. Such a case would enable the study of bifurcation of the shear layer that develops from this configuration.

Overcoming the memory limitation of Semtex, which did not allow interpolation polynomials of order higher than 10, would allow us to utilise this still experimental software for simulations with much higher Reynolds number. The problem was identified as lying in the input/output operations and steps will be undertaken to fix this.

Bibliography

Abbot, D.E. & Kline, S.J. (1962). Experimental investigations of subsonic turbulent flow over single and double backward-facing steps. *Transactions of the ASME. Series D, Journal of Basic Engineering*, **84**.

Adams, E.W. & Johnston, J.P. (1988). Effects of the separating shear layer on the reattachment flow structure. part 1: Pressure and turbulence quantities. part 2: Reattachment length and wall shear stress. *Experiments in Fluids*, **6**, 400–408,493–499.

Armaly, B.F., Durst, F., Pereira, J.C.F. & Schonung, B. (1983). Experimental and theoretical investigation of backward-facing step flow. *Journal of Fluid Mechanics Digital Archive*, **127**, 473–496.

Biswas, G., Breuer, M. & Durst, F. (2004). Backward-facing step flows for various expansion ration at low and moderate reynolds nubers. *Transactions of the ASME*, **126**, 362 – 374.

Blackburn, H. & Schmidt, S. (2003). Spectral element filtering techniques for large eddy simulation with dynamic estimation. *Journal of Computational Physics*, **186**, 610–629.

Blackburn, H. & Sherwin, S. (2004). Formulation of a galerkin spectral element fourier method for three-dimensional incompressible flows in cylindrical geometries. *Journal of Computational Physics*, **197**, 759–778.

Blackburn, H. & Sherwin, S. (2007). Instability modes and transition of pulsatile stenotic flow: pulse-period dependence. *Journal of Fluid Mechanics*, **573**, 57–88.

Blackburn, H., Ooi, A. & Chong, M. (2007). The effect of corrugation height on flow in a wavy-walled pipe. *16th Australian Fluid Mechanics Conference*.

Bradshaw, P. & Wong, F.Y.F. (1972). The reattachment and relaxation of a turbulent shear layer. *Journal of Fluid Mechanics Digital Archive*, **52**, 113–135.

Cantwell, C., Barkley, D. & Blackburn, H. (2010). Transient growth analysis of flow through a sudden expansion in a circular pipe. *Physics of Fluids*, **22**, 034101–115.

Cantwell, C.D. (2009). *Transient Growth of Separated Flows*. Ph.D. thesis, University of Warwick.

Castro, I. & Haque, A. (1987). The structure of a turbulent shear layer bounding a separation region. *Journal of Fluid Dynamics*, **179**, 439–468.

Chandrsuda, C. & Bradshaw, P. (1981). Turbulence structure of a reattaching mixing layer. *Journal of Fluid Mechanics*, **110**, 171–194.

Cherdron, W., Durst, F. & Whitelaw, J.H. (1978). Asymmetric flows and instabilities in symmetric ducts with sudden expansion. *Journal of Fluid Mechanics*, **84**, 13–31.

Chin, C., Ooi, A., Marusic, I. & Blackburn, H. (2010). The influence of pipe length on turbulent statistics computed from direct numerical simulation data. *Physics of Fluids*, **22**, 115107.

Chu, D. & Karniadakis, G. (1993). A direct numerical simulation of laminar and turbulent flow over riblet-mounted surfaces. *Journal of Fluid Mechanics*, **250**, 1–42.

Davidson, P. (2007). *Turbulence. An Introduction for Scientists and Engineers*. Oxford University Press.

den Toonder, J. & Nieuwstadt, F. (1997). Reynolds number effects in a turbulent pipe flow for low to moderate re. *Physics of Fluids*, **9**, 3398–3409.

Domaradzki, J.A., Liu, W. & Brachet, M. (1993). An analysis of subgrid-scale interactions in numerically simulated isotropic turbulence. *Physics of Fluids A*, **5**, 1747–1759.

Driver, D.M. & Seegmiller, H.L. (1985). Features of a reattaching shear layer in divergent channel flow. *AIAA Journal*, **23**, 163–171.

Durst, F. & Tropea, C. (1981). Turbulent, backward-facing step flows in two-dimensional ducts and channels. In *Proceedings of the Fifth International Symposioum on Turbulent Shear Flows*, 18.1–18.5, Cornell University.

Durst, F., Melling, A. & Whitelaw, J.H. (1974). Low reynolds number flow over a plane symmetric sudden expansion. *Journal of Fluid Mechanics*, **64**, 111–128.

Etheridge, D.W. & Kemp, P.H. (1978). Measurements of turbulent flow downstream of a rearwad-facing step. *Journal of Fluid Mechanics*, **86**, 545–566.

Friedrich, R. & Arnal, M. (1990). Analysing turbulent backward-facing step flow with the lowpass-filtered navier-stokes equations. *Journal of Wind Engineering and Industrial Aerodynamics*, **35**, 101–228.

Gear, C. (1973). *Numerical Initial Value Problems in Ordinary Differential Equations*. Prentice-Hall, Englewood Cliffs, NJ.

Hall, S., Behnia, M., Fletcher, C. & Morrison, G. (2003). Investigation of the secondary corner vortex in a benchmark turbulent backward-facing step using cross-correlation particle imaging velocimetry. *Experiments in Fluids*, **35**, 139–151.

Henderson, R. & Karniadakis, G. (1995). Unstructured spectral element methods for simulation of turbulent flows. *Journal of Computational Physics*, **122**, 191–217.

Hussain, A. & Reynolds, W. (1975). Measurements in fully developed turbulent channel flow. *ASME J. Fluid. Engng.*, **97**, 568–578.

Jeong, J. & Hussain, F. (1995). On the identification of a vortex. *Journal of Fluid Mechanics*, **285**, 69–94.

Jovic, S. & Driver, D. (1994). Backward-facing step measurements at low reynolds number. *NASA Tech. Mem.*, 108807.

Jovic, S. & Driver, D. (1995). Reynolds number effect on the skin friction in separated flows behind a backward-facing step. *Experiments in Fluids*, **18**, 464–467.

Kaikstis, L., Karniadakis, G.E. & Orszag, S.A. (1991). Onset of three-dimensionality, equilibria, and early transition in flow over a backward-facing step. *Journal of Fluid Mechanics*, **231**, 501–538.

Karniadakis, G. & Sherwin, S. (2005). *Spectral/HP Element Methods for Computational Fluid Dynamics*. Oxford University Press.

Karniadakis, G., Israeli, M. & Orszag, S. (1991). High-order splitting methods for the incompressible navier-stokes equations. *Journal of Computational Physics*, **97**, 414–443.

Kasagi, N. & Matsunaga, A. (1995). Three-dimensional particle-tracking velocimetry measurement of turbulence statistics and energy budget in a backward-facing step flow. *International Journal of Heat and Fluid Flow*, **16**, 477–485.

Kerr, R.M., Domaradzki, J.A. & Barbier, G. (1996). Small-scale properties of nonlinear interactions and subgrid-scale energy transfer in isotropic turbulence. *Physics of Fluids*, **18**, 197–207.

Kim, J., Kline, S.J. & Johnston, J.P. (1980). Investigation of a reattaching turbulent shear layer: Flow over a backward-facing step. *Transactions of the ASME. Journal of Fluid Engineering*, **102**, 302–308.

Kim, J., Moin, P. & Moser, R. (1987). Turbulent statistics in fully developed channel flow at low reynolds number. *Journal of Fluid Mechanics*, **177**, 133–166.

Le, H. (1995). *Direct numerical simulation of turbulent flow over a backward-facing step*. Ph.D. thesis, Stanford University.

Le, H., Moin, P. & Kim, J. (1993). Direct simulations of turbulent flow over a backward-facing step. In *Proceedings of the Nineth Symposium on Turbulent Shear Flows*, 13–2–1 – 13–2–5, Kyoto University.

Le, H., Moin, P. & Kim, J. (1997). Direct numerical simulation of turbulent flow over a backward-facing step. *Journal of Fluid Mechanics*, **330**, 349–374.

Levin, J., Iskandarani & M. Haidvogel, D. (1997). A spectral filtering procedure for eddy-resolving simulations with a spectral element ocean model. *Journal of Computational Physics*, **137**, 130–154.

Lund, T., Wu, X. & Squires, K. (1998). Generation of turbulent inflow data for spatially-developing boundary layer simulations. *Journal of Computational Physics*, **140**, 233–258.

Marcus, P. (1984). Simulation of taylor-couette flow. part 1. numerical methods and comparison with experiment. *Journal of Fluid Mechanics*, **146**.

Martin, W.W. (1974). *Anwendung der hydrodynamischen Stabilitätstheorie auf die Schwingung von Schützen*. Ph.D. thesis, Universität Karlsruhe.

Metais, O. (2001). *New Trends in Turbulence*, chap. Large-eddy simulation of turbulence. Springer.

Moffat, H. (1964). Viscous and resistive eddies near a sharp corner. *Journal of Fluid Dynamics*, **18**, 1–18.

Moser, R., Kim, J. & Mansour, N. (1999). Direct numerical simulation of turbulent channel flow up to $\mathrm{re}_\tau = 590$. *Physics of Fluids*, **11**, 943–945.

Natrajan, V. & Christensena, K. (2006). The role of coherent structures in subgrid-scale energy transfer within the log layer of wall turbulence. *Physics of Fluids*, 065104.

Orszag, S., Israeli, M. & Deville, O. (1986). Boundary conditions for incompressible flows. *Journal of Scientific Computing*, **75**.

Piomelli, U., Cabot, W., Moin, P. & Lee, S. (1991). Subgrid-scale backscatter in turbulent and transitional flows. *Physics of Fluids A*, **3**, 1766–1771.

Roshko, A. & Lau, J. (1965). Some observations on transition and reattachment of a free shear layer in incompressible flow. In *Proceedings of the 1965 Heat Transfer and Fluid Mechanics Institute*, 157–167, Stanford University Press.

Schafer, F., Breuer, M. & Durst, F. (2009). The dynamics of the transitional flow over a backward-facing step. *Journal of Fluid Dynamics*, **623**, 85–119.

Sherwin, S. & Blackburn, H. (2005). Three-dimensional instabilities and transition of steady and pulsatile axisymmetric stenotic flows. *Journal of Fluid Mechanics*, **533**, 297–327.

Silveira Neto, A., Grand, D., Metais, O. & Lesieur, M. (1993). A numerical investigation of the coherent vortices in turbulence behind a backward-facing step. *Journal of Fluid Mechanics*, **256**, 1–25.

Spazzini, P., Iuso, G., Oronato, M., Zurlo, N. & Di Cicca, G. (2001). Unsteady behaviour of back-facing step flow. *Experiments in Fluids*, **30**, 551–561.

Walsh, M. (1980). Drag characteristics of v-groove and transverse curvature riblets. *Prog. Astronaut. Aeronaut.*, **72**, 168.

Wei, T. & Willmarth, W. (1989). Reynolds-number effects on the structure of a turbulent channel flow. *Journal of Fluid Mechanics*, **204**, 57–95.

Westphal, R.V., Johnston, J.P. & Eaton, J.K. (1984). Experimental study of flow reattachment in a single-sided sudden expansion. *NASA STI/Recon Technical Report N*, **84**, 18571–+.

Yoshioka, S., Obi, S. & Masuda, S. (2001). Turbulence statistics of periodically perturbed separated flow over backward-facing step. *Journal Heat and Fluid Flow*, **22**, 393–401.